

SOOT FORMATION DURING COAL PYROLYSIS

A Dissertation

Presented to the

Department of Chemical Engineering

Brigham Young University

In Partial Fulfillment

of the Requirements for the Degree

Doctor of Philosophy

by

Jinliang Ma

February, 1996

This dissertation by Jinliang Ma is accepted in its present form by the Department of Chemical Engineering of Brigham Young University as satisfying the dissertation requirement for the degree of Doctor of Philosophy.

Thomas H. Fletcher, Advisor

Brent W. Webb, Advisory Committee

John N. Harb, Advisory Committee

William G. Pitt, Graduate Coordinator

Date

TABLE OF CONTENTS

LIST OF TABLES	vi
LIST OF FIGURES	vii
ACKNOWLEDGMENTS	x
NOMENCLATURE	xi
Chapter 1. INTRODUCTION.....	1
General Description of Soot	1
Origin of Soot in Coal-Fired Furnaces	1
Importance of Soot in Coal Combustion	2
Questions to Be Addressed	3
Objectives of This Research	4
Chapter 2. LITERATURE REVIEW.....	6
General Mechanisms of Soot Formation and Oxidation for Simple Hydrocarbons.....	6
Structure and Properties of Soot	6
Soot Formation Stages	8
Soot Oxidation	16
Soot from Secondary Reactions of Coal Volatiles	18
Experiments in Inert Conditions	18
Experiments in Combustion Gases	22
Nitrogen Evolution Due to Secondary Reactions	23
Soot Sampling Techniques	25
Chapter 3. EXPERIMENTAL APPARATUS AND PROCEDURES	28
Overview.....	28
Flat-Flame Flow Reactor	29
Coal Particle Feeder.....	35
Thermophoretic Sampling	37
Bulk Collection and Soot/Char Separation.....	40
Suction Probe	42
Virtual Impactor.....	43
Cyclone	45
Soot Filters.....	47

Water Condenser, Water Trap, Flow Meters and Vacuum Pumps.....	49
System Calibration and Testing.....	49
Particle Residence Time Measurement.....	52
Mass Release and ICP Analysis.....	53
Elemental Analysis.....	54
Chapter 4. EXPERIMENTAL RESULTS.....	55
Coal Types and Characterization.....	55
Particle Residence Time Measurements.....	55
Thermophoretic Sampling.....	61
Soot from a Butane Flame.....	61
Coal-Derived Soot.....	62
Evaporating Deposits.....	65
Bulk Collection of Soot and Char Particles.....	67
General Description of Soot Collected By the Suction Probe.....	67
Soot Yield and Volatiles Yield.....	71
Elemental Composition of Products.....	82
Chapter 5. PROCESS SIMULATIONS.....	88
Flat Flame Structure.....	88
Coal Devolatilization.....	93
Soot Formation and Agglomeration.....	97
Chapter 6. DISCUSSION OF RESULTS.....	103
Thermophoretic Soot Sampling.....	103
Bulk Soot Sampling Experiments.....	107
Volatiles Yield.....	107
Total Soot Yield.....	108
Soot Agglomeration or Aggregation.....	114
Elemental Composition of Products.....	116
Kinetics of Soot Formation and Agglomeration.....	117
Chapter 7. CONCLUSIONS AND RECOMMENDATIONS.....	118
REFERENCES.....	123
Appendix.....	130
A. Effect of Soot Radiation on Flame Temperature.....	130
B. Code for Generation of Stepping Signal.....	134
C. Design of the Virtual Impactor.....	136
D. Design of the Cyclone.....	139
E. Code for Obtaining Kinetic Constants From Fitting Experimental Data.....	142

F. Kinetic Scheme for Methane/Hydrogen Combustion.....	146
G. Temperature Correction.....	148
H. Tabulation of Experimental Data.....	149

LIST OF TABLES

Table 2.1.	A summary of coal pyrolysis experiments conducted by three investigators.	21
Table 3.1.	Flow rates in three temperature settings.	33
Table 3.2.	Gas flow rates used for particle bulk collection experiments.	51
Table 4.1.	Proximate and ultimate analyses for the six coals used in this study.	56
Table 4.2.	Coefficients for curve-fits of particle residence time during the initial acceleration stage.	58
Table 4.3.	Coefficients for curve-fits of particle residence time determined from high-speed video camera tests.	59
Table 5.1.	Chemical structure parameters for six coals tested.	94
Table 5.2.	Optimized activation energies and pre-exponential factors.	102
Table D-1.	Major dimensions of the cyclone design.	141

LIST OF FIGURES

Figure 2.1.	Soot yields versus temperature.	9
Figure 2.2.	Postulated mechanisms for the formation of the first aromatic ring.....	11
Figure 2.3.	Principal reaction pathway for formation of two-ring aromatics.	12
Figure 2.4.	Principal reaction pathways for formation of fused polycyclic aromatics.....	13
Figure 2.5.	Possible reaction pathways for soot generation in coal pyrolysis.	25
Figure 2.6.	TEM micrograph showing soot from an ethene flame.	27
Figure 3.1.	Schematic of the flat flame burner and gas delivery system.	30
Figure 3.2.	A photograph of the visible soot cloud.....	32
Figure 3.3.	Centerline gas temperature profiles in the quartz tower.....	33
Figure 3.4.	Centerline gas temperature profile in the Pyrex tower.	34
Figure 3.5.	Horizontal gas temperature profiles at different heights of the quartz tower.	34
Figure 3.6.	Radial temperature profiles at different heights of the Pyrex tower.....	35
Figure 3.7.	Schematic of the coal particle feeder.....	36
Figure 3.8.	Schematic of the flat-flame flow reactor and thermophoretic sampling system.....	38
Figure 3.9.	Schematic of the Pyrex tower for thermophoretic sampling.	39
Figure 3.10.	Particle collection and separation system.	41
Figure 3.11.	Schematic of the suction probe.....	43
Figure 3.12.	Schematic of the virtual impactor.....	44
Figure 3.13.	Schematic of the cyclone and the char collection cap.	46
Figure 3.14.	Schematic of the filter holder.....	48
Figure 4.1.	Frames of video images showing particle movement.....	60
Figure 4.2.	A plot of height versus time for a Pittsburgh #8 coal particle.	60
Figure 4.3.	Micrograph of soot particles form a butane diffusion flame.	61
Figure 4.4.	TEM micrograph of soot from the Utah coal, collected at 13 cm above the burner (65 ms).	63
Figure 4.5.	TEM micrograph of soot from the Utah coal, collected at 25.5 cm above the burner (128 ms).	63

Figure 4.6. TEM micrograph of soot from the Utah coal, collected at 15.5 cm above the burner (78 ms).	64
Figure 4.7. TEM micrograph of separated soot particles from the Pittsburgh #8 coal collected at 5.5 cm (28 ms).	64
Figure 4.8. TEM micrograph of tar deposit from the Utah coal, collected at 20.5 cm (103 ms).	66
Figure 4.9. TEM micrograph of solid particles inside tar droplet from Utah coal, collected at 20.5 cm above the burner (103 ms).	66
Figure 4.10. Soot agglomerate layer formed upon shaking the char/soot sample.	69
Figure 4.11. SEM micrograph of soot/char mixture.	69
Figure 4.12. SEM micrograph showing the surface of a bright particle.	70
Figure 4.13. SEM micrograph showing the surface of a gray char particle.	70
Figure 4.14. SEM micrograph of small soot particles collected on a soot filter.	71
Figure 4.15. Measured volatiles yields and soot yields for Pittsburgh #8 coal.	73
Figure 4.16. Measured volatiles yields and soot yields for Illinois #6 coal.	74
Figure 4.17. Measured volatiles yields and soot yields for Utah Hiawatha coal.	75
Figure 4.18. Measured volatiles yields and soot yields for Pocahontas #3 coal.	76
Figure 4.19. Measured volatiles yields and soot yields for Dietz coal.	77
Figure 4.20. Measured volatiles yields and soot yields for Zap lignite.	78
Figure 4.21. A comparison between mass balance method and ICP method (mass release of Pittsburgh #8 coal at 1800 K).	79
Figure 4.22. Effect of pyrolysis temperature on total soot yield.	81
Figure 4.23. Effect of pyrolysis temperature on soot yield (< 5 μm).	81
Figure 4.24. Elemental composition of the soot from Pittsburgh #8 coal.	83
Figure 4.25. Elemental composition of the soot from Illinois #6 coal.	83
Figure 4.26. Elemental composition of the soot from Utah Hiawatha coal.	84
Figure 4.27. Elemental composition of the soot from Pocahontas #3 coal.	84
Figure 4.28. Elemental composition of the soot from Dietz coal.	85
Figure 4.29. Elemental composition of the char from Pittsburgh #8 coal.	85
Figure 4.30. Elemental composition of the char from Illinois #6 coal.	86
Figure 4.31. Elemental composition of the char from Dietz coal.	86
Figure 5.1. Species mole fractions versus height at T=1900 K.	90
Figure 5.2. Species mole fractions versus height at T=1800 K.	91
Figure 5.3. Species mole fractions versus height at T=1650 K.	92
Figure 5.4. Calculated tar yields versus height in the 1900 K condition.	95
Figure 5.5. Calculated tar yields versus temperature.	95

Figure 5.6.	Calculated total volatile yields versus height at 1900 K.....	96
Figure 5.7.	Calculated total volatiles yields versus temperature.....	96
Figure 5.8.	Reaction scheme used in the simulations of soot formation and agglomeration.	97
Figure 5.9.	Calculated soot yield profiles for Pittsburgh #8 coal using the optimized kinetic coefficients in Table 5.2.....	100
Figure 5.10.	Calculated soot yield profiles for Illinois #6 coal using the optimized kinetic coefficients in Table 5.2.....	100
Figure 5.11.	Calculated soot yield profiles for Utah Hiawatha coal using the optimized kinetic coefficients in Table 5.2.....	101
Figure 5.12.	Calculated soot yield profiles for Pocahontas #3 coal using the optimized kinetic coefficients in Table 5.2.....	101
Figure 6.1.	Formation of soot streamer around a coal particle in oxygen-rich environment.	106
Figure 6.2.	Measured and calculated volatiles yields versus temperature for the Pittsburgh #8 coal.	109
Figure 6.3.	Measured and calculated volatiles yields versus coal rank in the 1900 K condition.	109
Figure 6.4.	Comparison of soot yield with tar yield for several coals.	111
Figure 6.5.	Comparison of soot yield versus temperature.....	112
Figure A-1.	The dimension of the volatile flame used for calculation.....	133
Figure C-1.	Important dimensions in the design of virtual impactor.....	138
Figure D-1.	Geometry of cyclone and design guidelines.....	140

ACKNOWLEDGMENTS

First, I wish to express my appreciation to my graduate advisor, Dr. Thomas H. Fletcher for his guidance and encouragement throughout this work. The quality of this work is a reflection of expert advice that has been received. Appreciation is also extended to Dr. Brent W. Webb for his technical advice and direction.

There have been many people whose cooperation and assistance have been vital during this research. I am grateful to Jason Haslam and Taufik Sastrawinata who helped me in construction of the test table and burner support. I would also like to thank Joshua Rossman and Melissa Dean for their assistance in the thermophoretic soot sampling experiments. Gratitude is expressed to Dominic Genetti and William Allen who conducted ICP and CHN analyses for all soot and char samples. Acknowledgment also goes to Allen Salmi of Sandia National Laboratories who helped me in design of the suction probe. The comradery of work associate James Rigby has been a positive influence in this work.

Financial support provided through the Advanced Combustion Engineering Research Center at Brigham Young University is gratefully acknowledged. I would also like to thank Sir Run Run Shaw, a Hong Kong businessman who donated the funds for my 4-year scholarship. Without his generosity, I would not have been able to come to U.S. to pursue a Ph.D. degree.

Finally, I wish to thank my wife Shirong and my son Chao for their support and patience during several years of my study. Special thanks are expressed to my beloved parents who supported my early education in the face of poverty and made me the first in my family to get a high school diploma.

NOMENCLATURE

Symbol	Definition
A_a	pre-exponential factor for soot agglomeration
A_f	pre-exponential factor for soot formation
A_g	pre-exponential factor for tar gasification
D	tube diameter
D_b	diameter of thermocouple bead
D_p	particle diameter
E_a	activation energy for soot agglomeration
E_f	activation energy for soot formation
E_g	activation energy for tar gasification
F_g	gravitational force on a particle
F_k	drag force on a particle
M_{clust}	average molecular weight of a cluster
M_w	molecular weight
N	particle number density
Q	volumetric flow rate
R	gas constant
Re	Reynolds number
Stk	Stokes number
T	temperature
V	velocity
Y_{vol}	total volatiles yield or mass release
a	acceleration
a_1, a_2, a_3	polynomial coefficients
b_1, b_2, b_3	polynomial coefficients
d	diameter
f_{sa}	mass fraction of coal (daf) as agglomerated soot
f_{sp}	mass fraction of parent coal (daf) as primary soot
f_{tar}	mass fraction of parent coal (daf) as tar
f_{tar}^o	tar mass fraction calculated by the CPD model

f_{Ti}^{ash}	mass fraction of Ti in ash
f_{Ti}^{char}	mass fraction of Ti in char
f_{Ti}^{coal}	mass fraction of Ti in coal
f_v	soot volume fraction
k	rate constant
m_{ash}	mass of ash
m_{char}	mass of char
m_{coal}	mass of coal
m_δ	average molecular weight of a side chain
p_o	fraction of intact bridge
r_a	soot agglomeration rate
r_f	soot formation rate
r_g	tar gasification rate
t	time
t_l	residence time at which a char particle luminesces
v_g	gas velocity
v_p	particle velocity
v_∞	slip velocity
z	height above the particle injection point
z_l	height at which a char particle luminesces
ε	emissivity
ϕ	equivalence ratio
μ_g	gas viscosity
ν_g	gas kinematic viscosity
ρ_g	gas density
ρ_p	particle density
σ	Stefan-Boltzmann constant
$\sigma+1$	coordination number

Chapter 1

INTRODUCTION

General Description of Soot

Generation of small submicron carbonaceous particles known as soot in the combustion and pyrolysis of hydrocarbons has been observed since the very beginning of the utilization of fossil fuels to supply energy. Soot is formed in many practical combustion systems ranging from a burning candle to sophisticated combustors such as gas turbines and internal combustion engines. Based on the experiments conducted on simple hydrocarbon flames, such as diffusion and premixed flames, it is found that soot is usually formed when conditions are sufficiently fuel rich to allow condensation or polymerization reactions of the fuel (and its initial decomposition products) to compete with oxidation (Haynes and Prado, 1980). Soot in those hydrocarbon flames usually exists in the form of both individual particles and agglomerates comprised of several primary particles.

Origin of Soot in Coal-Fired Furnaces

Soot formation has also been observed in many coal utilization processes, including coal gasification and combustion. In a conventional wall-fired, swirl-stabilized, pulverized coal combustor, coal particles with an average size around 50 microns are transported by primary air, and are injected into the furnace through the nozzles of a pulverized coal burner. When low NO_x burners are used along with staged combustion configuration, the region near the burner is fuel rich; the particles are rapidly heated at 10^4 - 10^6 K/s by convection from the recirculating hot gases and by radiation

from the combustor walls and hot flame in the combustor. Many chemical and transport processes occur in a coal flame. Pyrolysis is the initial reaction step that occurs in a coal particle. Primary pyrolysis products include light gases, char, and tar, which is a gas mixture of heavy-molecular-weight hydrocarbons at high temperatures and condensable at room temperature. Simultaneously, the volatile matter released in the gas phase may also undergo secondary reactions. Soot is believed to be one of the products of these secondary reactions. The tar from primary pyrolysis consists of many polycyclic aromatic hydrocarbons (PAH). These hydrocarbon molecules are very likely to undergo both cracking and polymerization processes at high temperature. As first proposed by McLean, et al. (1981) and Seeker, et al. (1981), tar is a precursor of soot in coal flames.

Importance of Soot in Coal Combustion

Soot in coal flames is important to combustion systems because of its radiative heat transfer effects. On a mass basis, there is much less soot present in a coal flame than other solid particles such as char and ash. However, the small size of soot particles results in a large total surface area. The importance of coal-derived soot in radiative heat transfer has been addressed by several researchers (Mengüç and Viskanta, 1987, 1988; Ahluwalia and Im, 1994). In a computational study of radiative heat transfer in a 915 MW coal-fired furnace by Ahluwalia and Im (1994), where 10% of the volatile matter was assumed to be transformed into soot, it was found that the soot particles significantly enhanced radiative heat transfer. In spite of the fact that soot particles are only present in the flame zone, the calculated total radiative heat transfer was about 10% higher if soot was included in addition to gas, char and ash. This increase in heat transfer corresponded to an 80 K difference in exit gas temperature. It can be expected that in the presence of a large radiant surface area of soot, the near-burner flame temperature could be lowered several hundred degrees due to the heat transfer to the surrounding walls (see Appendix A for a sample estimation). A major problem in pulverized coal combustion is the

formation of nitrogen oxides (NO_x) which are generated (a) through the reaction of nitrogen and oxygen in air at elevated temperatures (called thermal NO_x), and (b) from the nitrogen-containing species or groups in the fuel (called fuel NO_x). It has been found that the production of both thermal and fuel NO_x in coal combustion is a strong function of reaction temperature. Therefore, the existence of soot in a coal flame will affect NO_x formation. Also, it has been reported that soot from coal pyrolysis contains nitrogen (Chen, et al., 1992), and therefore soot is an additional pathway for fuel nitrogen evolution.

Questions to Be Addressed

Although soot formation and its importance in coal combustion and pyrolysis have been known to the combustion community for a long time, extensive characterization of coal-derived soot has not been performed. Most of the published research deals with soot generated during coal pyrolysis in inert conditions (i.e., in nitrogen, argon, or helium). Results from these experiments will be reviewed in Chapter 2. However, the mechanism of soot formation in coal combustion is still not clear because the flame environment in a practical furnace is not an inert environment. Oxygen-containing species (e.g., H_2O , CO_2 and OH radical) in the coal flame may affect the conversion of tar to soot. According to most of the suggested soot formation mechanisms obtained from hydrocarbon combustion experiments, the stability of PAH in the process of soot formation significantly affects final soot yield. High temperatures reduce the stability and cause decomposition or cracking of PAH. Oxygen-containing species may also attack PAH and cause the rupture of aromatic ring structures. Therefore, the soot yield data obtained from coal pyrolysis experiments in inert conditions may not represent what happens in a practical furnace.

The differences in formation and properties between coal-derived soot and the soot from pure hydrocarbon flames also needs to be clarified. The soot formation process

in coal pyrolysis should be related to the pyrolysis of aromatic hydrocarbons because tar is basically a mixture of PAH. On the other hand, soot formation in coal pyrolysis should be different from that in ordinary hydrocarbon pyrolysis due to the existence of a large number of PAH species in tar. The mixing of different hydrocarbon compounds may promote soot formation (Kern and Xie, 1991). Since the origin of soot in coal pyrolysis and combustion is different from those of pure hydrocarbon flames, the properties of coal soot may also be different from those of conventional hydrocarbon soot. The sizes of individual soot particles and soot agglomerates, as well as the structure of the soot agglomerates, are of great importance in radiative transfer calculation and in interpreting the soot volume fraction from laser diagnostics.

Heteroaromatic compounds containing O, S, and N are found in coal tar, but not in most simple hydrocarbon fuels. They are probably also involved in the soot formation mechanism. Therefore, the chemical properties such as elemental compositions of soot need to be further investigated. Special attention should be paid to the nitrogen content of soot because it is related to coal nitrogen evolution.

Objectives of This Research

Comprehensive coal combustion models should account for soot chemistry and the effects soot on radiation and nitrogen evolution. Soot properties such as size and optical constant are required in order to perform heat transfer calculations. It is desirable to understand the soot formation mechanism, and how soot properties and kinetics are related to reaction conditions and coal rank. Knowledge of the size, chemical properties, formation rate, and basic mechanism of coal-derived soot formed in conditions comparable to those in practical furnaces is essential to the accurate predictions of flame temperature, NO_x formation rate and other important parameters in coal combustion systems.

While the origin of soot in coal flames has been verified by the pyrolysis experiments in inert conditions, data regarding soot properties and soot formation during coal pyrolysis *in flame environments* are nearly nonexistent. The ultimate goal of this research is to generate the experimental data and to obtain detailed information about soot formation in conditions similar to those encountered in pulverized coal flames. This information can eventually be incorporated into comprehensive coal combustion models to give accurate predictions of combustion characteristics and pollutant formation. To complete this ultimate objective, five tasks have been identified:

- 1) Construction of a coal pyrolysis experimental facility which simulates the environment in a practical pulverized-coal-fired furnace and allows optical and probe access for the examination of char, soot, and gas species.
- 2) Examination of the physical and chemical properties of soot derived from coal tar, and comparison of the coal-derived soot to the soot from conventional hydrocarbon flames.
- 3) Determination of soot yields in flame environments as a function of temperature, residence time, and coal rank, and investigation of the effect of gas-phase composition on soot yield.
- 4) Investigation of tar evolution and secondary pyrolysis chemistry to help develop empirical kinetic models for soot formation, agglomeration, and oxidation.
- 5) Examination of nitrogen incorporation into soot.

Chapter 2

LITERATURE REVIEW

The general mechanisms of soot formation and oxidation will be reviewed based on the studies of simple hydrocarbon pyrolysis and combustion, due to the scarcity of relevant knowledge of coal-derived soot. The large amount of research on soot in simple hydrocarbon flames provides background for understanding soot formation in coal combustion. Secondary reactions of coal volatiles and nitrogen evolution due to secondary reactions are reviewed later in this chapter, followed by a brief review of soot sampling techniques.

General Mechanisms of Soot Formation and Oxidation for Simple Hydrocarbons

Structure and Properties of Soot

Soot emitted from typical hydrocarbon pyrolysis and combustion systems consists of agglomerates of a number of “primary spheres” whose diameters are typically in the range of 10 to 50 nm for a wide variety of conditions (Haynes, 1991; Saito, et al., 1991). These primary spheres typically exhibit a size distribution. It has been reported that the mature soot has similar physical and chemical characteristics regardless of fuel precursor or conditions of formation, although the pathways to form the mature soot are different (Saito, et al., 1991). The earliest particles may have diameters as small as 2 nm (Haynes and Wagner, 1981). The morphology of soot particles collected from the flames of various fuels has been studied using scanning electron microscopy (SEM) and transmission electron microscopy (TEM). According to Megaridis, et al. (1989) and Saito, et al. (1991), the earliest particles from methane and benzene flames appear as

irregularly shaped pieces with sharp edges, while later particles contain chain-like agglomerates of individual spheres.

The internal structure of soot particles has also been examined by high-resolution phase-contrast electron microscopy (Haynes, 1991). Near the edge of the particle, bent carbon layers follow the shape of the particle surface. Inside the particle, lattice structures seem to be located more or less regularly around certain centers, between which the structure is less ordered. Many dislocations and other lattice defects are present. Heat treatment improves the internal order of the particles, and the interplanar spacing approaches that of graphite. The rate of graphitization depends on temperature, so that the age of a particle and its degree of order are closely linked. For soot particles at high temperatures, some ordering may occur as the particles continue to grow.

Chemically, soot mainly consists of carbon but also contains hydrogen and other elements. Young soot particles from simple hydrocarbon fuels have C/H mole ratio as low as 1, while mature particles have a C/H ratio in excess of 10. In contrast, the soot collected by Chen (1991) from coal pyrolysis exhibited C/H ratios ranging from 2 to 9.5. Saito, et al. (1991) used X-ray photoelectroscopy (XPS) to determine whether the soot samples were primarily aromatic or non-aromatic compounds. They found that the earliest particles from methane and benzene flames were non-aromatic, changing to aromatic at higher residence times in the flame. Oxygen, both adsorbed and bound to carbon, was also found in the samples. A large fraction of oxygen was chemically bound to carbon atoms, but not incorporated into the aromatic rings. The ratio of oxygen to carbon decreased dramatically with increasing time in the flame. Nitrogen was found in the structure of soot from coal pyrolysis (Chen and Niksa, 1992c), but has not been reported in the soot from simple hydrocarbon fuels that do not contain nitrogen.

Soot Formation Stages

Soot formation is a very complicated process involving hundreds of elemental steps. Qualitatively, there are three stages that lead to a primary soot particle: a) particle inception or nucleation; b) surface growth; and c) coagulation (Haynes, et al., 1980). After these three stages, however, the primary particles may continue to undergo d) agglomeration and e) aggregation processes (Nenniger, 1986). During *particle inception*, the first condensed phase material arises from the fuel molecules and their oxidation or pyrolysis products. Such products typically include various unsaturated hydrocarbons, especially acetylene and PAH. These two types of molecules are often considered the most likely precursors of soot in flames. Once the first particles are formed, the soot loading (the mass of soot per unit volume) can be increased by *surface growth*, which involves the attachment of gas-phase species (mainly acetylene) to the surface of a particle. Surface growth reactions lead to an increase in the amount of soot, but leave the number of particles unchanged. *Coagulation* also leads to particle growth, where particles collide and coalesce. Although the number of particles is decreased, the soot volume fraction remains constant during the coagulation process. At later stages in the growth process, particles no longer coalesce on collision, but are chemically fused together in chains. Primary particles are discernible in the chains. The growth by non-coalescent collision is known as *agglomeration*. Usually, agglomerates can subsequently become entangled with other agglomerates through a process known as *aggregation*. All these processes are reviewed below.

Particle Inception

The first stage of soot generation is particle inception. This process appears to be a continuation of the PAH growth processes, and is of critical importance in overall soot formation (Haynes, et al., 1980). As mentioned above, the smallest identifiable particles observed in luminous flames have diameters in the range 1.5 to 2 nm and a mass on the

order of 1000 amu. It is the generation of such particles from the initial gas-phase reactants that constitutes the particle inception process. The identical chemical character of the mature soot formed from diffusion or premixed systems would seem to suggest that there is a similarity in the chemical mechanisms for soot formation.

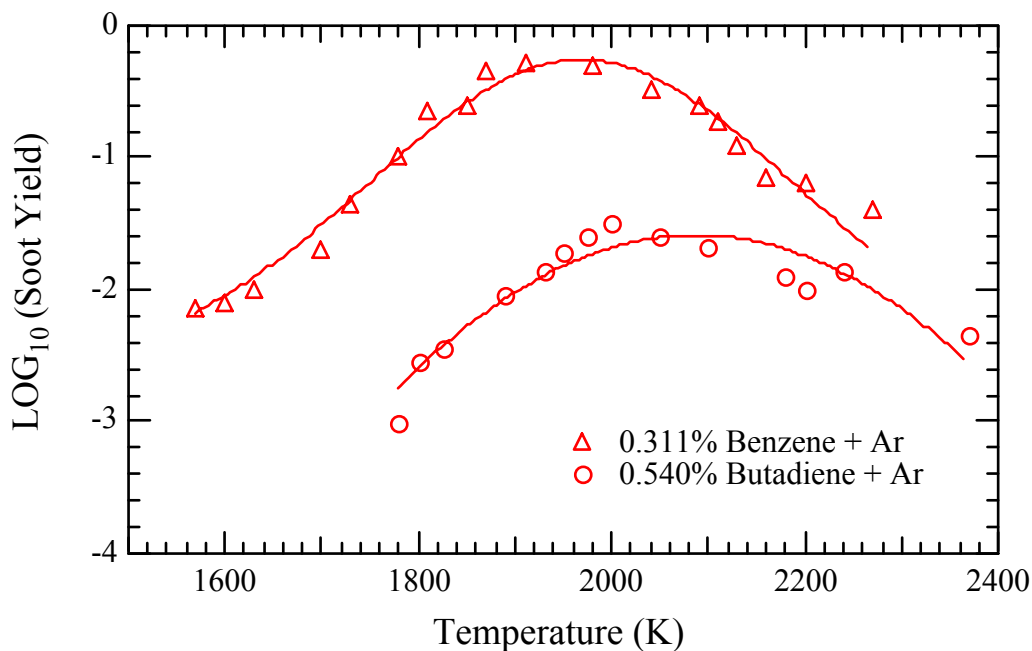


Figure 2.1. Soot yields versus temperature (from Frenklach, et al., 1986).

Many experiments have been conducted in search of soot formation mechanisms using different hydrocarbon fuels, various combustor configurations (such as premixed flames, diffusion flames, flat flames and shock tubes), and either combustion or pyrolysis conditions. An interesting phenomenon was observed in almost all experiments. Soot yields were found to initially increase with increasing reaction temperature, and then decline. In other words, plots of soot yield versus temperature are bell-shaped, as displayed in Fig. 2.1. To explain the underlying principles of molecular growth pertaining to soot formation, mechanisms involving ions, ring growth, polyacetylene chains, Diels-Alder reactions, and neutral radicals have all been proposed. According to

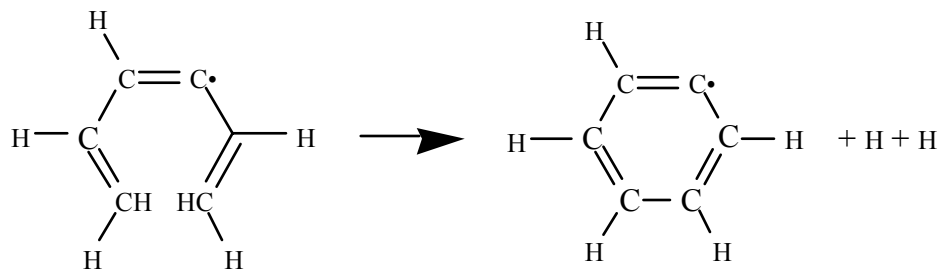
a review paper by Glassman (1988), there is a general acceptance that the mechanism proposed by Frenklach, et al. (1984, 1986) correctly describes the chemical history of formation of a soot nucleus. The Frenklach model ascribes no role to ions in soot formation. There is strong evidence that chemions exist in hydrocarbon diffusion flames, and this has led to a lively controversy concerning the importance of ions in forming soot. This controversy continued until the experiment conducted by Bertrand and Delfau (1985), suggesting that chemions had little, if any, effect on the production of soot.

The Frenklach model is a detailed kinetic model containing about 600 possible elementary reversible reactions and about 180 species. The principal routes for the particle inception include the formation of the first aromatic ring, the formation of two-ring aromatics and the further growth of fused polyaromatics. The cyclization reactions are of two classes: non-radical and radical cyclizations. The latter can be further subdivided into: a) cyclization of more stable radicals; b) cyclization of less stable radicals; and c) radical cyclization via interaction of an unpaired electron with a triple bond. The computational results indicated that reaction (c) has several orders of magnitude more forward flux than reactions (a), (b), and the non-radical cyclizations. The major reaction pathways for the formation of the first aromatic ring are illustrated in Fig. 2.2. About 10 essentially different pathways were considered for the formation of two-ring aromatic species. The dominant route is presented in Fig. 2.3.

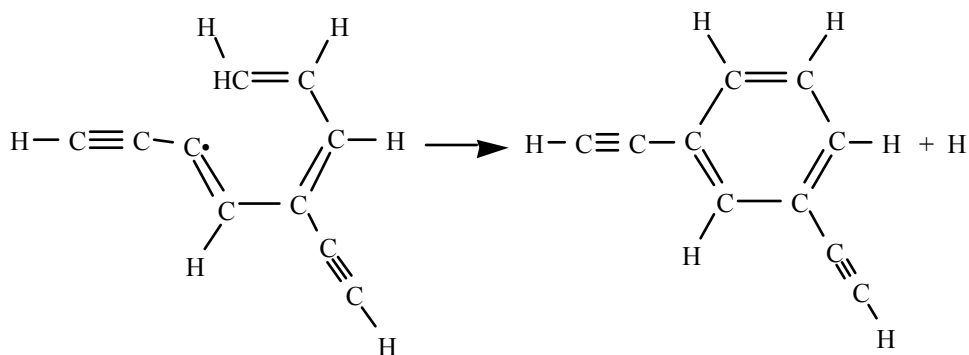
Two main pathways for the further growth of fused polycyclic aromatics considered by Frenklach, et al. (1984, 1986) are shown in Fig. 2.4. Although the mechanism stops at pyrene and cyclopenta[cd]pyrene in the figure, both routes can continue to eventually form coronene ($C_{24}H_{12}$).

The Frenklach model can simulate the bell-shaped soot yield versus temperature profile (see Fig. 2.1). As for the nature of the soot-yield bell, the computational results supported the conjecture that the competition between kinetic and thermodynamic factors

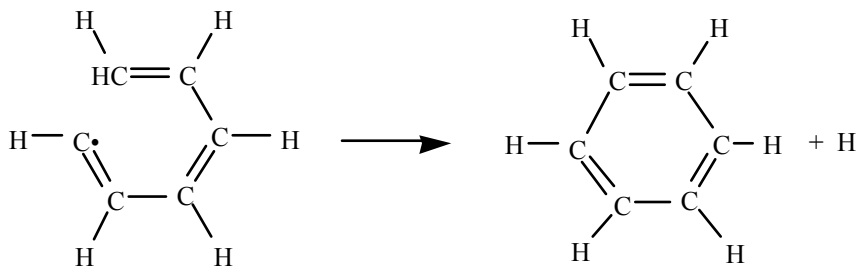
is responsible for the bell-shaped phenomenon. At the lower temperature bound of the



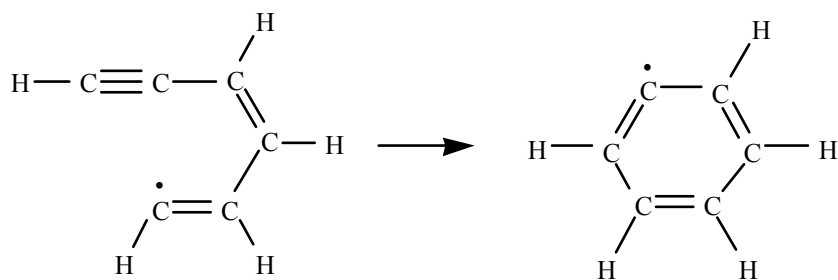
Nonradical cyclization



a) Cyclization of more stable radicals



b) Cyclization of less stable radicals



c) Radical cyclization via interaction of an unpaired electron with a triple bond

Figure 2.2. Postulated mechanisms for the formation of the first aromatic ring.

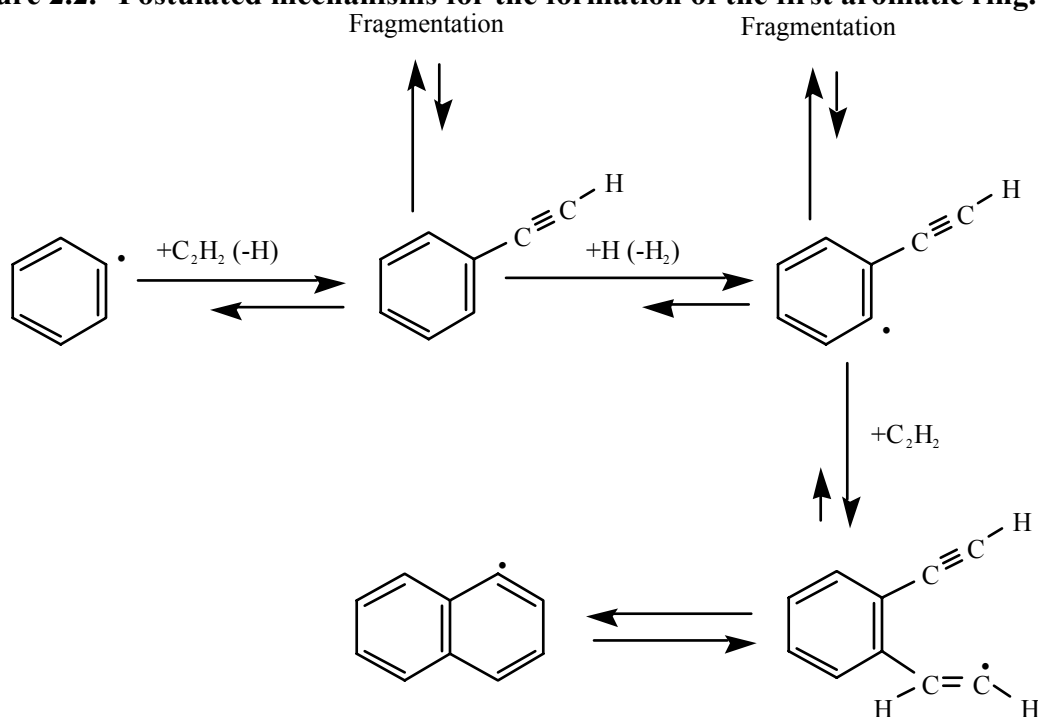
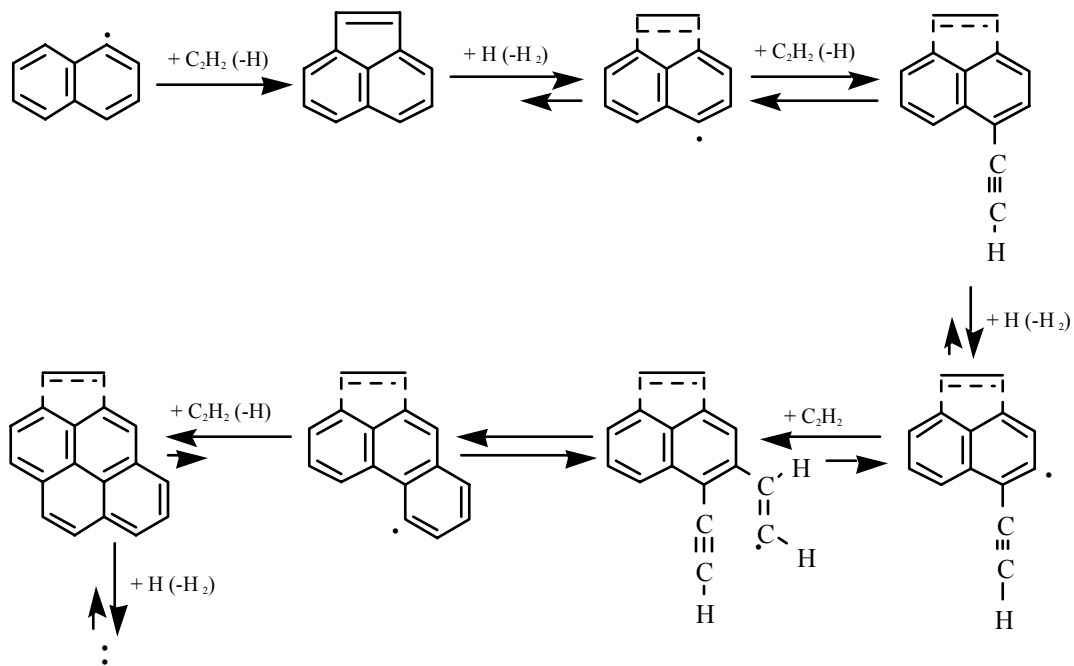


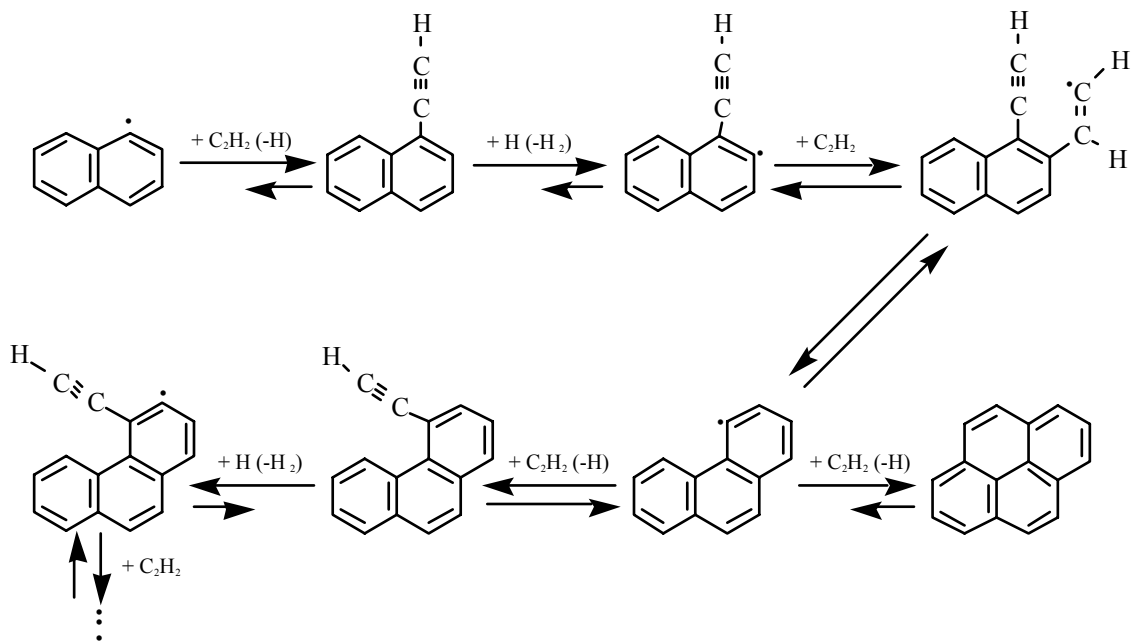
Figure 2.3. Principal reaction pathway for formation of two-ring aromatics.

bell, the pyrolysis reactions are rate controlling. As temperature increases, the thermodynamic stability of the intermediates, particularly of small aromatic radicals, decreases and eventually limits the soot yield. For aromatic hydrocarbon fuels at higher temperature, direct condensation of parent aromatic molecules becomes less important than the dissociation of the aromatic molecules to smaller molecules, which then participate in forming soot. Frenklach's computations showed that the bottleneck of soot formation for non-aromatic fuels appears at the formation of the first aromatic ring. Different fuel molecular structures influence the growth process only at its early stages, in two respects: (1) they provide different reaction partners for the formation of aromatic molecules; and (2) they affect the generation of hydrogen atoms. At late stages, the dominant growth mechanism is by the addition of acetylene. Based on Frenklach's findings, it can be expected that coal type will affect soot inception because the

molecular



Route 1



Route 2

Figure 2.4. Principal reaction pathways for formation of fused polycyclic aromatics.

structures in the coal tar are rank dependent. The profile of soot yield versus temperature should also be bell-shaped, which is different from what is reported in coal pyrolysis experiments (to be discussed later).

The first version of the Frenklach model assumed infinitely long reaction sequences. The computed soot yield was defined as the number of carbon atoms accumulated in the soot divided by the initial number of carbon atoms of hydrocarbons. It did not account for the soot growth mechanisms such as physical condensation, surface reaction, and particle coagulation, and therefore provided only a lower-limit estimate of soot yield. A more recent version included the surface growth and particle coagulation (Frenklach and Wang, 1990).

Surface Growth

The surface of hot soot particles readily accepts hydrocarbons from the gas phase. Surface growth can occur at lower temperatures than the temperature at which the initial soot particles are generated (Haynes, et al., 1980). The high reactivity of the soot surface is such that the presence of soot can accelerate the decomposition of benzene and acetylene in pyrolysis. In methane pyrolysis, the surface rate of deposition on soot particles is an order of magnitude higher than it is on aluminum or graphite.

It has been suggested that the main species being attached to the surface are acetylene and polyacetylene. Frenklach and Wang (1990) modeled the surface reactions as follows:



where $C_{soot}H$ and C_{soot}^*H represent an arm-chair site on the soot particle surface and $C_{soot} \cdot$ represents the corresponding radical. Estimation of the rate coefficients for the

above heterogeneous reactions was based on analogous gas-phase reactions of two one-ring aromatics (benzene and phenyl radical).

Coagulation

Particle coagulation is a result of the collision and sticking of particles undergoing Brownian motion, and leads to an increase in the characteristic dimension of the particles without affecting the soot loading. Typically, particle collisions are effectively coalescent for particles with diameters up to several hundred Angstrom units. Theoretically, the decrease in the number of particles can be expected to occur according to the Schmoluchowski equation (Haynes, et al., 1991):

$$\frac{dN}{dt} = -k(d)N^2 \quad (2.4)$$

where the rate constant, k , depends on the particle diameter, d . According to the molecular theory, the equation can be expressed as:

$$\frac{dN}{dt} = -\frac{6}{5}k_{theory}f_v^{1/6}N^{11/6} \quad (2.5)$$

where

$$k_{theory} = \frac{5}{12} \left(\frac{3}{4\pi} \right)^{1/6} \left(\frac{6kT}{\rho} \right)^{1/2} G\alpha \quad (2.6)$$

and

f_v is the particle volume fraction,

ρ is the density of particles,

G is a factor to account for inter particle dispersion forces and can be expected to have a value of about 2 for spherical particles.

α is a weak function of particle size distribution, varying from 5.66 to 6.55.

Hodges, et al. (1987) also modeled the particle coagulation by free molecule Brownian collision kinetics.

Agglomeration and Aggregation

While many researchers have found that soot formed in either hydrocarbon flames (Megaridis, et al., 1989), the combustion chamber of a diesel engine (Kawamura, et al., 1987), or a coal pyrolysis reactor (Nenniger, 1986) existed in chain-shaped agglomerates, the agglomeration and aggregation processes have not been well characterized. Most of agglomerates in hydrocarbon flames consist of only 10 to 50 primary particles, as reported by Megaridis, et al. (1989) and Prado, et al.(1976). However, in certain circumstance such as microgravity, soot agglomerates as large as 0.1 mm in diameter can be formed, as reported by Ito, et al. (1994). In Ito's experiment, large luminous spots were found in a thin annular region of a gaseous butane diffusion flame. The long residence time of a soot particle in that region due to negligible free convection accounted for the formation of large agglomerates. Jackson, et al. (1992) also observed the existence of large soot agglomerates or aggregates when burning heptane and heptane/monochloroalkane mixture droplets suspended on a quartz needle at low gravity. In the process that led to the formation of those agglomerates, a soot shell structure was observed between the diffusion flame boundary and the vaporizing droplet. They ascribed the accumulation of soot particles in the shell structure to the balance between the inwardly directed thermophoretic forces and the outwardly directed drag forces generated by the Stefan flow.

Soot Oxidation

The oxidation of soot aerosol particles in a flame environment is rather difficult to examine experimentally. In the case of oxidation by O₂, the semiempirical formula by Nagle and Strickland-Constable (1962) correlated the oxidation rate measurements of pyrolytic graphite,

$$\frac{\omega}{12} = \left(\frac{k_A P_{O_2}}{1 + k_z P_{O_2}} \right) x + k_B P_{O_2} (1 - x) \quad \text{g-carbon/cm}^2\text{s} \quad (2.7)$$

where ω is the reaction rate per surface area and x is given by

$$x = \left(1 + \frac{k_T}{k_B P_{O_2}} \right)^{-1} \quad (2.8)$$

$$k_A = 20 \exp(-125/RT) \quad \text{g-atom cm}^{-2} \text{ sec}^{-1} \text{ atm}^{-1} \quad (2.9)$$

$$k_B = 4.46 * 10^{-3} \exp(-63.6/RT) \quad \text{g-atom cm}^{-2} \text{ sec}^{-1} \text{ atm}^{-1} \quad (2.10)$$

$$k_T = 1.51 * 10^{-5} \exp(-406/RT) \quad \text{g-atom cm}^{-2} \text{ sec}^{-1} \quad (2.11)$$

$$k_Z = 21.3 \exp(17.2/RT) \quad \text{atm}^{-1} \quad (2.12)$$

$$R = 0.00831 \text{ MJ/kg mole} \quad (2.13)$$

This correlation was verified by Radcliffe and Appleton (1971) and Park and Appleton (1973) to be applicable to soot oxidation.

In a flame environment, about 10% of the collision of OH radicals with soot particles are effective in gasifying a carbon atom (Haynes, 1991). Frenklach and Wang (1990) used a collision efficiency of 0.13 to model the soot oxidation by OH radical. Puri, et al. (1994) studied the oxidation of soot in hydrocarbon diffusion flames. They found that the reactivity of soot (in terms of collision efficiency) decreased with increases in temperature, probably due to thermal annealing or radical site stabilization processes. It was also found that the OH radical was the dominant oxidizer of soot, with O₂ making only a small contribution in diffusion flames. While the collision efficiency may vary with flame conditions, an average value of 0.1 gives reasonable estimations (Wang, 1994).

The oxidation of soot by oxygen-containing species affects the surface growth of soot particles. In Frenklach and Wang's model (1990), the following two reactions were added:



Soot from Secondary Reactions of Coal Volatiles

Volatiles released from primary coal pyrolysis contain PAH, which are susceptible to secondary reactions to form soot. Secondary reactions are complex, being influenced by coal type, heating rate, residence time, temperature, intra- and extraparticle heat and mass transfer, and physical structures of the reacting coal such as porosity, swelling, and softening properties (Serio, et al., 1987). Most of the studies on secondary coal pyrolysis chemistry have been conducted in inert environments.

Experiments in Inert Conditions

Several investigators have examined the pyrolysis of model compounds that are representative of coal tar. Wornat, et al. (1992) examined anthracene as a model coal-derived aromatic compound. Bruinsma, et al. (1987) studied the pyrolysis of many aromatic compounds using a coiled tube flow reactor. Bruinsma and coworkers found that benzene and its derivatives start to decompose in a temperature range from 800 to 1100 K. The thermal stability of benzene derivatives was found to increase in the following sequence: methoxy < thio < propyl < ethyl < carbaldehyde < ethenyl < hydroxyl < methyl < phenyl \approx cyano < benzene. For heterocyclic compounds, thermal stability followed the sequence: furan < cyclopentadiene < pyrrole < pyridine < benzene < thiophene.

Serio, et al. (1987) investigated kinetics of secondary reactions of fresh coal tars. The experiment consisted of two tubular reactors connected in series. The primary tar was generated in the first reactor by heating a helium-swept, shallow packed bed of a bituminous coal from room temperature to 550 °C at a heating rate of 3/min. It was found that secondary reactions were insignificant for these conditions. The primary tar was then introduced to the secondary reactor, maintained at a constant temperature between 500 and 900 °C, where decomposition reactions occurred. Extensive tar conversion (30-50%) was observed at 700-800 °C, with light gases as the major products.

Doolan, et al. (1987) used quartz tubular reactors to study secondary cracking of the tar vapors generated in a fluidized bed pyrolyzer. The cracking reaction temperatures were changed from 870 K to 1370 K. At 870 K, very little cracking occurred. As the cracking temperature was raised, the light hydrocarbon yields increased rapidly. Products were predominantly alkenes, with smaller yields of methane and benzene. At higher temperatures, the light hydrocarbon yields passed through a maximum and eventually declined, while acetylene became the major product. The cracking reaction experiments were also conducted using a shock tube reactor. Products such as acetylene, benzene and carbon monoxide were observed. No carbon dioxide was produced from the cracking of the tar. Along with gases, liquid product defined as secondary tar, and solid product believed to be soot, were also observed. However, the yields of liquid and solid products were not reported separately.

The chemical structures of tars that experienced secondary reactions in nitrogen were examined using ^1H NMR and ^{13}C NMR by Fletcher, et al. (1990) and Pugmire, et al. (1991). The pyrolysis experiments were carried out in an electrically-heated drop-tube furnace at 1050 K and 1250 K. The collected tars showed increases in multiple ring structures and decreases in aliphatic content with increases of temperature and residence time. The increased hydrogen aromaticity of tar might lead to the formation of soot nuclei.

Freihaut, et al. (1993) used a flash lamp reactor to study tar evolution and secondary cracking for a bituminous coal. At low irradiance flux levels, only tar and low temperature decomposition gases were observed. At high irradiance levels, significant quantities of secondary decomposition product gases (HCN , C_2H_2 , and CO) were observed. They believed that the high temperature cracking reactions could occur at the particle surface or in the particle-gas boundary layer.

Nenniger, et al. (1983, 1986) studied the sooting potential of several coals by separating aerosol from char particles after the pyrolysis of coals in a laminar flow

furnace. The pyrolysis was carried out in an inert atmosphere of preheated argon. The separation system consisted of a virtual impactor in series with a cascade impactor. The separation efficiency was checked by SEM, whereas no quantitative efficiency measurement was conducted. The aerosol was believed to consist of extractable tar, soot and condensed ash. The tar yield was assumed to be the amount of the aerosol extractable with methylene chloride. The condensed ash content was determined from neutron activation analysis. The soot yield was calculated by difference. They found that the soot yield increased while the tar yield decreased as the pyrolysis temperature was raised. The sum of soot plus tar remained constant with increasing severity of pyrolysis. At a high temperature (2200 K), about 20 wt % of a dry high-volatile bituminous coal was converted to soot. Soot inside char particles was also observed under TEM by crushing the char particles. This seems to suggest that the actual soot yields might be higher.

Wornat, et al. (1987) investigated changes in the composition of polycyclic aromatic compounds (PAC) from the pyrolysis of a high-volatile bituminous coal in argon. Overall, a loss in compositional complexity was observed as the severity of secondary reactions increased, suggesting the selective survival of a group of stable species. The stable species were identified as unsubstituted PAC. PAC reactivity followed the following order: aromatic amines > aromatic ethers \approx multialkylated PAC \approx phenols > monoalkylated PAC > unsubstituted PAC > carbonyl-substituted PAC. For the high volatile bituminous coal studied, about 20 wt % of the coal was converted to soot at high temperatures and long residence times. In addition, the fact that the sum of PAC and soot yields was relatively constant suggested that PAC served as precursors to soot.

Recently, Chen and coworkers (Chen, 1991; Chen and Niksa, 1992a, 1992b, 1992c) performed coal pyrolysis experiments in an inductively-heated radiant drop-tube furnace in an inert argon atmosphere. They also found that the yields of tar/oils plus soot in the secondary pyrolysis experiments were constant and were equal to the tar-plus-oil

yields obtained at the longest residence time in primary pyrolysis experiments. For a high-volatile bituminous coal at higher temperatures, more than 25% of the coal mass (daf) was converted to soot. For gas-phase products, C₃ hydrocarbons and ethane decreased monotonically with temperature, while methane and ethylene reached maxima and then dropped. Acetylene increased dramatically during soot formation and growth. The high soot yields reported by Nenniger, et al. (1983), Wornat, et al. (1987) and Chen (1991) were probably due to the inert conditions, since no destruction occurred by oxygen-containing species. The profiles of soot yield versus temperature in these coal pyrolysis experiments were not bell-shaped; the soot yields increased with temperature monotonically. Table 2.1 summarizes their experimental results.

Table 2.1. A summary of coal pyrolysis experiments conducted by three investigators.

Investigator	Nenniger (1986)	Wornat, et al. (1987)	Chen (1991)
Pyrolysis Environment	In Argon	In Argon	In Argon
Reactor	Drop-Tube, Electrically-Heated	Drop-Tube, Electrically-Heated	Radiant Drop-Tube
Pyrolysis Temperature (K)	1300 to 2200	1130 to 1480	1480 to 1740 ^a
Soot Yield	Increases with temp. Reaches a plateau	Increases with temp and residence time	Increases with temp and residence time
Tar Yield	Decreases with temperature	Decreases with temp and residence time	Decreases with temp and residence time
(Soot+Tar) Yield	Remains unchanged	Remains unchanged	Remains unchanged

^a Temperatures reported by Chen were reactor wall temperatures. The particle temperatures were hundred degrees lower.

Experiments in Combustion Gases

Only a few studies have been performed on secondary chemistry of coal tar in oxidizing or reducing conditions. These studies show that in certain flame environments, oxygen-containing species will cause the destruction of PAH. Haynes (1991) investigated the decomposition of pyrene injected into the post flame gases ($T \sim 1700\text{K}$) of near-sooting and slightly sooting ethylene/air flames at atmospheric pressure. In the most fuel rich, sooting flame, no decomposition of the pyrene occurred over extended reaction times. At more fuel lean flame conditions, significant decomposition of the pyrene occurred. It was argued that the pyrene decomposition was due to reaction with OH radical.

Soot formation around an individual pulverized coal particle was observed by McLean, et al. (1981) using a methane/hydrogen/air flat flame reactor. For bituminous coals, ejected volatile matter formed a condensed soot-like phase, which was oxidized during the early stage of char burning under oxidizing conditions and that persisted throughout the reactor under reducing conditions. For lignite coals, a condensed phase was not observed, since lignite volatiles are largely composed of light gases instead of high-molecule-weight hydrocarbons. Seeker, et al. (1981) performed similar research using a down-fired methane/air flat flame, running in a lean (35% excess air) condition. They found that both particle size and coal rank affected the sooting tendency. For large bituminous particles (80 μm), a significant volatile fraction was ejected from the particle as a jet. This volatile jet reacted close to the particle, producing a trail of small solid particles believed to be soot. Tails of soot were not observed for lignite, anthracite, and small bituminous particles. Timothy, et al. (1986) studied the formation and burnout of soot during the combustion of three high-volatile bituminous coals using a combination of high-speed photography and two-color optical pyrometry. Soot was observed to form in a nearly spherical shell displaced from the particle surface by one to four particle radii. The overall soot cloud diameter was approximately constant, but the shell thickness

increased with decreasing oxygen concentration. The peak soot concentration ranged from 0.5% of the mass of coal (at oxygen concentrations greater than 50%) to 3% (at a lower concentration of 10% oxygen). Several models have also been developed to describe the volatiles flames around individual particles as a result of these experiments (e.g., Musarra, et al., 1986; Lau and Niksa, 1993). In these models, thermophoresis and radiation accounted for the transport processes of soot near the particle.

Nitrogen Evolution Due to Secondary Reactions

Several sets of research have been conducted on the evolution of nitrogen in coal pyrolysis (Axworthy, et al., 1978; Solomon, et al., 1978; Freihaut, et al., 1982; Nelson, et al., 1991; Chen and Niksa, 1992d; Kambara, et al., 1993). Most of the research concentrated on the nitrogen distribution in tar, char and gas, and how the nitrogen-containing species were destroyed to form precursors of nitrogen oxides. NH_3 and HCN were believed to be the precursors of fuel NO_x . Regarding the effect of coal rank, some studies report that coal type and coal composition have little effect on the nitrogen distribution, while others argue that coal rank is related to nitrogen functionality, which determines the nitrogen evolution. The study conducted by Solomon, et al. (1978) on a lignite and 12 bituminous coals suggested that at low temperature, where no secondary reaction occurs, the fraction of coal nitrogen in tar is the same as the fraction of the coal that yields the tar, and the chemical compositions of tar and parent coal are similar. Kambara, et al. (1993) investigated the nitrogen evolution for 20 coals covering wide ranks. Three nitrogen functional forms of pyrrole type, pyridine type, and quaternary nitrogen were observed for all coals. They found that the quaternary nitrogen converts finally to NH_3 , and a portion of the pyrrolic and pyridinic type nitrogen converts to HCN.

The stability of fuel-nitrogen compounds has been investigated in both coal pyrolysis (Nelson, et al., 1991) and model compound pyrolysis studies (Houser, et al., 1980; Mackie, et al., 1990, 1991). These studies revealed that the reactivities of pyrrolic

type structures are greater than those of pyridinic type structures. It was also reported that the sooting tendency of pyridine was very low compared to that of benzene, although pyridine has considerable aromatic character (Kern and Xie, 1991). However, few studies have been performed on the effect of soot on the evolution of nitrogen.

Wornat, et al. (1988) studied the changes in the ring number composition of nitrogen-containing polycyclic aromatic compounds (PACN) and soot nitrogen during pyrolysis. They found that the mass distribution and rate of decay of the PACN followed the order: five ring > six ring > four ring > three ring > two ring. It was also found that the PAC conversion reactions leading to ring build up, ring rupture, and soot formation were faster for PACN relative to the nonpolar PAC, because C-N bonds within the coal's aromatic rings were weaker than the C-C bonds. Elemental analysis also showed that the N/C ratio in the soot dropped with increasing PAC conversion. The percentage of coal nitrogen evolved in soot declined with the increase of pyrolysis severity, while the soot yield increased. It was argued that this decline was due to nitrogen liberation from the soot generated, and soot growth resulting from the conversion of PAC with successively lower nitrogen content.

Recently, Chen, et al. (1992) examined soot and nitrogen evolution in coal pyrolysis. Their experimental results showed that tar aromaticities increased dramatically, reaching ultimate values greater than 0.67. The C/H mole ratio in the soot changed from 2 to 10 when residence time was increased. Up to one-fourth of the coal-nitrogen expelled in volatiles during primary devolatilization was incorporated into soot during secondary pyrolysis for coals whose volatiles were dominated by tar. Ten percent was incorporated for a subbituminous coal. All nitrogen was incorporated into soot early in the secondary pyrolysis process, and the total amount of coal-nitrogen in soot remained constant even when soot yields increased dramatically with increases in residence time.

A global mechanism of soot formation was proposed by Chen, et al. (1992) as shown in Fig. 2.5. Here, all reaction pathways are irreversible. In earlier stages, R₂ is the major pathway for soot formation, and nitrogen-containing compounds are incorporated in soot. Thereafter, substantial soot mass is added via R₃. Direct tar addition to soot in later stages is possible only if tars eliminate their nitrogen before getting added to the soot.

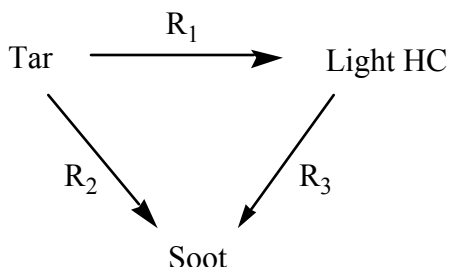


Figure 2.5. Possible reaction pathways for soot generation in coal pyrolysis (Suggested by Chen, et al., 1992).

Soot Sampling Techniques

Soot particle sizes are commonly determined by collecting the soot from an experimental coal pyrolysis reactor, followed by observation using an electron microscope. Several different methods for soot collection have been reported in the literature. Saito, et al. (1991) used a fine quartz needle to collect soot samples from hydrocarbon diffusion flames. The quartz probe provided good soot samples with minimal disturbance of the flame for both visual observation and for observation under an optical microscope. However, this method is inappropriate for SEM or TEM because of the poor conductivity of the quartz. Saito and coworkers also used a mesh screen of stainless steel, which allowed the observation using SEM. Prado, et al. (1976) collected soot from a turbulent flow combustor with a stainless steel, water-cooled and water-flushed probe, in which a small amount of water was injected into the sampled gas to quench the reactions. The carbonaceous residue was collected on a filter. It was then

removed from the filter, dispersed in an ultrasonic bath, and deposited on perforated carbon electron microscope grids for visualization and size distribution analysis. A sonic suction probe was employed by Harold, et al. (1990) to collect soot for TEM examination from an optical fiber preform torch. The use of water-cooled probes and sonic suction probes necessitates the transfer of soot onto the microscope grids. In addition, these probes are not small enough to avoid disturbance of the flames. Nenniger (1986) used an electrostatic precipitator to collect soot particles generated in a flow reactor after being nitrogen-quenched and separated from char particles. In her experiments, samples were deposited on carbon-coated copper grids that were held in place in the precipitator by tape, and the deposited samples were also subsequently examined with a transmission electron microscope. One disadvantage of this method is that the soot particles were not extracted from the reactor directly and soot size or shape may have been altered after the quench and separation.

Thermophoretic sampling provides a method to capture the soot particles directly on the surface of a microscopic grid, with minimal flame disturbance. Dobbins and Megaridis (1987) devised a refined thermophoretic sampling system to collect the soot from an ethene coannular diffusion flame. Figure 2.6 shows a TEM micrograph of soot particles extracted from the ethene flame. In their experiments, a TEM grid was attached to a small probe whose insertion into the flame was controlled by a special pneumatic insertion device. This sampling technique is based on the principle that the temperature gradient between soot particles entrained in the hot gas and the relatively cold surface of grid causes a thermophoretic drift of soot particles towards the cold grid, finally resulting in deposition. Furthermore, the grid provides a cold surface to freeze the reactions of the soot particles. Exposure time in the flame or reactor must be short so that the temperature of the grid is not raised significantly, yet long enough for deposition to occur. The chemical freezing action prevents changes in the soot morphology.

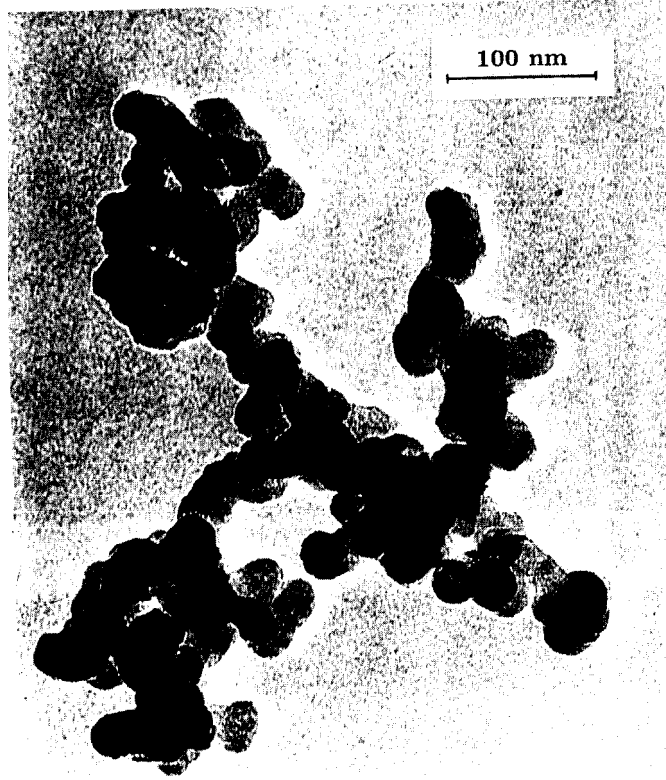


Figure 2.6. TEM micrograph showing soot from an ethene flame (from Dobbins and Megaridis, 1987).

Chapter 3

EXPERIMENTAL APPARATUS AND PROCEDURES

Overview

Coal pyrolysis experiments were conducted in a flat-flame laminar flow reactor running at atmospheric pressure. Coal particles were fed into the post-flame zone of the reactor. The post-flame gases, which contain mainly CO₂, H₂O, CO and unburned CH₄, simulate the gas-phase environment a coal particle sees when it travels through the near burner region of an industrial pulverized coal-fired furnace. As would occur in a real furnace, coal particles are heated up by the post-flame gases and undergo primary and secondary pyrolysis. Even though a flat flame can be operated over a wide range of equivalence ratios, all the experiments for this research were conducted in fuel rich conditions (equivalence ratio $\phi > 1$). The concentration of O₂ in the post-flame zone was negligible, based on both a combustion simulation and a measurement using an oxygen analyzer (Universal Enterprises, Inc., Model C100). The oxygen-free environment ensures no direct oxidation of tar and soot by oxygen molecules, although gasification by other oxygen-containing species may be possible.

The soot particles were collected using two different sampling methods: thermophoretic sampling and bulk collection. In bulk collection, the soot and char particles flowed into a water-cooled, nitrogen-quenched suction probe. In the process of collection, small soot particles ($< 5 \mu\text{m}$) were separated aerodynamically from char particles and large soot agglomerates by a combination of a virtual impactor and a cyclone, and then collected on two soot filters. In certain conditions (i.e., high temperatures and high residence times), the soot agglomerates were so large that they

were collected with the char particles at the end of the cyclone. These large soot agglomerates were separated from char particles using a sieve with 38 μm openings. The sizes and shapes of soot particles were examined using Transmission Electron Microscopy (TEM) and Scanning Electron Microscopy (SEM). Inductively-coupled plasma (ICP) analysis was performed on each sieved char sample and its parent coal to determine the extent of mass release due to coal pyrolysis. Elemental analysis was also performed on both char and soot samples to obtain the mass fractions of C, H and N in each sample. Variations of the testing conditions included the post-flame gas temperature, residence time, and coal type.

Flat-Flame Flow Reactor

A schematic of the flat-flame flow reactor system is shown in Fig. 3.1. It consists of a Hencken flat flame burner, similar to that used by McLean, et al. (1981), and two designs of towers used to confine the post flame gases. A round Pyrex tower was used for thermophoretic sampling, whereas a square quartz tower was used for bulk soot collection. The outlet of the burner has a dimension of 51 mm by 51 mm square. A mixture of methane, hydrogen and nitrogen was used as the fuel, and air was the oxidizer for combustion. There are about 750 capillary tubes evenly distributed inside the burner. The fuel passes through the inside of these capillary tubes, while the oxidizer flows through the honeycomb on the outside of the capillary tubes. The glass beads packed inside of the burner assure even distribution of oxidizer at the burner surface. Upon ignition, about 750 diffusion blue flamelets are formed on the burner surface. These flamelets are located 2 mm above the burner surface. The flow rates of methane, hydrogen, nitrogen and air were adjusted to obtain a stable, horizontally uniform flame and the desired post-flame gas temperature profile. The flame was fired upwards. The average velocity of the hot gas above the burner was approximately 2.3 m/s (i.e., laminar

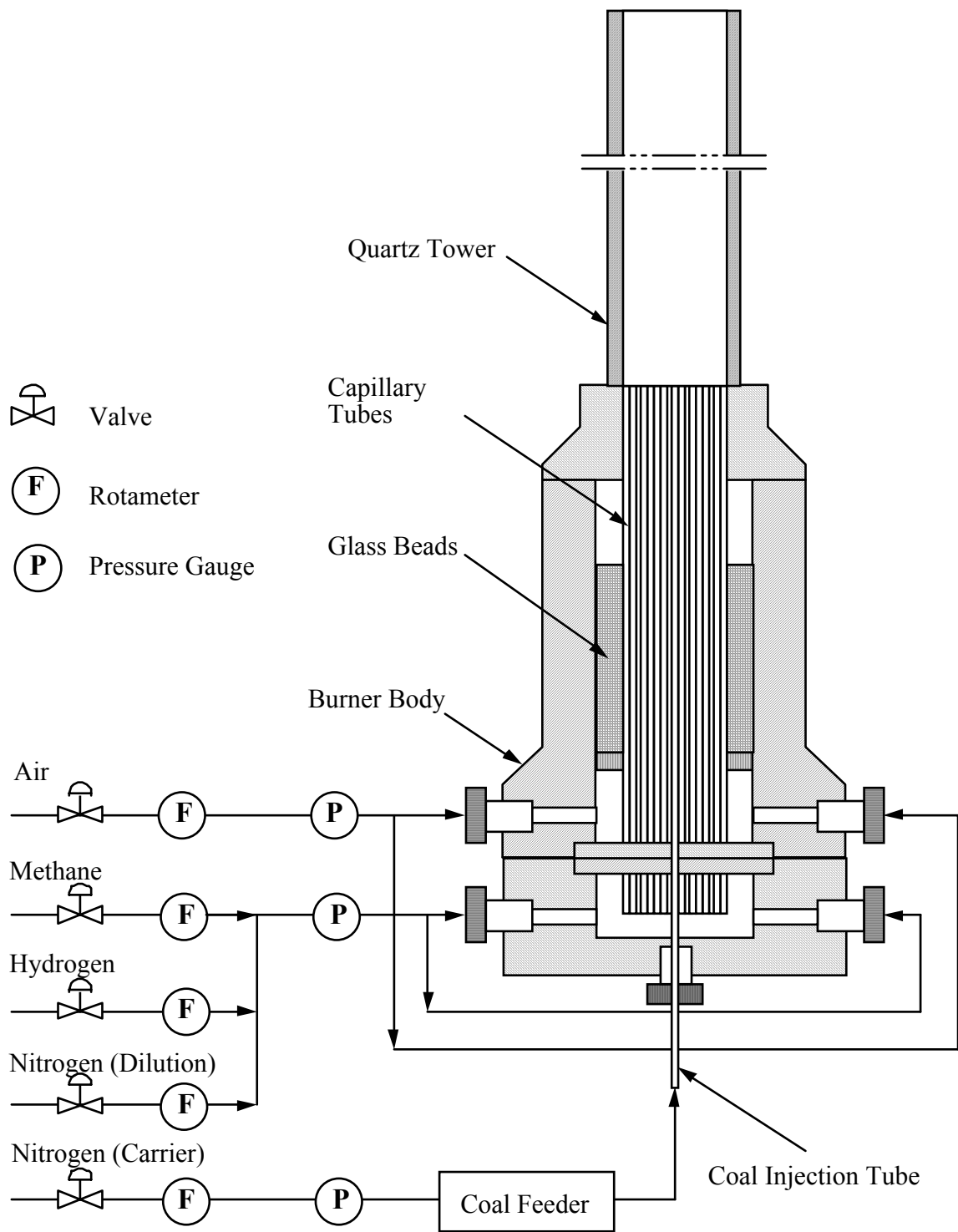


Figure 3.1. Schematic of the flat flame burner and gas delivery system.

flow) when the quartz tower was used. This velocity and other flame parameters were calculated using the modified Chemkin/Premix code, obtained from the Sandia National Laboratories (Kee, et al., 1985). However, due to the velocity distribution in a cross section of the tower, the actual centerline velocity was higher than the average velocity, and was around 2.9 m/s according to the char particle velocity measurements with a fast video camera and terminal particle velocity estimation. Coal particles were fed into the burner by a syringe particle feeder (described later). The hot combustion products from the methane/hydrogen/air flame entrained and heated the coal particles, which were injected at 2 mm above the burner surface on the centerline of the laminar flow reactor. Coal volatiles were released during particle heatup and then traveled radially away from the particles. While the char particles remained in a very thin stream (~1 mm in diameter) along the centerline of the tower, the volatiles cloud expanded to a diameter of approximately 3 cm. In Fig. 3.2, the bright centerline is the char particle trajectory and the envelope is the soot cloud. The whole burner and tower assembly is movable in 3 directions (x,y,z), which allows the changes of sampling height and radial position.

Three temperature conditions were used for the experiments. The corresponding flow rates of methane, hydrogen, air, dilution nitrogen and carrier nitrogen are listed in Table 3.1, along with the equivalence ratio. At these equivalence ratios, the formation of soot from methane/hydrogen combustion is negligible; the post flame gases are not luminescent. The post-flame gas temperatures were measured in the absence of particles using a fine-wire silica-coated type B thermocouple as a function of height z above the flat flame. The thermocouple readings were corrected for radiative heat loss (see Appendix G). Figure 3.3 shows the centerline gas temperature profiles in the quartz tower at the three flow settings listed in Table 3.1. As can be seen in the figure, the temperatures are slightly lower near the flat flame because of the injection of cold nitrogen gas used to carry the coal particles. From 2 cm to 7 cm above the flame surface, a maximum temperature is achieved and the axial profile is relatively flat. After 7 cm,

the temperature decreases with height z due to (a) convective heat loss to the surrounding wall and (b) radiative heat loss. For the sake of convenience, the three different gas conditions will be referred to using only the peak gas temperature. The three peak temperatures are approximately 1900 K, 1800 K and 1650 K. The measured centerline gas temperature profile for the round Pyrex tower is shown in Fig. 3.4; this is the only flow condition used to perform the thermophoretic soot sampling. The horizontal (“radial”) temperature profiles at different heights of the quartz tower are presented in Fig. 3.5. Figure 3.5 only shows the distributions at the 1900 K condition. The trends of temperature distributions at the other two flow settings are similar to what is shown in Fig. 3.5. Radial temperature distributions in the Pyrex tower are shown in Fig. 3.6. From Figs. 3.5 and 3.6, it can be seen that the temperatures are almost uniform within 1.5 cm of the centerline. Temperatures drop only in the boundary layer very close to the tower

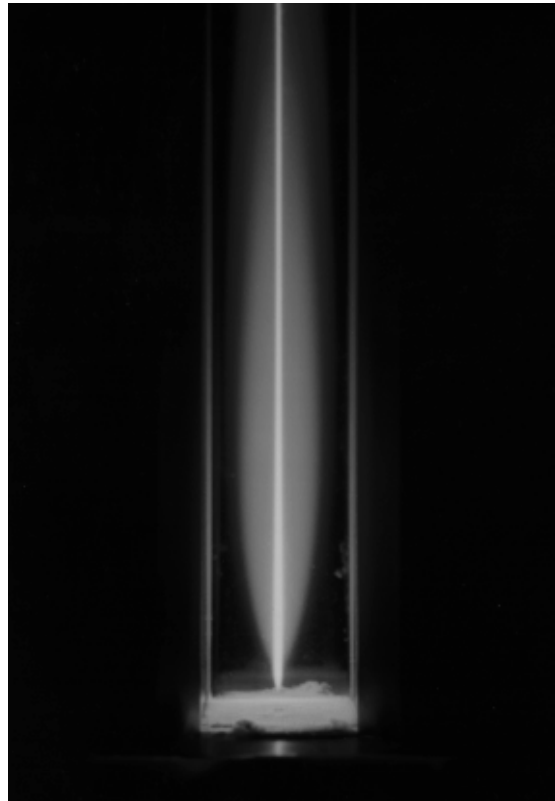


Figure 3.2. A photograph of the visible soot cloud.

Table 3.1. Flow rates in three temperature settings.

Temperature (K) ^a	CH ₄ (slpm) ^b	H ₂ (slpm)	Air (slpm)	Equivalence Ratio	Dilution N ₂ (slpm)	Carrier N ₂ (sccmpm) ^c
1900	5.64	0	42.70	1.26	0	39.7
1800	5.47	0	40.18	1.30	1.95	39.7
1650	5.12	2.91	37.74	1.48	5.24	39.7

^a Temperatures listed here refer to the highest temperatures inside the reactor.

^b “slpm” stands for standard liters per minute (i.e., at 1 atm, 298 K)

^c “sccmpm” stands for standard cubic centimeters per minute (i.e., at 1 atm, 298 K)

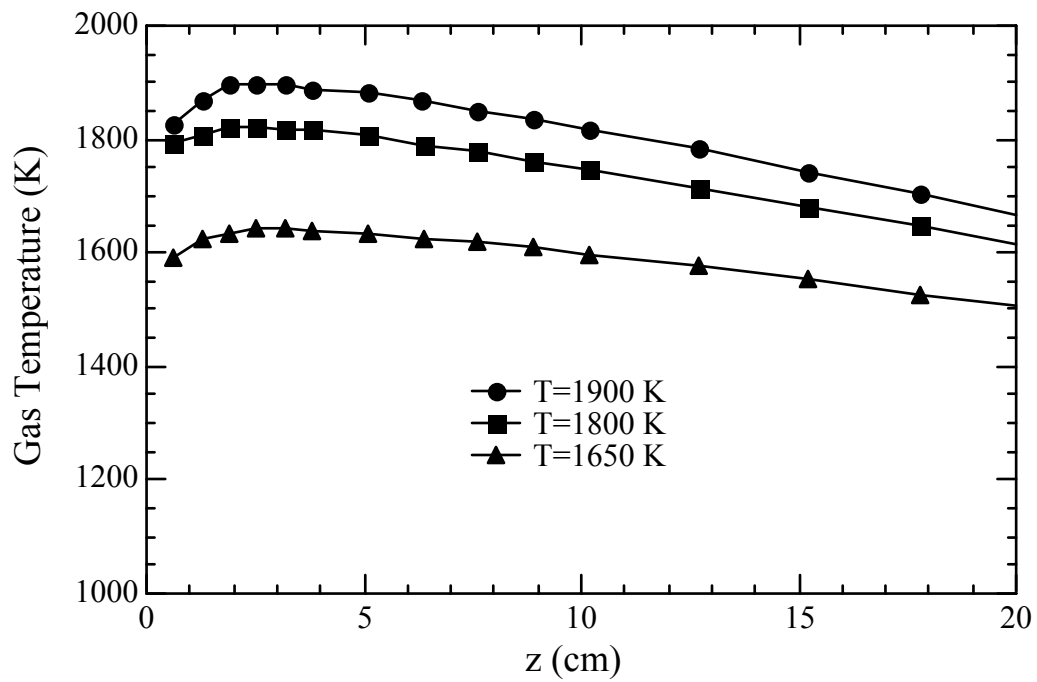


Figure 3.3. Centerline gas temperature profiles in the quartz tower.

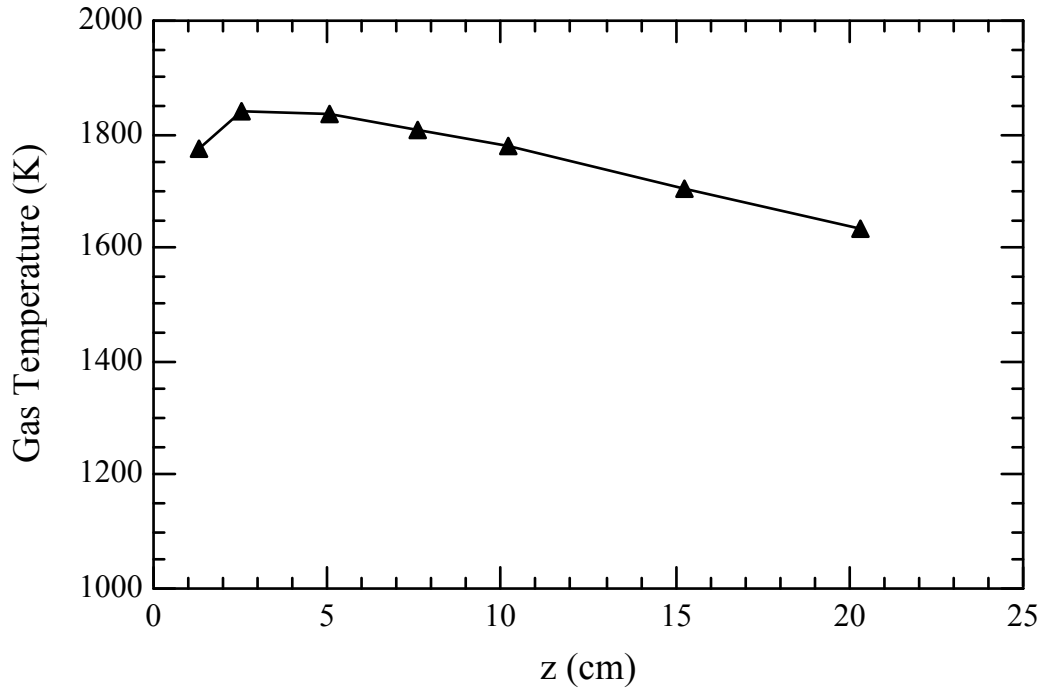


Figure 3.4. Centerline gas temperature profile in the Pyrex tower.

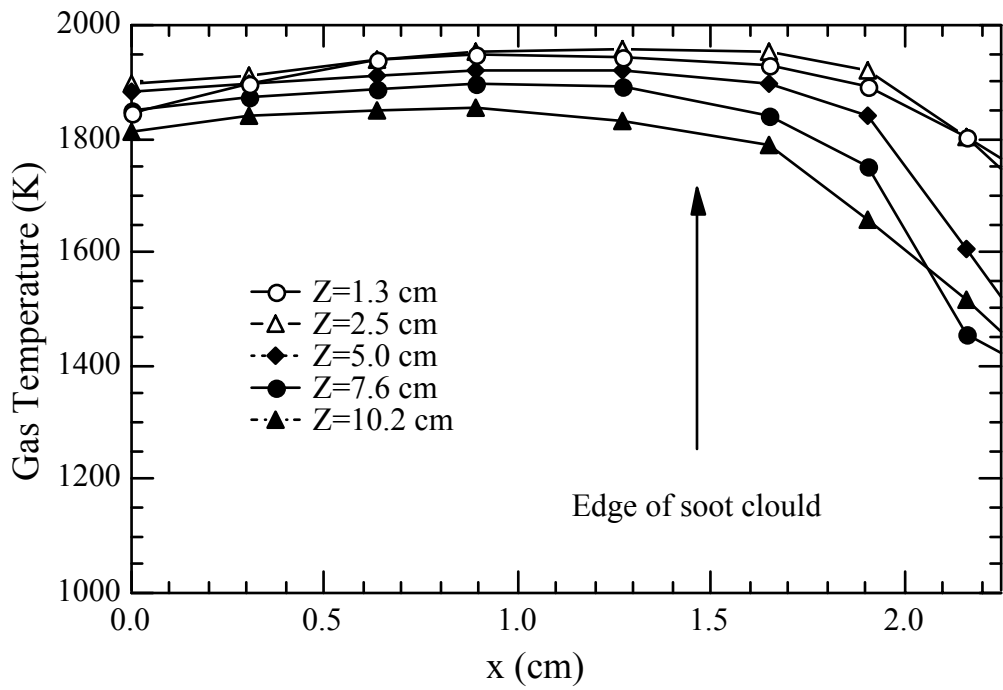


Figure 3.5. Horizontal gas temperature profiles at different heights of the quartz tower.

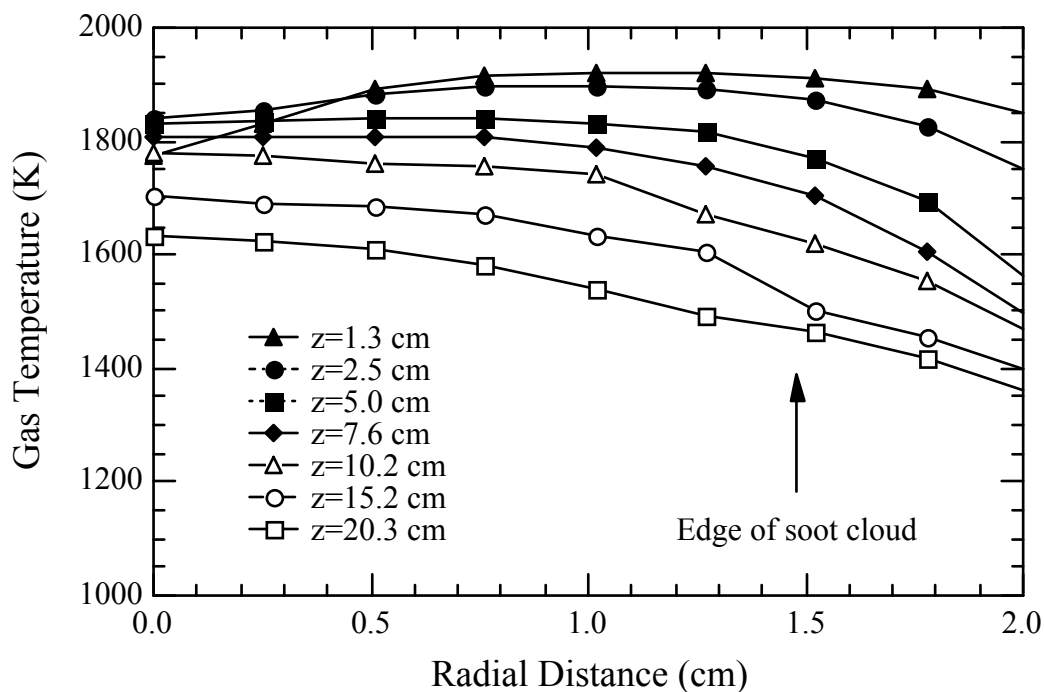


Figure 3.6. Radial temperature profiles at different heights of the Pyrex tower.

wall. As mentioned above, the radius of the visible soot cloud is around 1.5 cm. Therefore, for the soot chemistry experiments performed here, uneven radial temperature distributions are not considered to be a problem.

Coal Particle Feeder

A coal particle feeder was designed to provide a steady and variable feed rate and to allow an accurate measurement of the amount of coal fed in a run. The quality of a feeder affects the accuracy and reproducibility of the experimental results. The design for this feeder was patterned after the feeder used by Fletcher (1989).

Figure 3.7 is a schematic of the particle feeder. It consists of a Gastight[®] syringe, a modified glass funnel, a syringe pump, a step motor and a small vibrator. The needle

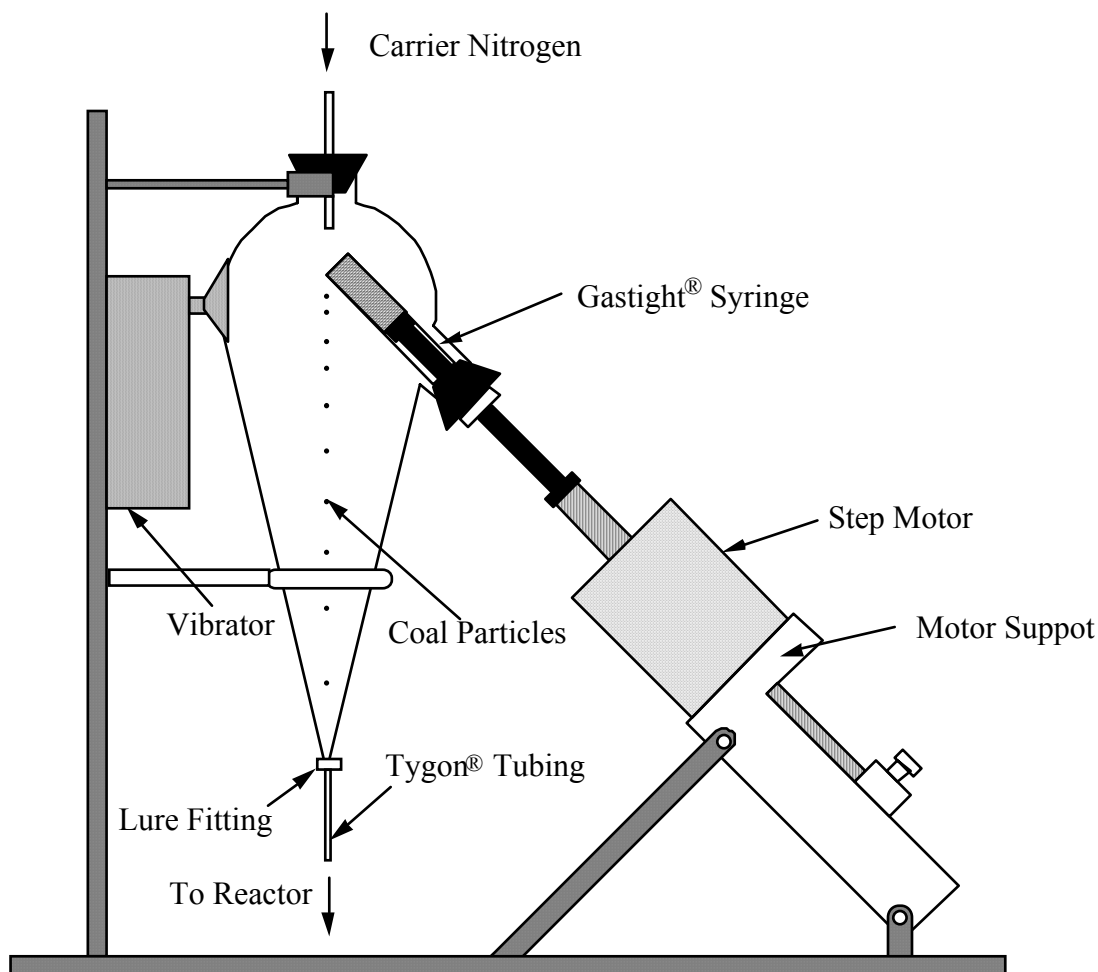


Figure 3.7. Schematic of the coal particle feeder.

fitting at the end of original syringe was cut off, leaving a cylindrical opening as shown in Fig. 3.7. About 2 grams of coal particles can be contained in the 2.5 ml syringe. The syringe is connected to the funnel through a rubber stopper. Particles are pushed out of the syringe to the funnel by the syringe pump which is driven by the step motor. The pulse signals used for driving the step motor are generated by a microcomputer. The particle feed rate can be adjusted by changing the frequency or period of the pulse signal (i.e., the stepping rate of the motor). A pulse generation code was written in C++ with an embedded assembly routine (see Appendix B for the code). The code reads in the square wave period (in milliseconds) as an input parameter and sends wave signals to the

computer's parallel port (LPT1), which is connected to the controller of the step motor. The exact frequency generated by the computer ensures the accuracy of the feed rate. The electrical vibrator attached to the funnel is used to shake the syringe/funnel assembly, and to make sure that the particles drop down from the syringe tip and reach the bottom of the funnel. Finally, the coal particles are entrained by a stream of carrier nitrogen gas into a plastic Tygon[®] tube with an inside diameter of 1 mm. The plastic tube is connected to the stainless steel injection tube installed inside the burner.

The amount of coal fed in one run was measured by weighing the coal contained in the syringe before and after the run. The difference was the weight of coal fed to the reactor. The balance used for weighing was a Mettler Model AB104, with a readability of 0.1 milligram and a precision of 0.2 milligram. The feed rate can be calculated based on the stepping rate and the bulk density of each coal. Also, the feed rate can be calibrated by recording the amount of coal fed during a certain period of time. The stepping rate for all the experiments in this research was set at 2 steps per second, which corresponded to a particle feed rate of approximately 1.5 g/hour. At this feed rate, the overlapping of two or more particles in the reactor after the injection was negligible, as visualized by the records of a fast video camera (see Fig. 4.1).

Thermophoretic Sampling

The size, shape, and state of agglomeration of coal-derived soot were examined using a technique called thermophoretic sampling, originally used by Dobbins and Megaridis (1987). As discussed in Chapter 2, this method provides a way to extract soot particles directly from a reactor or a flame without destroying the soot morphology. It has been shown that even though soot particles usually present a size distribution, the thermophoretic transport of soot particles is size- and structure-insensitive for soot generated from hydrocarbon flames (Rosner, et al., 1991). This insensitivity to size occurs only when all of the soot agglomerates are small and when the primary particles in

each agglomerate are not tightly packed, as is usually the case in simple hydrocarbon flames. However, as will be discussed later, soot agglomerates derived from coal can be much larger than those from the conventional hydrocarbon flames, especially at longer residence times and high temperatures. Therefore, the soot samples extracted through thermophoretic sampling in this research only represented the small soot particles and agglomerates.

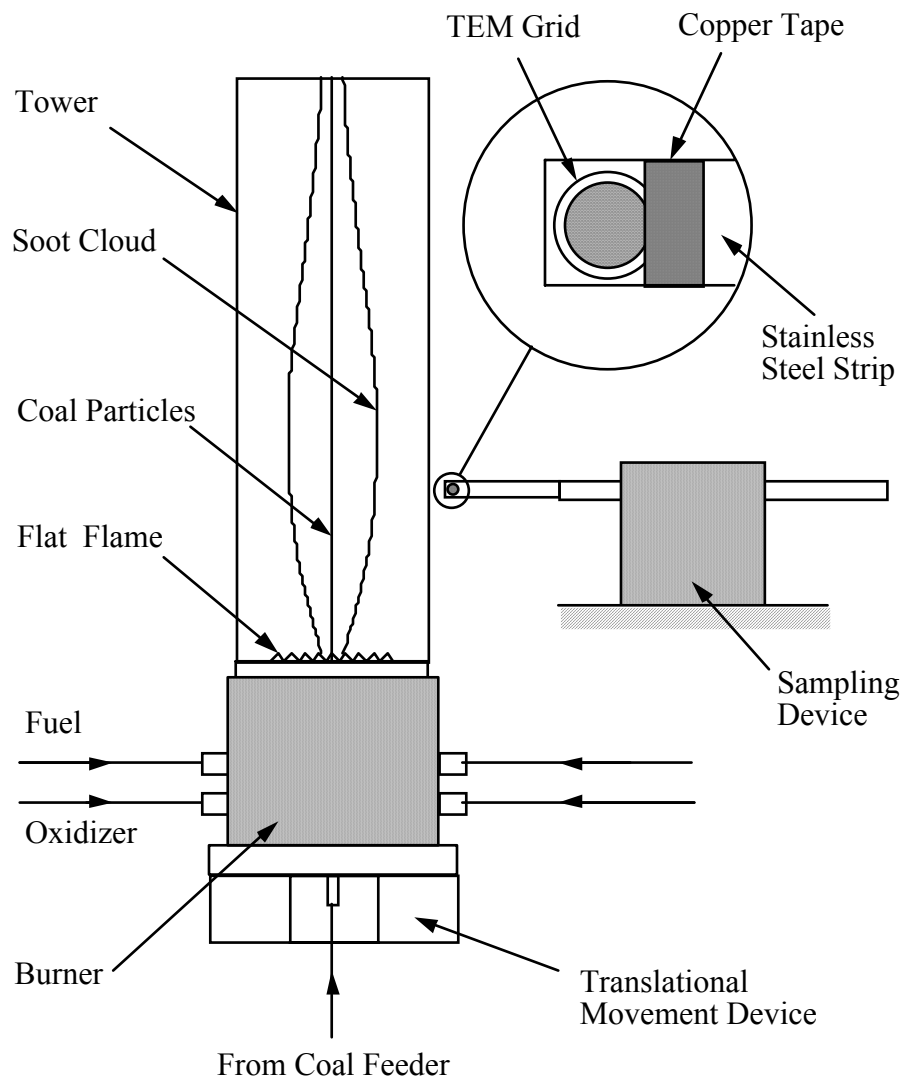


Figure 3.8. Schematic of the flat-flame flow reactor and thermophoretic sampling system.

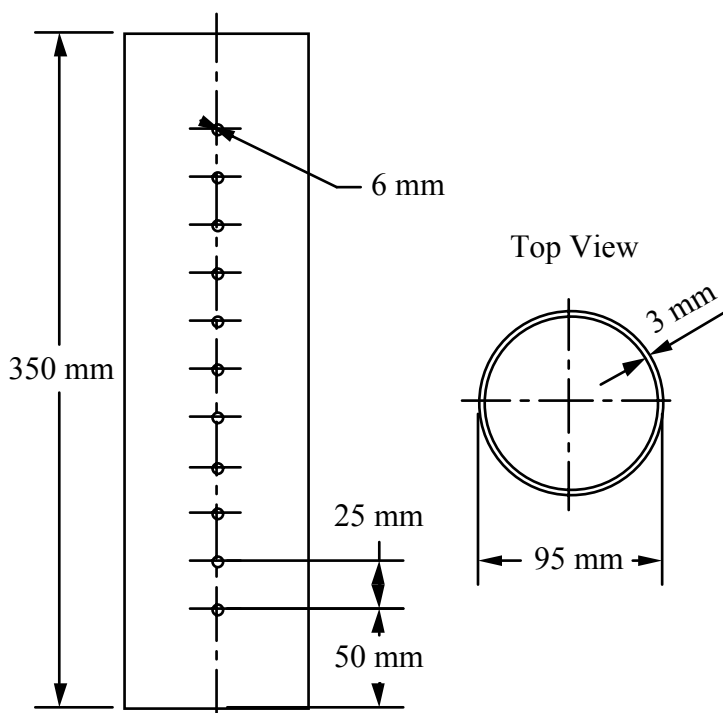


Figure 3.9. Schematic of the Pyrex tower for thermophoretic sampling.

Figure 3.8 shows a schematic of the thermophoretic sampling system in the flat flame reactor. A schematic of the cylindrical Pyrex tower for the thermophoretic sampling is shown in Fig. 3.9. Several sampling ports of 6 mm in diameter were constructed along the height of the Pyrex tower. Only one port was open at a time, allowing the sampling probe to be inserted horizontally into the soot cloud during the experiment. The rest of the ports were covered by a stainless steel sheet to avoid excessive disturbance of the gas flow in the reactor. For the best performance (i.e., minimal flow disturbance), even the circular sampling port was partially covered by the stainless steel sheet with a 2×6 mm slit opening, allowing a minimum amount of air to enter the tower.

Standard carbon-coated TEM grids were used for the thermophoretic sampling experiments. A good grid should have an intact shape, an intact carbon coating, and minimal contamination. Before each sampling experiment, every grid was first examined

under a conventional optical microscope to make sure that the grid was intact. The protective layer on the carbon coating of an intact grid was then removed using chloroform and acetone. The blank grid was then examined under the electron microscope after the removal of the protective layer to ensure that the carbon coating was intact and that there was minimal contamination. Although minor amount of contamination was sometimes observed on the grid, the shape of contaminant particles was discernible and usually lacked a distinct form. The grid was then attached with copper tape onto a stainless steel strip with dimensions 5 mm wide, 70 mm long and only 0.25 mm thick. The small thickness of the probe resulted in negligible disturbance of the gas flow. Sampling consisted of quickly inserting the TEM grid into the reactor and removing it from the reactor. The insertion device was spring-loaded and manually operated to provide residence times of approximately 0.1 second in the hot gases, as measured by a fast video camera. Low residence times are necessary to prevent the carbon coating on the grid from being destroyed. After sampling, the grid was removed from the probe and examined on a Philips 400 transmission electron microscope. The soot particles were usually observed under magnifications from 54,000 to 152,000. Results of the thermophoretic sampling experiments were recently published (Ma, et al., 1995a).

Bulk Collection and Soot/Char Separation

Bulk collection of soot allows quantitative measurement of soot yield in terms of weight percentage of dry ash-free coal fed to the reactor. By collecting the soot and char at different residence times (i.e., collection locations) and in different gas temperature conditions, information regarding soot formation, particle agglomeration and elemental composition can be obtained. A good collection system requires (a) rapid quenching of reacting gas, soot, and char particles, (b) a minimum loss of the materials during the

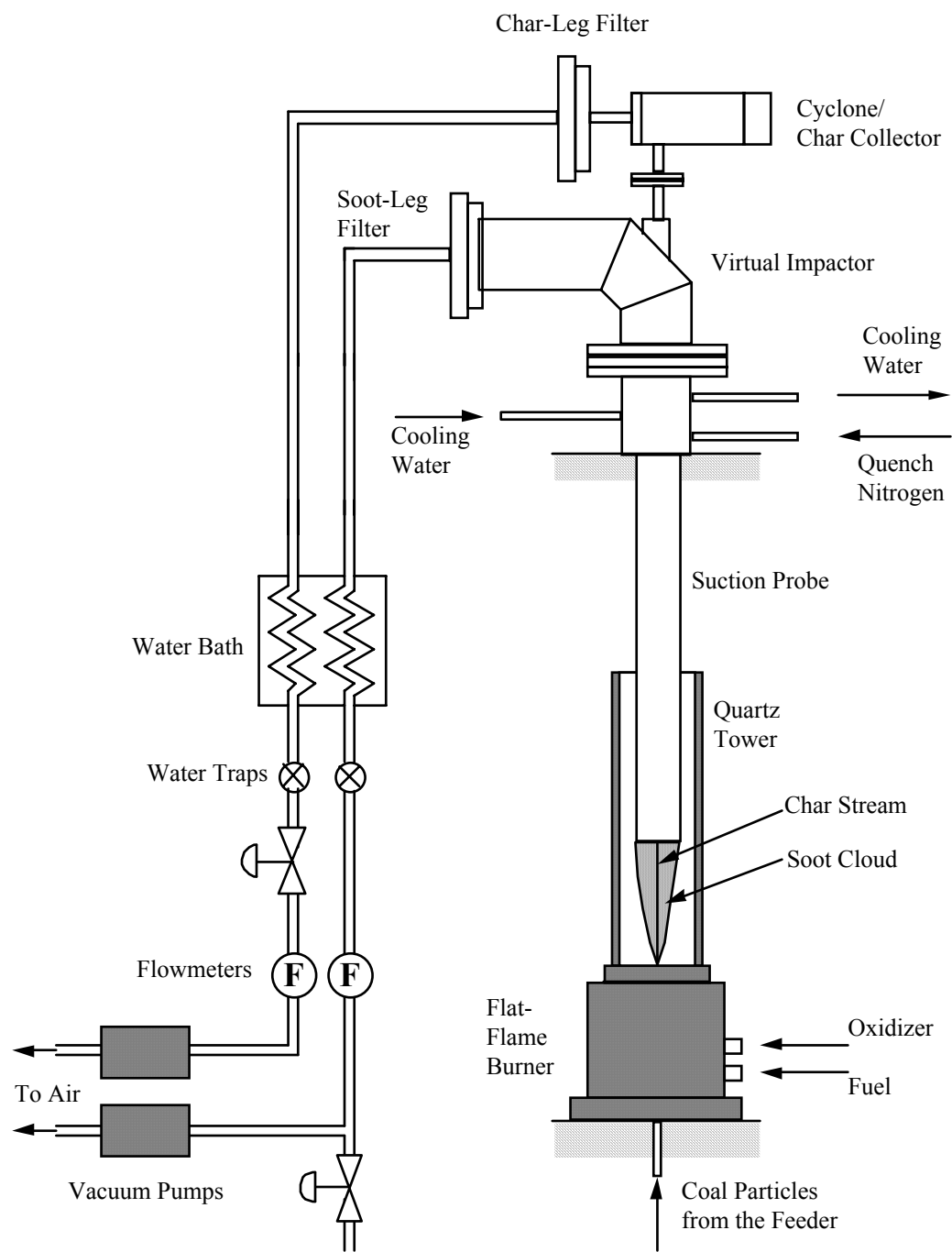


Figure 3.10. Particle collection and separation system.

collection, (c) good separation of soot from char, and (d) convenience for post-collection sample handling. Figure 3.10 shows a schematic of the collection and separation system designed as part of this work. The bulk soot collection system consists of a suction probe, a virtual impactor, a cyclone, two soot filters, a water condenser, two water traps and three vacuum pumps. These components are described below.

Suction Probe

The suction probe was patterned after a probe used at Sandia National Labs (Fletcher, 1989). This probe is capable of collecting soot, char, and gases, with negligible material loss. The probe has an inside diameter of 25.5 mm, an outside diameter of 44.5 mm, and a length of 61 cm. A schematic of the suction probe is shown in Fig. 3.11. The probe is nitrogen-quenched and water-cooled. The probe liner consists of a porous sampling tube made of sintered stainless steel with a pore size of 5 μm . About 30% of the quench nitrogen is injected through 12 jets in the mouth of the probe. The balance of the quench nitrogen (70%) transpires through the wall of the sintered tube to minimize any deposition on the inside wall of the probe. Two layers of water jackets are located outside of the transpiring tube (one for water in and the other for water out). The flow rate of cooling water is adjusted to avoid excessive condensation of water outside the suction probe, which causes the dripping down of water droplet onto the burner surface. The nitrogen quenching and the water cooling can keep the gas temperature inside the probe mouth below 700 K, as has been measured by a thermocouple, and freeze the secondary reactions. As mentioned in the previous section, the volatile cloud is observed to be about 3 cm in diameter, which is slightly larger than the inside diameter of the probe. However, pressure inside the probe was maintained at a level slightly lower than the ambient pressure (i.e., a slight vacuum) so that all visible materials were collected by the probe. There was no evidence of soot deposition on the exterior of the probe.

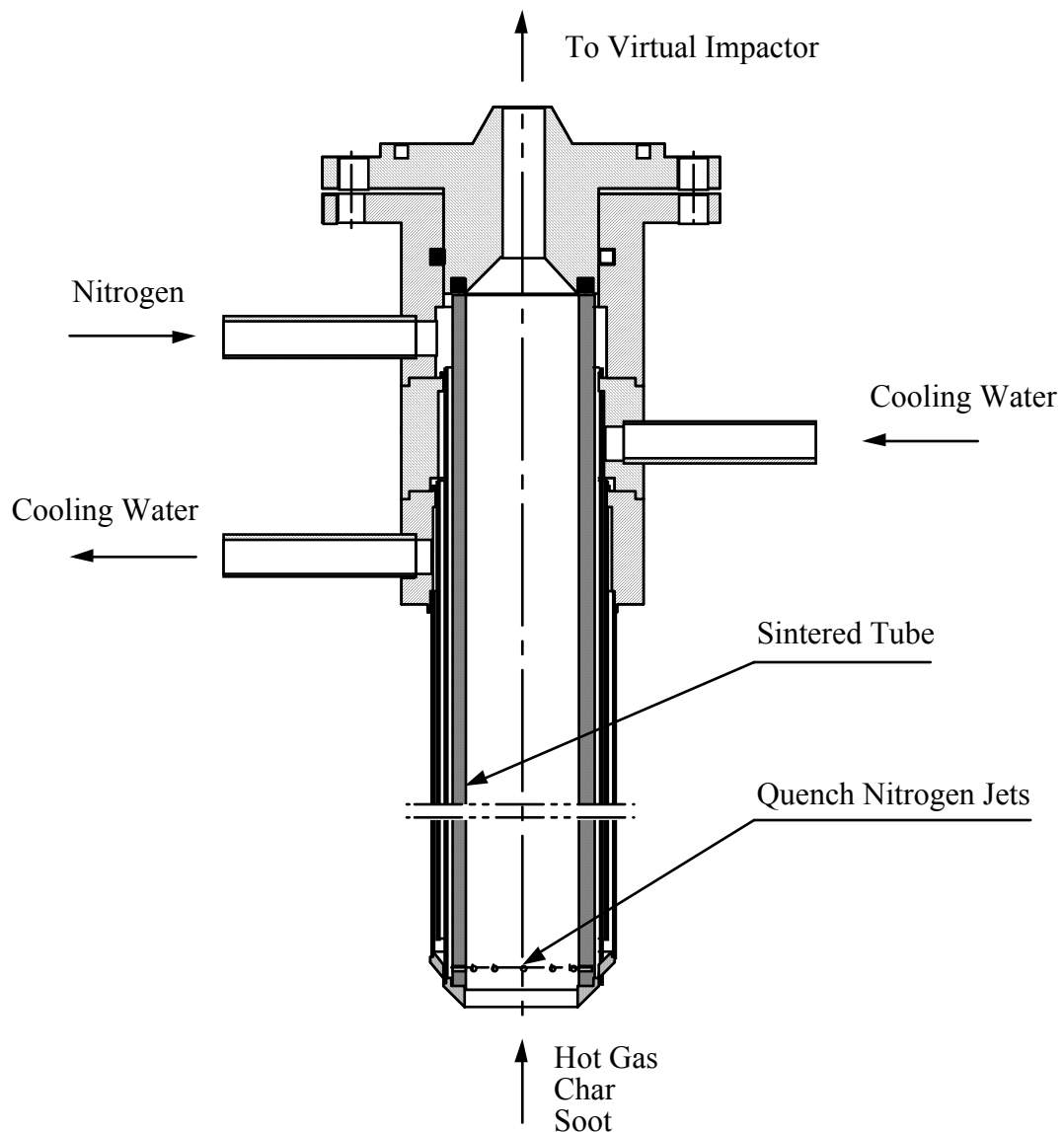


Figure 3.11. Schematic of the suction probe.

Virtual Impactor

A virtual impactor similar to that used by Daines (1990) and Monsen (1992) was designed for the separation of small soot particles from char particles and large soot agglomerates (see Fig. 3.12). The principle of this aerodynamic separator is based on the inertia difference between large and small particles. To use a virtual impactor, a stream

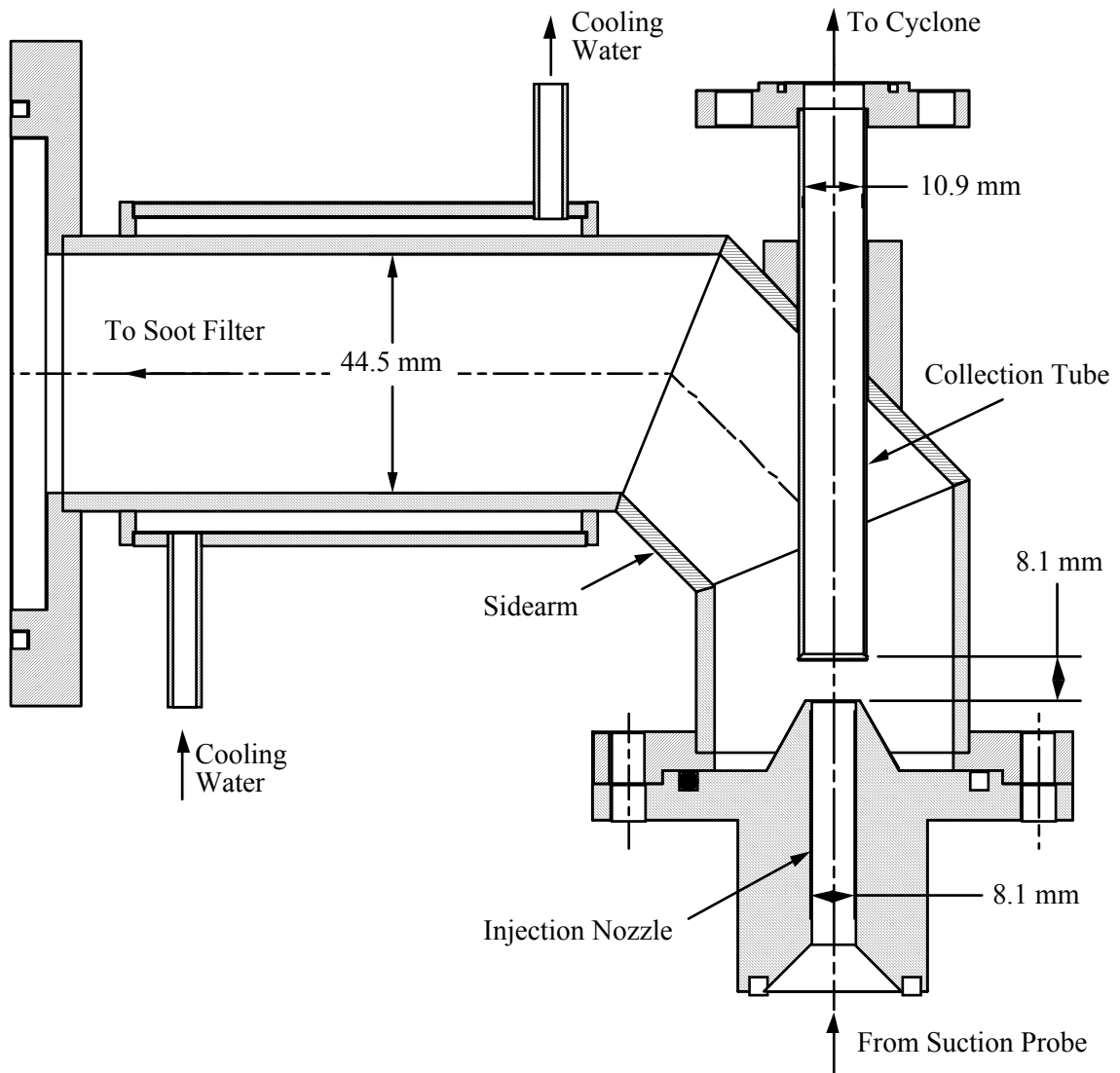


Figure 3.12. Schematic of the virtual impactor.

of particle-laden gases is introduced through an injection nozzle towards a reception tube. The reception tube diameter is slightly larger than the injection nozzle diameter. The gap between the injection nozzle and the reception tube has a dimension about the size of the injection nozzle. After passing through the injection nozzle, most of the gas stream abruptly changes directions and flows through the gas into the impactor sidearm, while the small remainder of the stream flows through the reception tube. The percentage of the gases exiting from the sidearm is usually between 75 and 95 %. Most of the very

small particles are entrained by the gases moving towards the sidearm due to the drag force, while all large particles, if the virtual impactor is designed correctly, end up in the reception tube, due to their higher inertia. Because gases flow through the reception tube, a small percentage of small particles may still be carried into the reception tube, which is usually separated later by some other device. A critical parameter governing the performance of a virtual impactor is the Stokes Number Stk , which is basically the ratio of inertial forces to drag forces. An ideal impactor would have a very steep slope on the efficiency curve centered around the desired 50% cut point (i.e., the particle diameter at which 50% of particles of that size can be collected).

Appendix C lists the guidelines for impactor design and also gives the detailed calculations about how the dimensions of the virtual impactor used in this research were determined. The geometry of a virtual impactor is usually determined by the gas flow rate, the operating temperature, and the desired cut point diameter. A cut point of $5\ \mu\text{m}$ was used in this application. In the process of design, two injection nozzles were tried and tested. The final design is shown in Fig. 3.12.

Cyclone

The virtual impactor does not completely separate small soot particles from char particles because a small amount of soot aerosol follows the gas flow to the reception tube of the virtual impactor. Further separation is usually required. Other investigators accomplished this secondary separation by using either a multi-stage plate impactor (Nenniger, 1986), a screen basket (Chen, 1991) or a cyclone (Fletcher, 1989; Daines, 1990). The first two methods require that the flow is downward, otherwise, the char particle can not stay on the impactor plates or basket due to gravity. In the case of a cyclone, the vortex generated by the tangential gas injection can push large particles towards the collection end of the cyclone even if the cyclone is held horizontally.

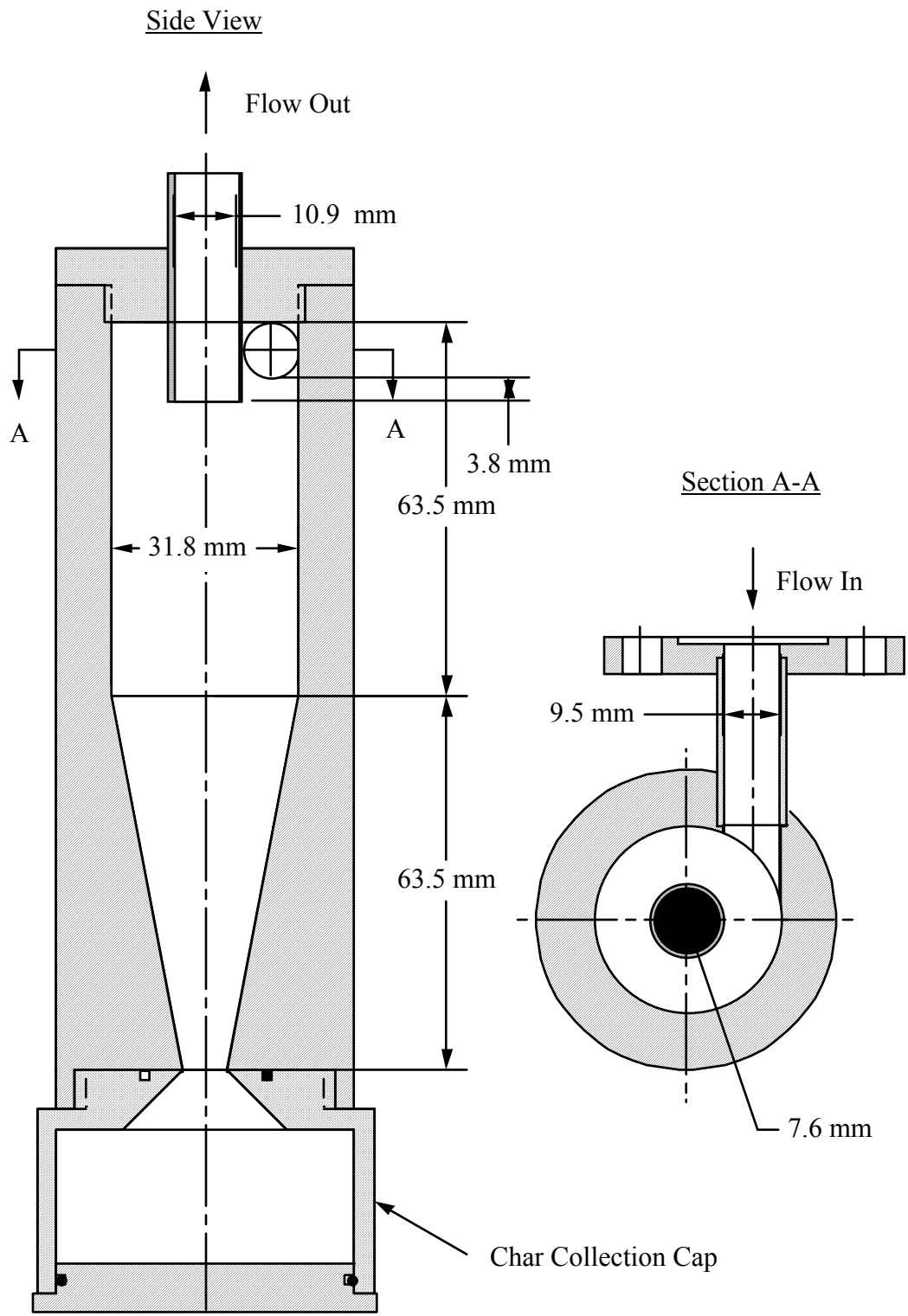


Figure 3.13. Schematic of the cyclone and the char collection cap.

Because of the upward flow configuration in this study, a cyclone was used for the final separation. The inlet of the cyclone was directly connected to the reception tube of the virtual impactor, with the body of the cyclone being held horizontally.

A schematic showing the design of the cyclone is shown in Fig. 3.13. The detailed design calculations are given in Appendix D. As in the design of the virtual impactor, the dimensions of a cyclone depend on the flow rate, operating condition and cut point diameter. In this design, a cut point of 5 μm was adopted. A special cap with a hollow space inside was also designed to attach to the end of the cyclone to hold the char sample during a run. A char sample after a sampling experiment can be recovered simply by loosening the screw of the cap from the cyclone body.

Soot Filters

Most of soot aerosol was collected on a filter connected to the side arm of the virtual impactor (see Fig. 3.12), with the balance collected on a filter after the cyclone. In the following discussion, the former will be referred as the soot-leg filter and the latter as the char-leg filter. The size of the filter was 90 mm in diameter for both legs.

Both glass fiber filter and Nuclepore[®] polycarbonate filters were tried. The glass fiber filters exhibited a lower pressure drop than the polycarbonate filters, permitting longer running times before becoming clogged. However, it was hard to remove the soot particles from the surface of the glass fiber filter because the glass fiber was very fragile. The polycarbonate filter with a pore size of 1 μm showed much better performance in sample removability, although the pressure drop was a little bit higher. The polycarbonate filter is a thin film with a smooth surface and straight, uniform cylindrical pores made by irradiating a thin polycarbonate plastic sheet, in contact with uranium sheet, with slow neutrons. Static was a problem when weighing the polycarbonate filter until a static removing device (Static Master, Model 2U500, NRD, Inc.) was applied, which effectively neutralized the static with α -particles without touching the surface of

the filter. Even though some soot particles and agglomerates may be smaller than the pore size ($1\ \mu\text{m}$), the collection efficiency for those particles is still very high (Finlayson-Pitts and Pitts, 1986). The higher pressure drop was overcome by using a lower vacuum pressure after the filters.

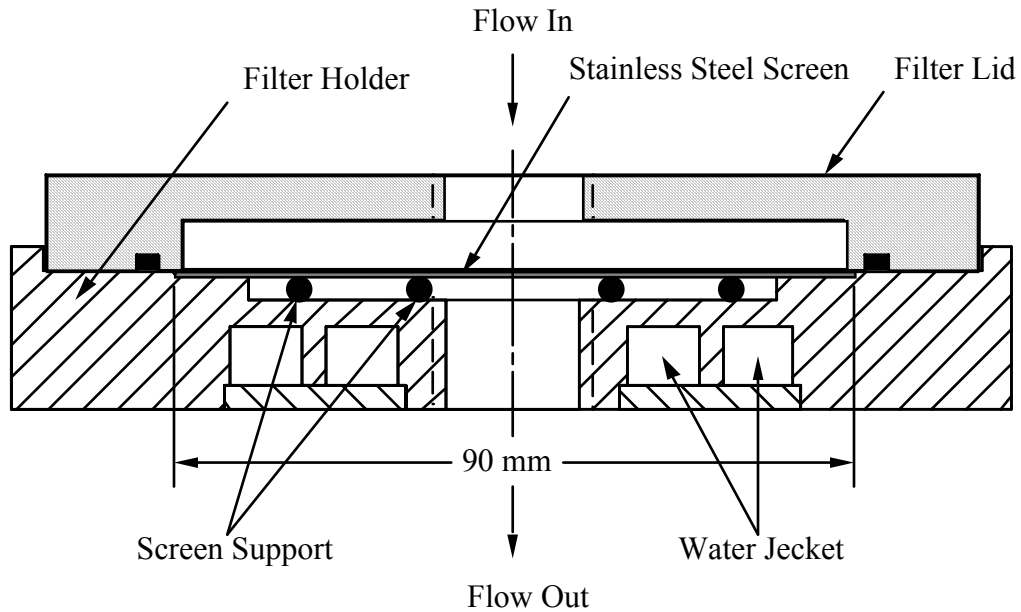


Figure 3.14. Schematic of the filter holder.

A schematic showing the design of the filter holder is shown in Fig. 3.14. The lid for the soot-leg filter holder was welded directly to the side arm of the virtual impactor (see Fig. 3.12), while the lid for the char-leg filter holder was connected to the cyclone outlet with a fitting. Both filters were held vertically due to restriction of lab space and flow configuration. This arrangement avoids the use of excess tubing and therefore minimizes soot deposition inside the tubes. A special stainless steel screen from Millipore, which has small perforated holes of about $0.5\ \text{mm}$ in diameter, was used to support each filter. A stainless steel support (made of $3\ \text{mm}$ diameter wire) was placed under the screen to avoid the deformation of the screen during sample collection. Because the opening area of the perforated holes in the screen was limited, a piece of

high-volume paper filter was sandwiched between the screen and the polycarbonate filter to reduce the pressure drop. Both the side arm of the virtual impactor and the filter holder for the soot-leg were water-cooled to avoid possible melting of the polycarbonate filter (see Fig. 3.12 and Fig. 3.14). Cooling of the char-leg filter holder was not necessary because the gas temperature there was low enough due to heat losses in the cyclone. Special care was taken when mounting the filters on each filter holder. Because the filter was held vertically, a small vacuum was kept down stream of the filter to keep the filter on the screen during mounting.

Water Condenser, Water Trap, Flow Meters and Vacuum Pumps

Burning of methane or hydrogen with oxygen generates steam. The temperature of the filter is adjusted so that the steam does not condense on the filters. However, normal operation of the vacuum pumps requires that the gas stream has a temperature less than 70 °C and contains no liquid. To meet this requirement, water was first condensed out by passing the two gas streams through two cooling coils which were immersed in a cold water bath (see Fig. 3.10). Two water traps, consisting of two glass flasks, were placed after the water condenser for both soot-leg and char-leg gas streams. The flow rates of the two water-free streams were controlled by regulating valves and measured by rotameters (along with vacuum gauges). Finally, the two streams were vented to the air by three Gast[®] rotary vane vacuum pumps, one for the char leg and two for the soot leg.

System Calibration and Testing

Bulk collection was initially performed when nothing was fed through the particle injection tube. No particle deposition was found on the soot filters, which verified the fact that no soot is formed in methane/hydrogen flat flame.

The separation efficiency of the bulk collection system was checked in different ways. First, an acetylene stream was fed through the “coal feed tube” into the post-flame zone of the methane/hydrogen/air flat flame. In this case, the solid particles formed were exclusively tiny soot particles. These particles were collected with the sampling probe to test the effectiveness of aerodynamic separation. In this test, no soot particles were found in the cyclone. This means that soot will not be collected in the cyclone if the soot particles are smaller than the acetylene soot. Second, coal particles were fed to an oxygen-rich methane/air flame. In this test, the soot yield should be negligible due to the oxidation of soot and its precursors, while residence times were low enough to permit only a small amount of char oxidation. In this test, all of the particles were collected in the cyclone, and almost no particles were collected on the two filters. This suggests that soot samples collected in coal pyrolysis tests will not be contaminated by char particles. Third, the soot samples collected on the two filters in the normal collection conditions were examined under SEM, and no single char particles were observed. Finally, the soot samples of coal pyrolysis tests were analyzed chemically. The samples consisted of C, H, and N, with no ash being found. This series of tests showed that small soot particles were separated from char particles, as designed.

While char particles do not enter the filters, coal-derived soot agglomerates may still be collected in the cyclone if they are larger than 5 μm . At high temperatures and high residence times, some coal-derived soot agglomerates reached sizes that exceeded the designed cut point. The presence of soot in the collected char samples was first recognized when (a) a dark black layer was observed in the collected char samples, and (b) a much higher bulk volume of char sample was obtained than the coal fed. Further examination of these char samples under SEM with X-ray elemental analysis showed that many small particles of 20 to 30 μm were mixed with the 70 μm diameter char particles. These smaller particles were brighter in SEM pictures than the char particles, due to their high surface roughness. Meanwhile, the X-ray spectrum showed that there were no

elements on the surface of these small particles except carbon. Based on these observations, it is clear that these small particles were extremely large coal-derived soot agglomerates. To separate these soot agglomerates from the char particles, a sieve with openings of 38 μm was used. Some mass of soot was lost during the sieving procedure, due to the low density of these soot agglomerates. Therefore, the amount of soot in an unsieved sample was calculated by the difference between the initial sample and the pure char obtained after sieving.

Different ratios of gas flow in the soot leg to that in the char leg were examined before taking the formal tests. The best performance was obtained with a flow ratio of 4 to 1, i.e., 80% of the inlet flow went through the side arm and 20% of the flow ran through the reception tube. The percentage of the gases through the reception tube was higher than what had been used by Nenniger (1986) and Chen (1991) but similar to that used by Fletcher (1989). One reason for the higher percentage might be partly due to the upward flow configuration. Also, the flow rate of the gas entering the cyclone must be high enough to create a strong vortex in the cyclone for separation of char particles. During a typical collection process, the gradual accumulation of soot particles on each filter will always cause an increase of pressure drop through the filter. Therefore, the openings of the two valves were adjusted manually to keep the mass flow rates and the gas split ratio constant. A good indication of a normal operation is that the orange soot cloud is slightly disturbed only near the collection probe, and that no particles bypass the collection probe. The flow rates in both soot and char legs as well as the flow rate of quench nitrogen are listed in Table 3.2.

Table 3.2. Gas flow rates used for particle bulk collection experiments.

Quench N ₂ (slpm) ^a	Soot-Leg (slpm)	Char-Leg (slpm)	Total (soot-leg + char-leg) (slpm)
69.18	69.83	17.20	87.03

^a “slpm” stands for standard liters per minute (i.e., at 1 atm, 298 K)

The deposition of soot aerosol on the walls of the collection system was also examined. No deposition was found on the inner side wall of the transpiring tube in the collection probe. Liners fabricated from thin brass sheets were placed inside the virtual impactor and cyclone. The amount of deposition on the sidearm wall and the cyclone wall was determined by weighing the liners before and after a coal pyrolysis test. It was found that about 10% of total soot sample was deposited on the liners. Thus, the amount of soot collected on the filters was increased by 10% in order to give an accurate soot yield. This correction for soot deposition is similar to the correction used by Chen (1991).

Particle Residence Time Measurement

Soot yields at different residence times give information of kinetics of soot formation. Chemical or physical properties of soot may also change with residence time. For the bulk collection and thermophoretic sampling, residence time was varied by changing the sampling location in the reactor. To obtain an accurate residence time of a coal particle at a certain height of the tower, a fast video camera (Kodak EktaPro Imager) was used to follow the trajectory of the coal particle. The recording speed of the camera was set at 500 frames a second. The video images were first stored in the memory device (Kodak EktaPro EM Processor) of the camera, which were transferred later to a video tape using a super-VHS VCR (JVC Model BR-S378U). The distance a particle moved versus time was finally obtained by playing back the video tape and measuring the distance the particle moved on a 20 inch TV screen. The image of each frame can also be transferred to a picture file and printed out by a laser printer. One limitation of the residence time measurement was that a char particle was visible only at certain height above the flat flame, i.e. after the particle was heated up to a high enough temperature.

The dark space between the coal injection point and the point at which a coal particle can be measured varied from 10 to 15 mm, depending on the temperature setting. All six coals used in this study were tested at three temperature settings using the square quartz tower.

Mass Release and ICP Analysis

Mass release of coal due to pyrolysis was determined in two ways. One was through directly weighing the mass of coal fed and the mass of char obtained in a collection experiment. In other words, this was a mass balance method. Samples were weighed using the Mettler balance described earlier. The mass balance method generally gives a high bound on the mass release, since some coal particles may be lost during the collection.

Another method that was used to check the mass release was to use Ti as a tracer in char and parent coal. The mass fractions of Ti in parent coal, char and ash were measured using an inductively coupled plasma (ICP) method according to ASTM Procedure D 3682. In this method, both parent coal and char samples were ashed and digested; the concentrations of certain elements in the solutions were measured using an ICP machine (Perkin Elmer) in the Chemistry Department of BYU. Assuming no Ti loss in the pyrolysis and ashing processes, the mass fractions of Ti in parent dry coal (f_{Ti}^{coal}), in dry char (f_{Ti}^{char}) and in ash (f_{Ti}^{ash}) are related to the masses of the coal (m_{coal}), char (m_{char}) and ash (m_{ash}) by:

$$m_{coal}f_{Ti}^{coal} = m_{char}f_{Ti}^{char} = m_{ash}f_{Ti}^{ash} \quad (3.1)$$

The percentage mass release or total volatile yield Y_{vol} (on dry ash free basis) during pyrolysis can then be calculated:

$$Y_{vol} = \frac{m_{coal} - m_{char}}{m_{coal} - m_{ash}} = \frac{m_{coal} - \frac{f_{Ti}^{coal}}{f_{Ti}^{char}} m_{coal}}{m_{coal} - \frac{f_{Ti}^{coal}}{f_{Ti}^{ash}} m_{coal}} = \left(\frac{f_{Ti}^{char} - f_{Ti}^{coal}}{f_{Ti}^{ash} - f_{Ti}^{coal}} \right) \left(\frac{f_{Ti}^{ash}}{f_{Ti}^{char}} \right) \quad (3.2)$$

The Ti tracer method usually gives a lower value of mass release if the tracer element vaporizes or leaves the char matrix during the coal pyrolysis. In this study, temperatures as high as 1900 K were used. At such high temperatures, Ti may leave the char particles (Baxter, 1995b), possibly causing lower values of the calculated mass release.

Elemental Analysis

Mass fractions of carbon, hydrogen, and nitrogen of parent coal, char, and soot were determined by a C-H-N analyzer (LECO 800). The analyzer was calibrated with several standard compounds with known compositions. A high-precision balance with 0.01 mg readability was used to determine sample mass. Some of the samples were analyzed in the ACERC Combustion Lab; the rest were analyzed at Western Analysis, Inc. in Salt Lake City. Several soot samples were also sent to LECO Corporation for independent testing. The results obtained by the LECO Corporation were very comparable to data obtained from the machine used in this study.

Chapter 4

EXPERIMENTAL RESULTS

Coal Types and Characterization

Coal rank is believed to be an important variable for tar yield and volatile composition. It must also affect the soot yield and soot properties. Six coals were used in the experiments, ranging in rank from lignite to medium volatile bituminous coals: Zap lignite (PSOC-1507D); Dietz subbituminous coal (PSOC-1488D); Utah Hiawatha high volatile B bituminous coal (PSOC-1502D); Pittsburgh #8 high volatile A bituminous coal (PSOC-1451D); Illinois #6 high volatile A bituminous coal (PSOC-1493D) and Pocahontas #3 medium volatile bituminous coal (PSOC-1508D). The "D" classification refers to a suite of coals selected for research by the DOE PETC's Direct Utilization/AR&TD program. These coals were originally obtained from Penn State, and were sieved and aerodynamically classified under nitrogen. A size cut of 63-75 μm was used in these experiments. The proximate and ultimate analyses for these coals are listed in Table 4.1.

Particle Residence Time Measurements

The distance a coal particle moves versus time can be measured using the fast video camera as described in Chapter 3. The video camera can only record particle trajectory after it becomes hot enough to be luminous (~ 1200 K). Accurate estimation of the total residence time requires the consideration of the residence time before the luminous point. The residence time correction was made by recording the distance from the point of coal injection to the point where a particle started to luminesce, and then

modeling the initial particle acceleration over this distance. The real residence time at a certain collection location was basically a summation of the calculated time before the luminous point and the time recorded after that point.

Table 4.1. Proximate and ultimate analyses for the six coals used in this study.

Coal Type	wt%	wt% (dry)		wt% (daf)				
	Moisture	Volatiles	Ash	C	H	N	S	O
PSOC 1507D Zap lignite	19.12	41.50	15.31	69.98	5.59	1.17	2.08	21.19
PSOC 1488D Dietz subbit.	19.59	40.06	4.55	75.39	5.57	0.87	0.45	17.71
PSOC 1493D Illinois #6 hva bit.	6.94	38.69	15.13	76.65	4.93	1.47	6.93	10.01
PSOC 1502 Utah Hiawatha hvb bit.	7.58	38.78	9.14	80.53	5.96	1.33	0.47	11.71
PSOC 1451D Pittsburgh #8 hva bit.	1.87	37.10	4.11	84.70	5.40	1.71	0.92	7.26
PSOC 1508D Pocahontas #3 lv bit.	0.97	15.91	11.65	90.51	4.59	1.60	0.77	2.52

The initial particle acceleration was modeled as follows. Assuming the coal particle is a sphere with a diameter D_p and density ρ_p , the drag force acting on the particle is

$$\begin{aligned}
 F_k &= \left(\frac{\pi D_p^2}{4} \right) \left(\frac{1}{2} \rho_g v_\infty^2 \right) \left(\frac{24}{\text{Re}} \right) \\
 &= \left(\frac{\pi D_p^2}{4} \right) \left(\frac{1}{2} \rho_g v_\infty^2 \right) \left(\frac{24 \mu_g}{D_p v_\infty \rho_g} \right) \\
 &= 3\pi \mu_g D_p v_\infty
 \end{aligned} \tag{4.1}$$

where μ_g , ρ_g , and v_∞ are gas viscosity, gas density, and slip velocity between the particle and entraining gas, respectively. The force of gravity on the particle is

$$F_g = \frac{\pi}{6} D_p^3 (\rho_p - \rho_g) g \quad (4.2)$$

The acceleration of the particle a can be expressed as:

$$\begin{aligned} a &= \frac{dv_p}{dt} = \frac{F_k - F_g}{\frac{\pi}{6} D_p^3 \rho_p} \\ &= \frac{3\pi\mu_g D_p v_\infty - \frac{\pi}{6} D_p^3 (\rho_p - \rho_g) g}{\frac{\pi}{6} D_p^3 \rho_p} \\ &= \frac{18\mu_g v_\infty}{D_p^2 \rho_p} - \left(1 - \frac{\rho_g}{\rho_p}\right) g \end{aligned} \quad (4.3)$$

Terminal velocity of a particle can be calculated by setting the acceleration a in Eq. 4.3 to zero. Therefore,

$$v_t = \frac{(\rho_p - \rho_g) g D_p^2}{18\mu_g} \quad (4.4)$$

Assuming a coal particle had a density of 1300 kg/m^3 , the terminal velocity of a $70 \text{ }\mu\text{m}$ particle was calculated to be 0.2 m/s at room temperature. The gas velocity at the tip of the coal injection tube was calculated to be 0.45 m/s , based on the flow rate of carrier nitrogen and the size of the injection tube. Therefore, the initial velocity of a coal particle was 0.25 m/s , which was used as the initial condition for the integration of Eq. 4.3. The slip velocity v_∞ is the difference between velocity of the hot gas v_g and particle velocity v_p :

$$v_\infty = v_g - v_p \quad (4.5)$$

The gas velocities along the height of the tower were estimated according to measured gas temperatures and results of the combustion simulation of the flat flame (to

be discussed in Chapter 5). The integration of Eq. 4.3 was performed on a spread sheet with a time step of 0.5 ms. The calculated data of distance versus residence time were fit using a third order polynomial expression:

$$z = a_1 t + a_2 t^2 + a_3 t^3 \quad (4.6)$$

This expression can be conveniently used for the kinetic modeling of the soot formation and agglomeration (discussed later). The coefficients for three temperature settings are listed in Table 4.2.

Table 4.2. Coefficients for curve-fits of particle residence time during the initial acceleration stage.

Temperature (K)	a_1 (s ⁻¹)	a_2 (s ⁻²)	a_3 (s ⁻³)	t_l (s) ^a	z_l (m) ^b
1900	0.2197	220.8	-7018.4	0.007	0.0100
1800	0.2192	216.3	-7057.7	0.008	0.0120
1650	0.1943	199.2	-6290.5	0.010	0.0156

^{a, b} t_l and z_l are the residence time and height at which a particle started to luminesce.

The distance between the particle injection point and the point that a particle started to luminesce was found to be dependent on temperature condition. In Table 4.2, z_l is the distance and t_l is the corresponding residence time that a particle started to luminesce. After the luminous point, the distance versus residence time was determined using the video camera measurements. Figure 4.1 shows a typical series of pictures in which the upward particle movement can be seen. The distance versus residence time when the particle was visible was also fit using a third order polynomial function, i.e.,

$$z = z_l + b_1(t - t_l) + b_2(t - t_l)^2 + b_3(t - t_l)^3 \quad (4.7)$$

The coefficients for all six coals and three temperatures are listed in Table 4.3. The analytical expressions of Eqs. 4.6 and 4.7 were used in the coal devolatilization and

soot formation simulations (as will be discussed in the next chapter). When $t \leq t_l$, Eq. 4.6 was used, and when $t > t_l$, Eq. 4.7 was used.

Table 4.3. Coefficients for curve-fits of particle residence time determined from high-speed video camera tests.

Coal Type	Temp (K)	b_1 (s^{-1})	b_2 (s^{-2})	b_3 (s^{-3})
Pittsburgh #8	1900	2.172	26.77	-265.2
	1800	2.044	30.65	-291.7
	1650	2.108	24.10	-224.7
Illinois #6	1900	2.045	30.65	-291.7
	1800	1.953	28.41	-273.8
	1650	2.113	16.76	-126.1
Utah Hiawatha	1900	2.208	25.97	-253.2
	1800	2.106	25.73	-251.7
	1650	2.316	9.02	-44.6
Pocahontas #3	1900	1.955	33.17	-338.3
	1800	2.077	23.42	-209.1
	1650	2.033	18.11	-135.0
Dietz	1900	2.154	12.64	-93.1
	1800	1.981	30.54	-292.2
	1650	2.198	12.68	-89.0
Zap	1900	2.375	17.69	-146.0
	1800	2.454	10.84	-56.7
	1650	2.186	12.51	-81.0

Figure 4.2 is a plot of particle height z versus residence time t for a Pittsburgh #8 coal particle entrained in the three temperature conditions, where both the modeled initial acceleration stage and video measurement results are shown. The corresponding particle velocities are accelerated from 0.25 m/s to approximately 2.8 m/s in 20 ms.

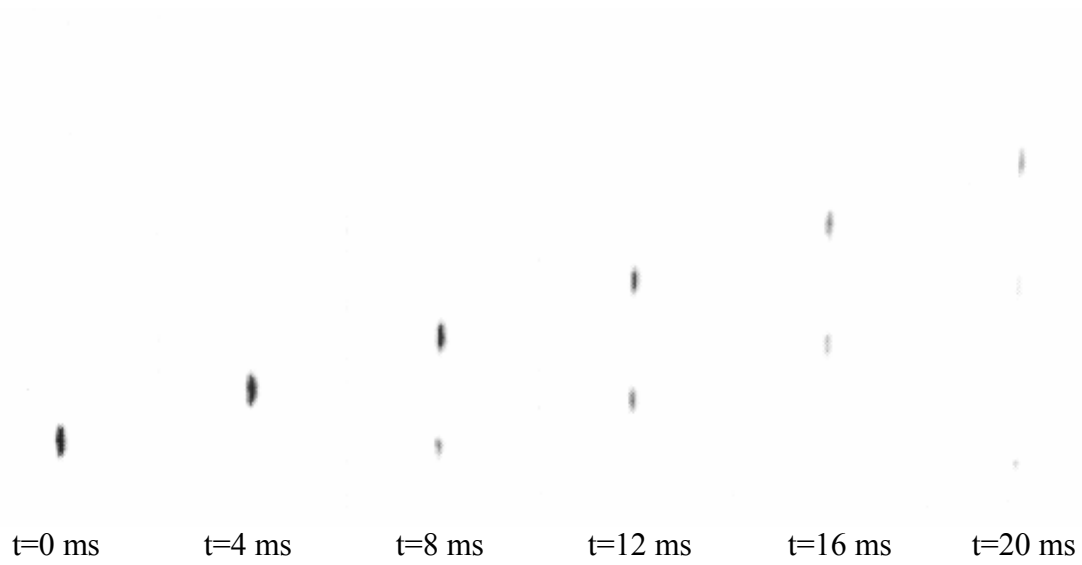


Figure 4.1. Frames of video images showing particle movement (some particle images were erased using a picture-processing code).

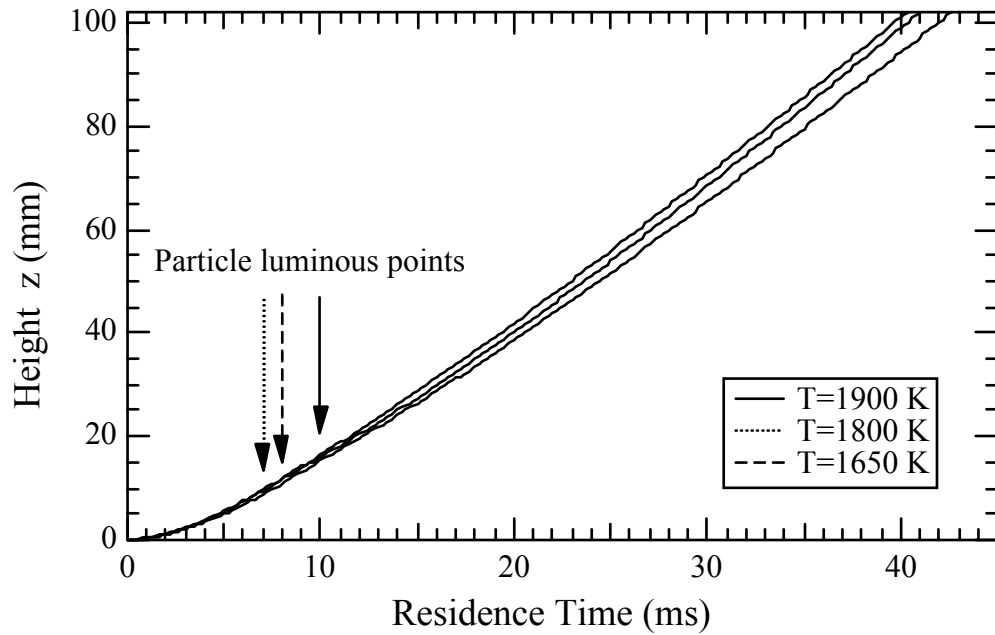


Figure 4.2. A plot of height versus time for a Pittsburgh #8 coal particle.

Thermophoretic Sampling

Three coals (Pittsburgh #8, Illinois #6 and Utah Hiawatha) were used in the thermophoretic sampling experiments. The results of these tests are discussed here.

Soot from a Butane Flame

In order to validate the sampling technique, thermophoretic sampling experiments were performed using the thermophoretic sampling device in a small butane diffusion flame. The sizes and shapes of soot particles from the butane flame were then compared with reported data in the literature. Figure 4.3 shows a TEM micrograph of soot particles collected from a butane flame. The grid was densely populated with aggregates of primary soot particles. The soot obtained from the butane flame appears to be similar to the soot of other hydrocarbon and polymer flames in the literature (Dobbins, et al., 1987; Jagoda, et al., 1980; Megaridis, et al., 1989) such as the one shown in Fig. 2.6. The large numbers of distinct soot particles collected in the butane flame, and the fact that the approximate sizes of the primary soot spheres and the agglomerates are comparable

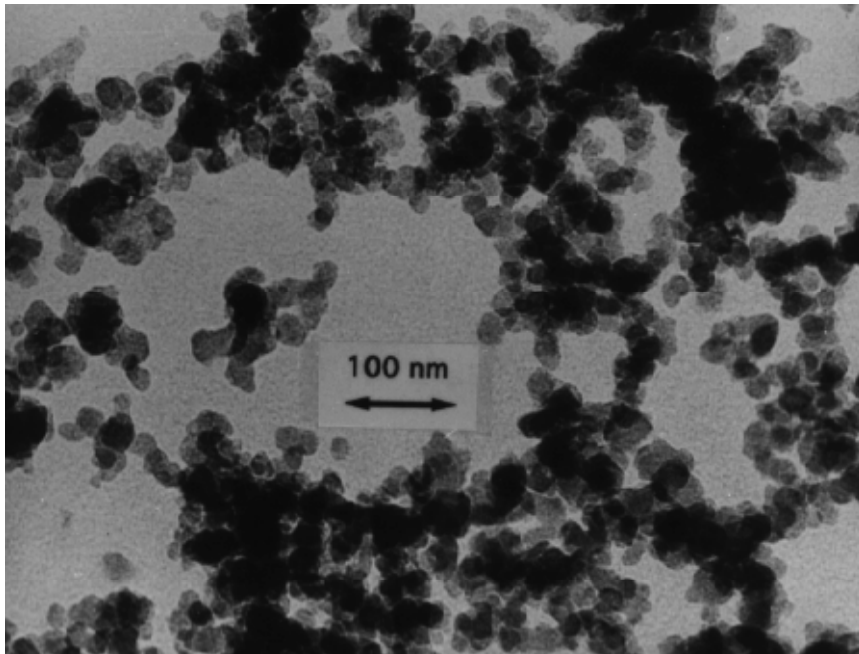


Figure 4.3. Micrograph of soot particles form a butane diffusion flame.

to reported values in the literature, is encouraging. The results of this simple experiment suggest that the sampling method can be confidently used to obtain similar data in coal-laden systems.

Coal-Derived Soot

Figure 4.4 represents a typical TEM micrograph of a soot agglomerate from the coal pyrolysis experiment in the flat flame burner system. The agglomerate, which consists of several primary soot particles, is similar to that of hydrocarbon flames, except that this kind of agglomerate is sparsely distributed on the grid due to the low volume fraction of the soot in the pyrolysis experiment. The size of primary soot particles is approximately 25 nm, which is comparable to the size of primary soot spheres from the butane flame. The sizes of the primary soot particles appear to increase to approximately 60 nm in the agglomerates collected at increased residence times, as shown in Figs. 4.5 and 4.6. Larger agglomerates, with diameters of approximately 800 nm, were observed at these increased residence times (see Figs. 4.5 and 4.6). Two types of agglomerates were observed: (a) spherical primary soot particles, as shown in Figs. 4.4 and 4.5; and (b) rod-like particles, along with primary soot particles, as shown in Fig. 4.6. The existence of the rod-like structures in the soot agglomerates was not expected. These structures show remarkable similarity to the tubular graphitic structures of buckminsterfullerene (C_{60}) and related compounds (e.g., Ugarte, 1992) reported in the literature.

In addition to the large soot agglomerates, individual (i.e., unagglomerated) small particles were also observed on the grids at early residence times (see Fig. 4.7). These small particles have a size similar to the particles that are connected together in the agglomerates. The solid deposits collected on the TEM grid are believed to be soot particles generated from coal tar or other volatiles. These particles correspond to the bright orange region in the reactor during coal pyrolysis experiments (see Fig. 3.2).

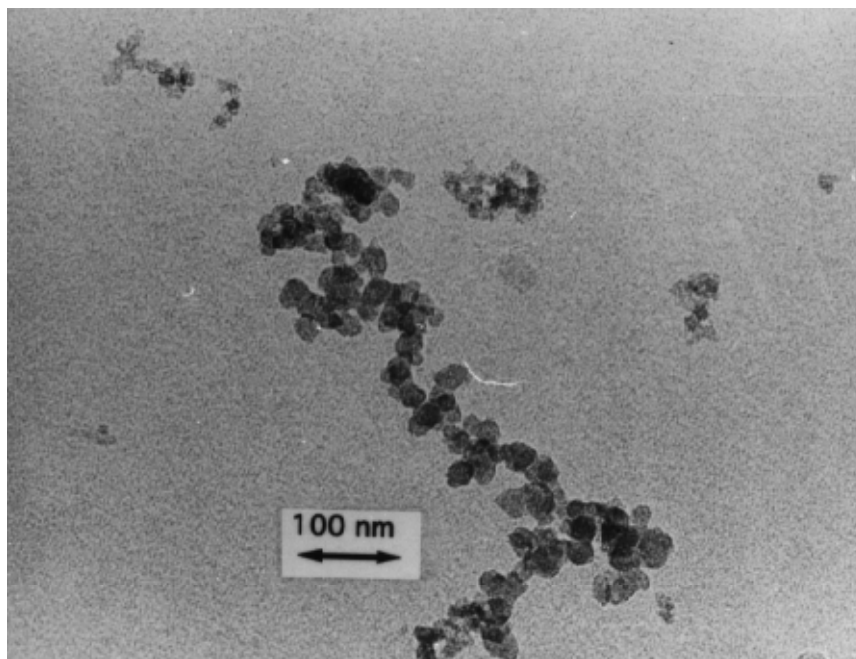


Figure 4.4. TEM micrograph of soot from the Utah coal, collected at 13 cm above the burner (65 ms).

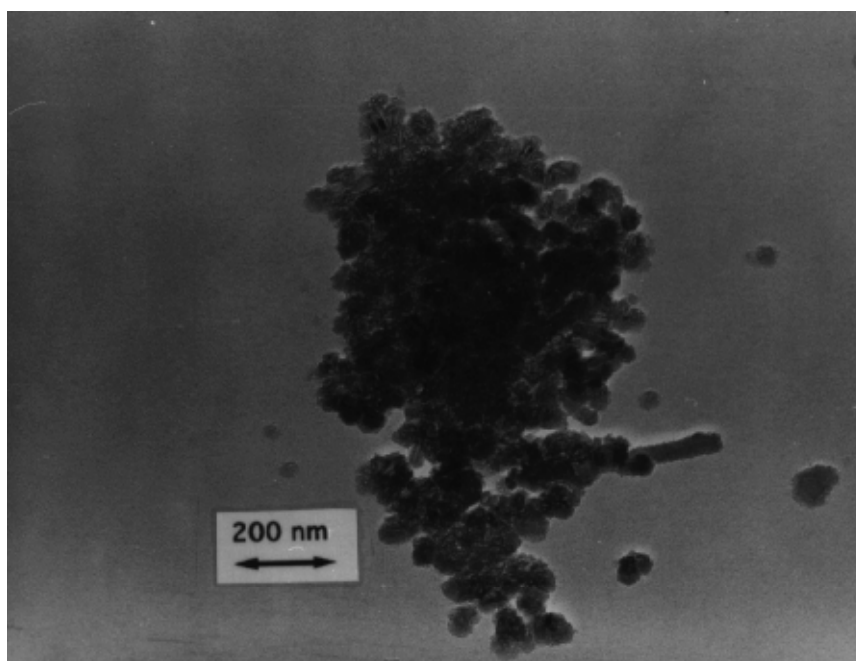


Figure 4.5. TEM micrograph of soot from the Utah coal, collected at 25.5 cm above the burner (128 ms).

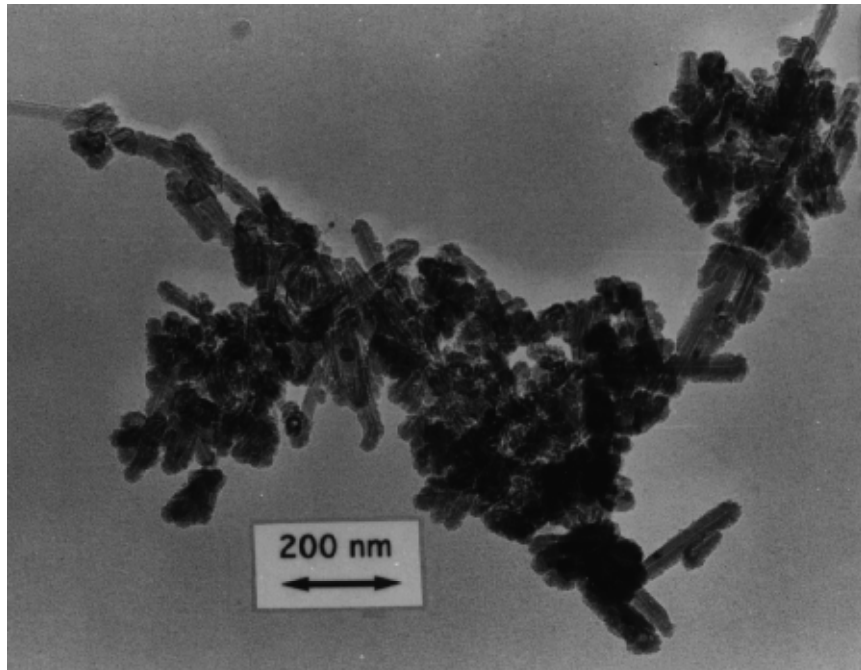


Figure 4.6. TEM micrograph of soot from the Utah coal, collected at 15.5 cm above the burner (78 ms).

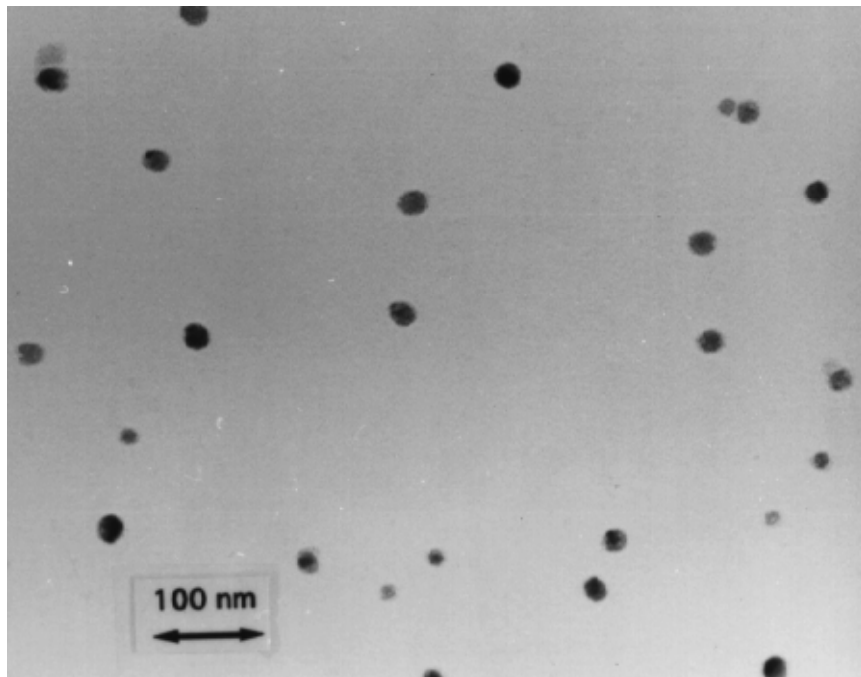


Figure 4.7. TEM micrograph of separated soot particles from the Pittsburgh #8 coal collected at 5.5 cm (28 ms).

No clear trend was observed as a function of coal type in these experiments. The lack of an observed trend is attributed to the limited data available in these qualitative thermophoretic sampling experiments. The coals studied were all high volatile bituminous coals; it is possible that low volatile coals or lower rank coals may exhibit different characteristics. The measured chemical compositions and yields of soot from suction probe sampling experiments in this reactor can help quantify the effects of coal type.

Evaporating Deposits

In addition to the stable solid particles deposited on the grid, a large number of unstable, liquid-like dark drops were observed on the grids for some locations in the reactor (see Fig. 4.8). Most of the unstable drops were observed along the copper bars at the edges of carbon-coated squares, and can vary in size from approximately 25 to 500 nm. These drops were unstable under the high-energy electron beams. When exposed to the electron beam, the drops boiled and finally disappeared, leaving voids with edges in the shapes of the peripheries of the original deposits. Non-boiling solid particles were occasionally observed inside the boiling drops (see Fig. 4.9). These drops were observed with square perimeters, as in Fig. 4.8, as well as with circular perimeters. The cause for the square structure of the evaporating deposits is unknown. Droplet deposits were only observed at low and intermediate residence times in the reactor, but not at high residence times.

It should be mentioned again that thermophoretic sampling can only extract small soot particles with a size less than 1 μm . No soot agglomerates larger than 1 μm were observed in the thermophoretic sampling experiments. However, in some examined test conditions, soot agglomerates much larger than 1 μm were observed. To sample the larger soot agglomerates and to obtain the quantitative soot yield data, particle bulk collection was performed.

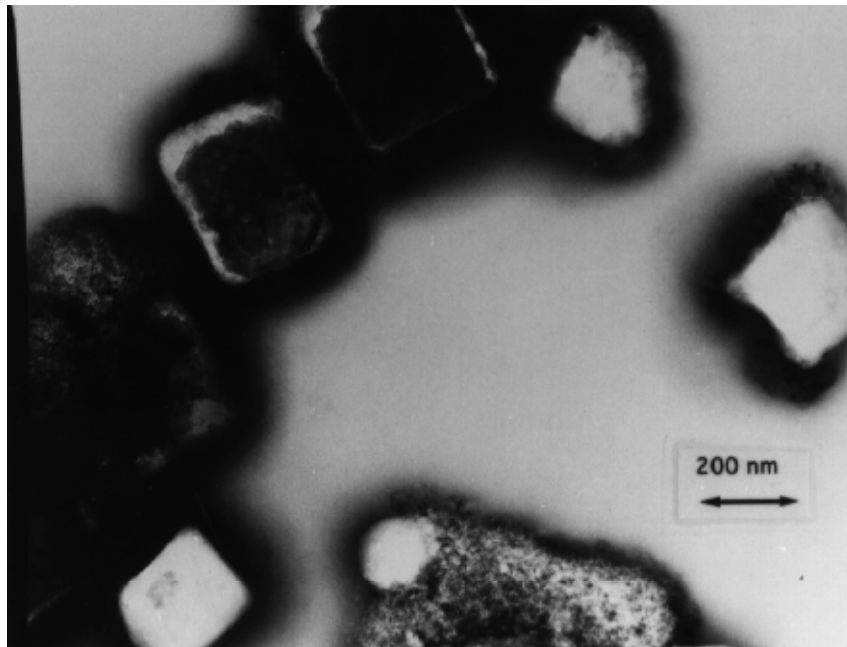


Figure 4.8. TEM micrograph of tar deposit from the Utah coal, collected at 20.5 cm (103 ms).

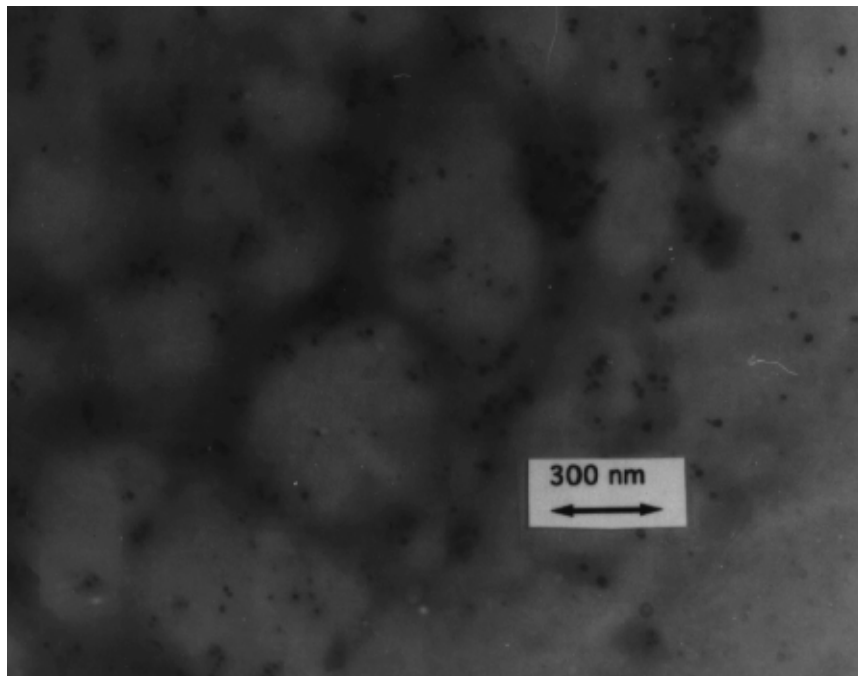


Figure 4.9. TEM micrograph of solid particles inside tar droplet from Utah coal, collected at 20.5 cm above the burner (103 ms).

Bulk Collection of Soot and Char Particles

Bulk samples were collected for all six coals at three temperatures and four sampling heights. The four collection heights were 25.4 mm, 50.8 mm, 76.2 mm and 101.6 mm, respectively. The corresponding residence times for each coal were calculated using Eqs. 4.6 and 4.7. The tests for three coals (Pittsburgh #8, Illinois #6 and Utah Hiawatha) were conducted twice to check reproducibility and to measure the amount of soot agglomerates existing in the char samples, which was not measured in the first series of tests.

General Description of Soot Collected By the Suction Probe

The bulk collection system was designed based on the assumption that the soot agglomerates should be less than 5 μm , as assumed by other researchers (Nenniger, 1986; Chen, 1991). No separation problems were reported by Nenniger, except for the Illinois #6 coal, which exhibited separation problems for unknown reasons. The basis for designing this separation system was that a cut point around 5 μm should be large enough to separate soot from char. The experiments performed in the flat flame flow reactor as part of this dissertation yielded soot agglomerates as large as 20 μm . The existence of these large soot agglomerates was first noticed by the fact that the collected char samples at longer residence times were always dark black and occupied much more volume than the parent coal, while the char samples collected at the lowest residence time were usually gray and occupied less volume. Shaking the vial containing the longer residence time sample caused stratification in the sample, with a low-density dark layer sitting on top of a gray layer, as illustrated in Fig. 4.10. By ashing the sample of the top layer and the sample of the bottom layer separately, it was found that the sample of top layer had negligible ash content. CHN analyses on the samples of Illinois #6 also showed that the material on top had about 90 wt% carbon, much higher than the carbon content of ordinary devolatilized char particles (~75%).

In order to further analyze the type of particles collected in the cyclone, the samples were examined under a scanning electron microscope (JEOL Model 840A). An SEM micrograph of a Illinois #6 soot/char mixture collected in the cyclone at a residence time of 34 ms and temperature of 1900 K is shown in Fig. 4.11. The bright particles in Fig. 4.11 are 10 to 30 μm in diameter, and the gray particles are around 70 μm ; the gray particles are definitely the char particles and are similar to those reported by Gale (1994). It can also be observed that the bright particles tend to fuse together to form a densely-packed aggregate. The brightness of a particle in an SEM picture is related to the roughness of its surface. The surface structures of a bright particle and a gray particle at high magnifications are shown in Figs. 4.12 and 4.13 respectively, from which it can be seen that the gray char particle has a very smooth surface. In contrast, the surface of the bright particle consists of a large number of tiny particles in the 50 to 100 nm range. The surface structure of the bright particle are similar to what is shown in Fig. 4.14, a micrograph of the soot deposited on the soot-leg filter, collected at the same residence time and from the same coal. X-ray analysis was also performed on both gray particles and bright particles using an X-ray analyzer (Model Link ISIS) in the SEM facility. Only carbon and gold, which was used to coat the sample for better conductivity, were detected as the constitutive elements of the surfaces of the bright particles, while other metal elements were found on the surface of the gray particles. The X-ray tests eliminated the conjecture that the bright particles might be from grains of pyrite in the coal, as reported by Baxter (1995a). In fact, a few bright pyrite grains were found in the char sample, but their sizes were much smaller ($<5 \mu\text{m}$). It is obvious that the bright particles are not fractured pieces of char particles, and that the gray particles must be the devolatilized char particles. The fact that no char particles smaller than 43 μm were found during the sieving of the char samples suggests that little char fragmentation occurred during devolatilization. From Fig. 4.11, it can also be seen that the char

particles are similar in

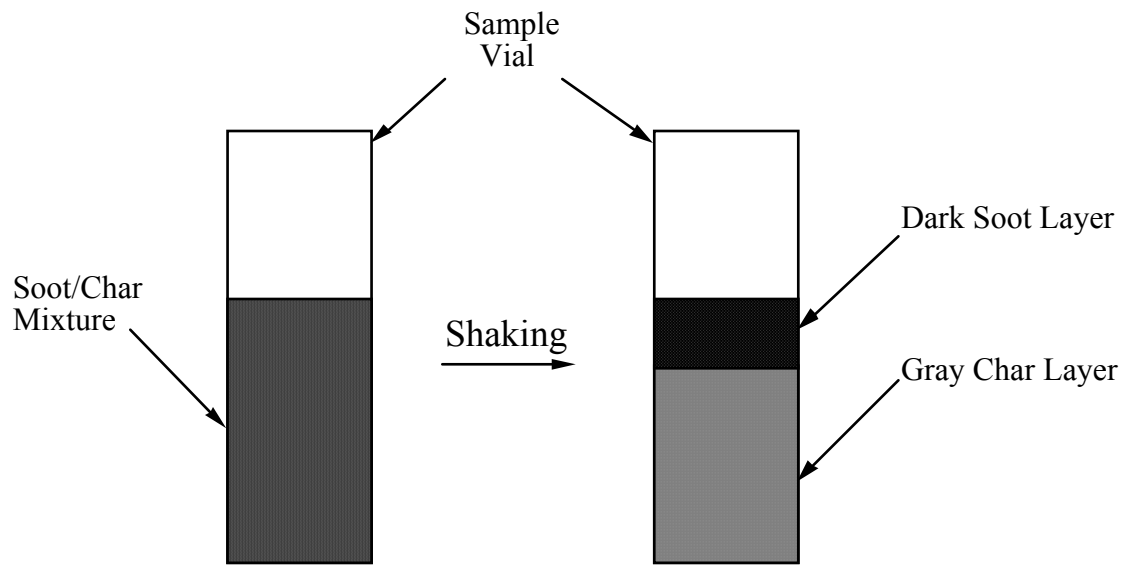


Figure 4.10. Soot agglomerate layer formed upon shaking the char/soot sample.

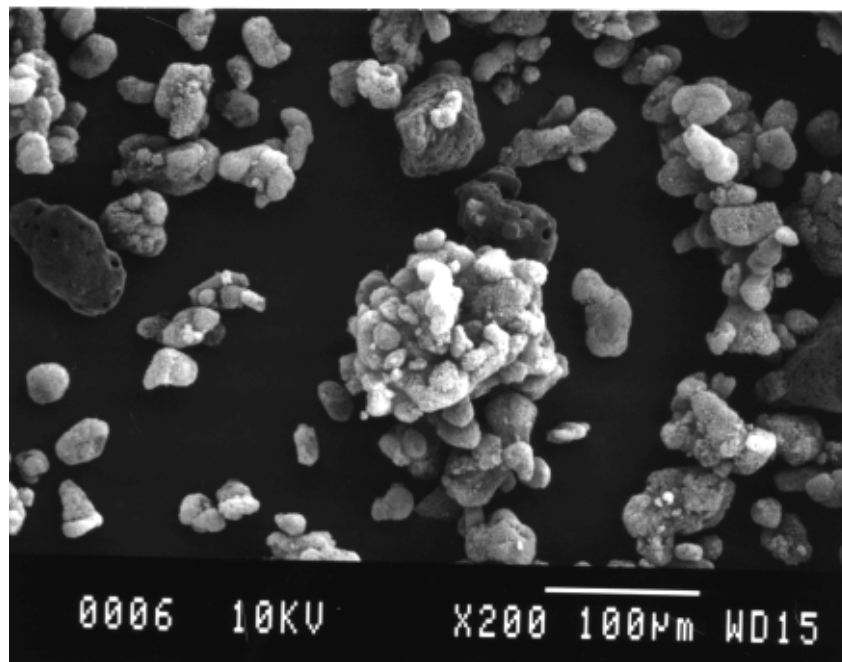


Figure 4.11. SEM micrograph of soot/char mixture.

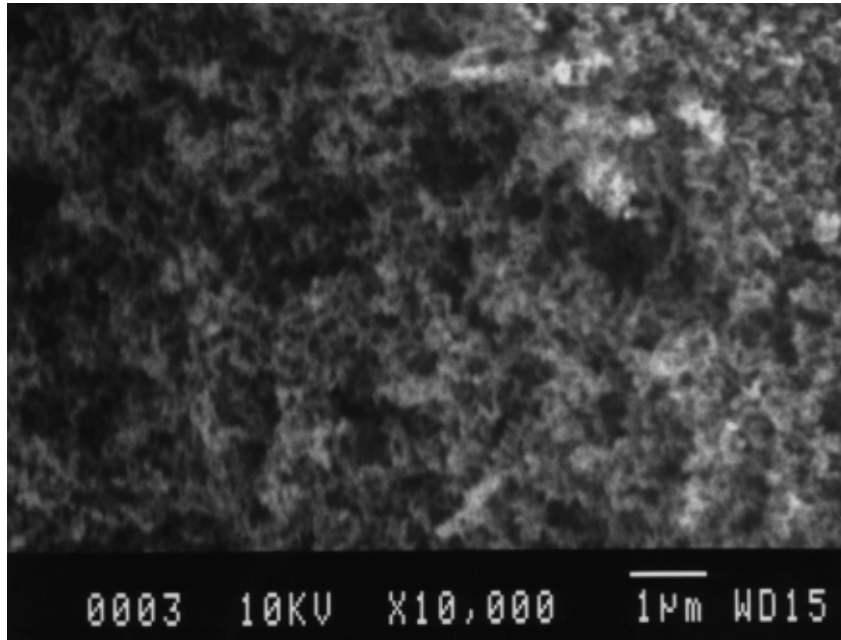


Figure 4.12. SEM micrograph showing the surface of a bright particle.

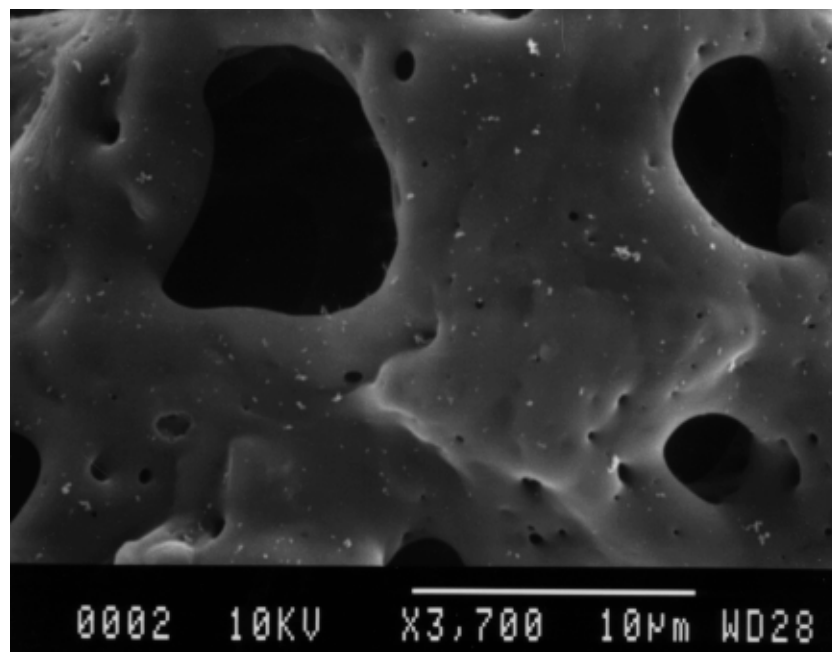


Figure 4.13. SEM micrograph showing the surface of a gray char particle.

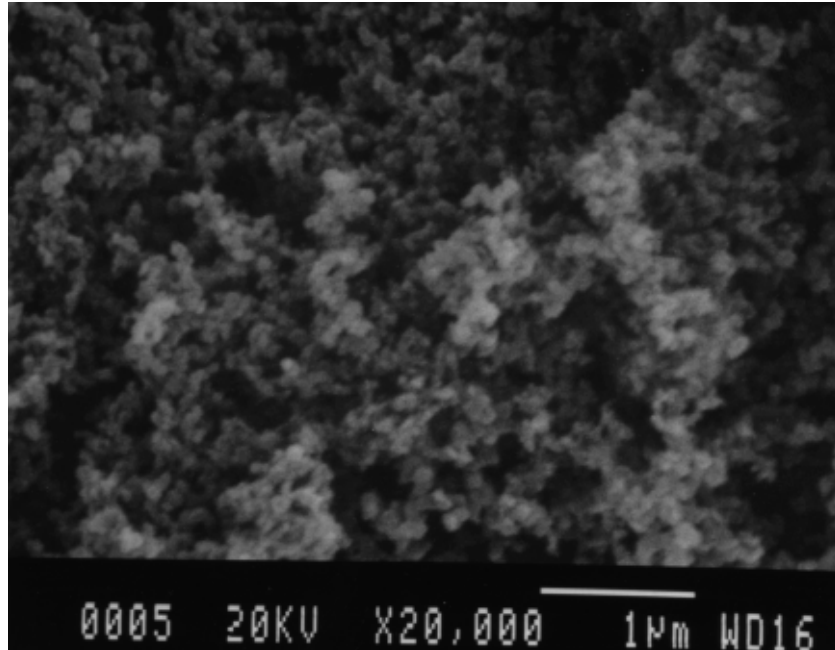


Figure 4.14. SEM micrograph of small soot particles collected on a soot filter.

size to the parent coal particles. The swelling or shrinking of the coal particles was insignificant during the devolatilization at such a high heating rate, which was comparable to the result reported by Gale, et al. (1994). Furthermore, the sizes of the primary soot particles shown in Figs. 4.12 and 4.14 are comparable to the sizes of the primary particles of soot agglomerates extracted by thermophoretic sampling (see Figs. 4.4 through 4.6). In Fig. 4.14, the chain-like shapes of soot agglomerates can not be seen because soot particles are packed tightly during the filtration.

Soot Yield and Volatiles Yield

One of the main purposes of the bulk sampling experiments was to determine the soot yield as a function of temperature, residence time and coal type. Possible errors in the soot yield data include the deposition of soot on the walls of collection system, the escape of volatiles or soot particles around the sides of the suction probe, the loss of soot

in sieving the char/soot mixture, and the vaporization and recondensation of mineral matter at the high temperatures involved in this experiment. It was found that about 10% of small soot particles ($< 5 \mu\text{m}$) deposited on the inner walls of the virtual impactor and cyclone. The yields of small soot particles were corrected for this 10% deposition loss. To examine if aerosols (collected on the filters) contain certain amount of tar, extractions with dichloromethane were performed on collected samples from the Pittsburgh #8 coal. The samples were transferred to the solvent, sonicated, and finally filtrated by nylon filters with a pore size of $1 \mu\text{m}$. The difference in weight between the initial aerosol and filtrated soot was assumed to be the tar yield. Only a small percentage of tar (less than 6% of total aerosol) was observed at the lowest collection height (25.4 mm) at the lowest gas temperature (1650 K). The tar yield observed in any other test conditions were found to be insignificant. Therefore, 6% tar yield was correct for each coal only in the condition of 25.4 mm and 1650 K.

Figures 4.15 through 4.20 show the measured soot yields and total volatiles yields on a dry ash-free basis versus residence times in the three temperature conditions. The soot yields for three coals (Pittsburgh #8, Illinois #6 and Utah Hiawatha) were divided into two parts, one for particles less than the cut point diameter ($5 \mu\text{m}$) and the other for those larger than $5 \mu\text{m}$. The distribution of soot yields among these two size fractions is related to the soot agglomeration after primary soot particles are formed. For Pocahontas #3, Dietz, and Zap coals, only the yields of small soot particles ($< 5 \mu\text{m}$) are presented. The reproducibility of the soot yield data was checked, and in most cases the relative errors are within 5%.

From these figures, it can be seen that the total volatiles yield of the Pittsburgh #8, Illinois #6, Utah Hiawatha, and Pocahontas #3 coals did not change much with residence time, with the exception that total volatiles yield increased between 15 ms and 25 ms for Pocahontas #3 coal at 1650 K. The constant total volatiles yield suggests that for these four coals, the devolatilization process was completed at the lowest residence

time

(about

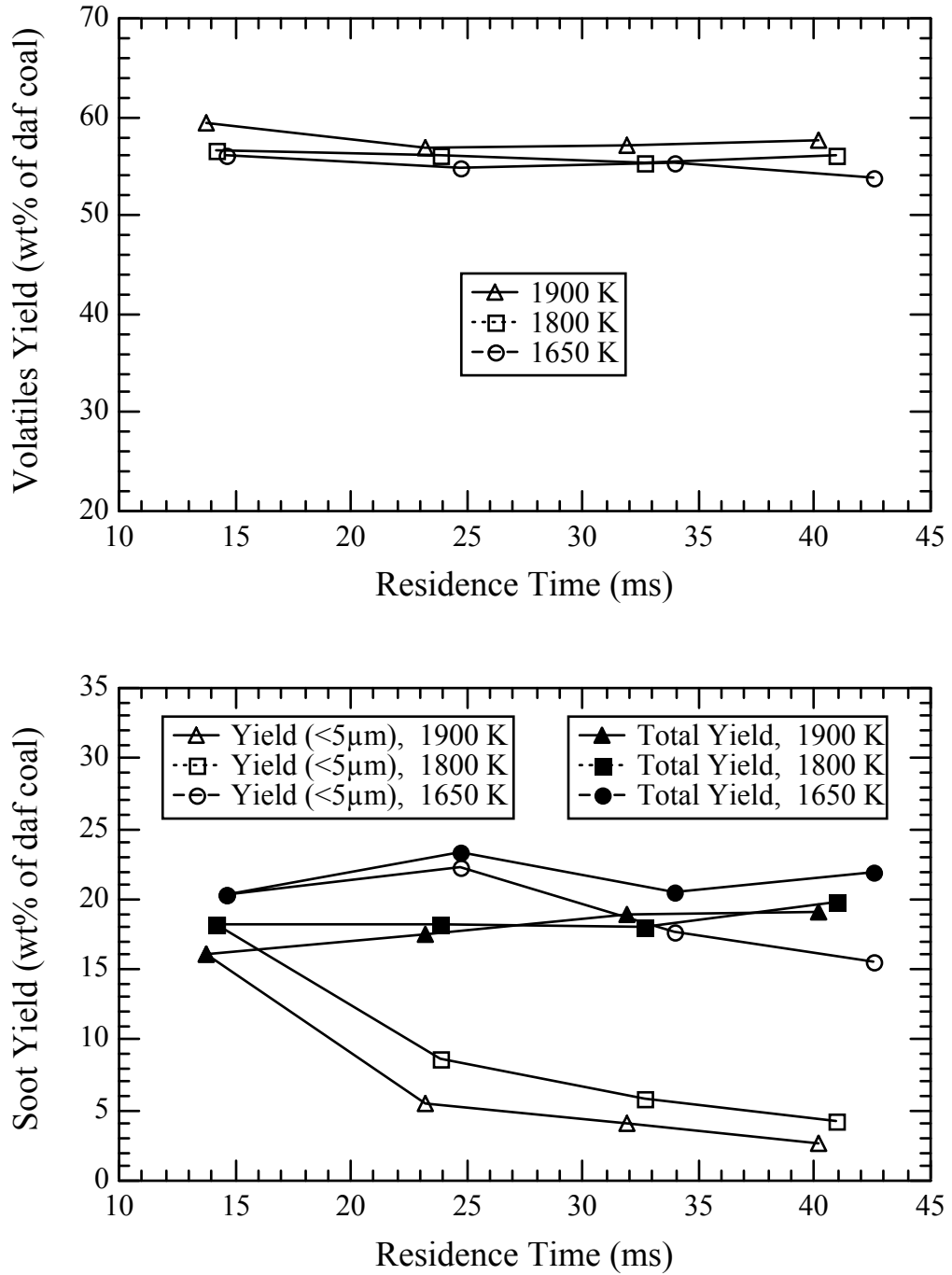


Figure 4.15. Measured volatiles yields and soot yields for Pittsburgh #8 coal.

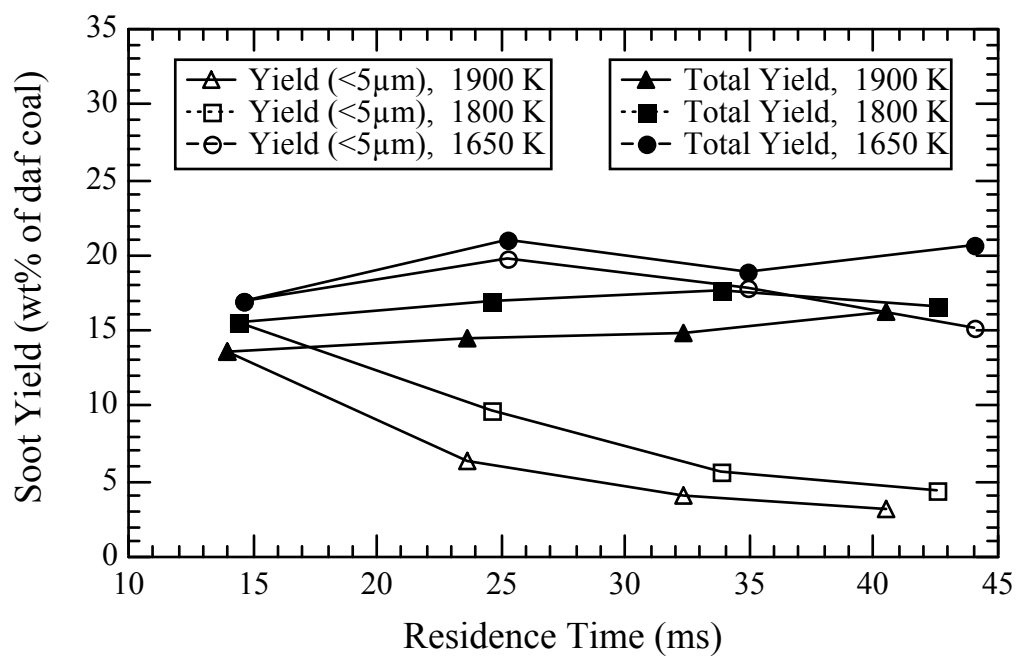
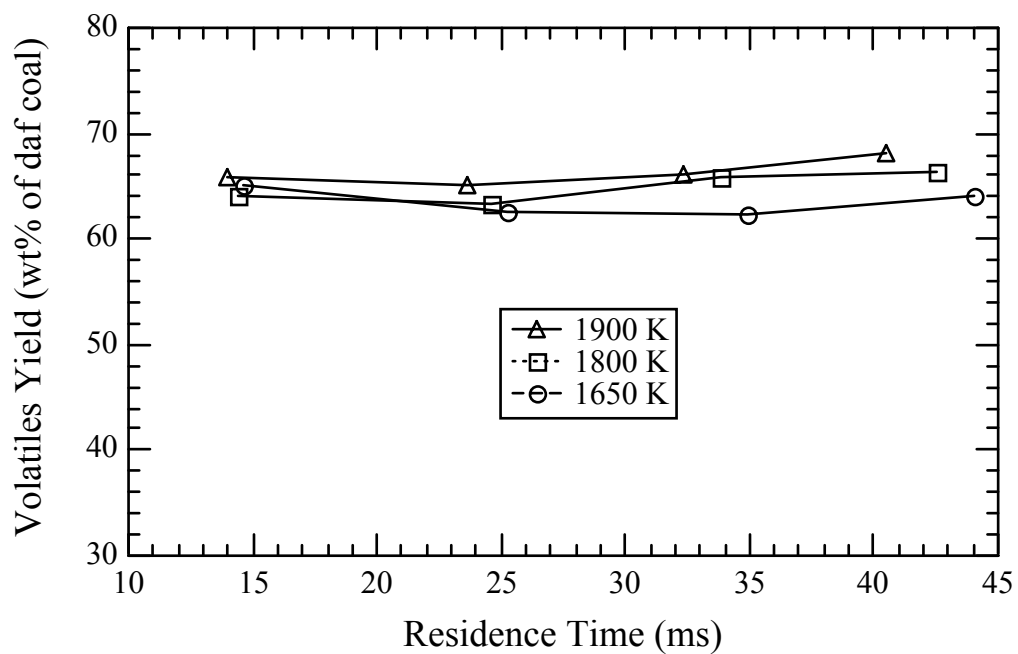


Figure 4.16. Measured volatiles yields and soot yields for Illinois #6 coal.

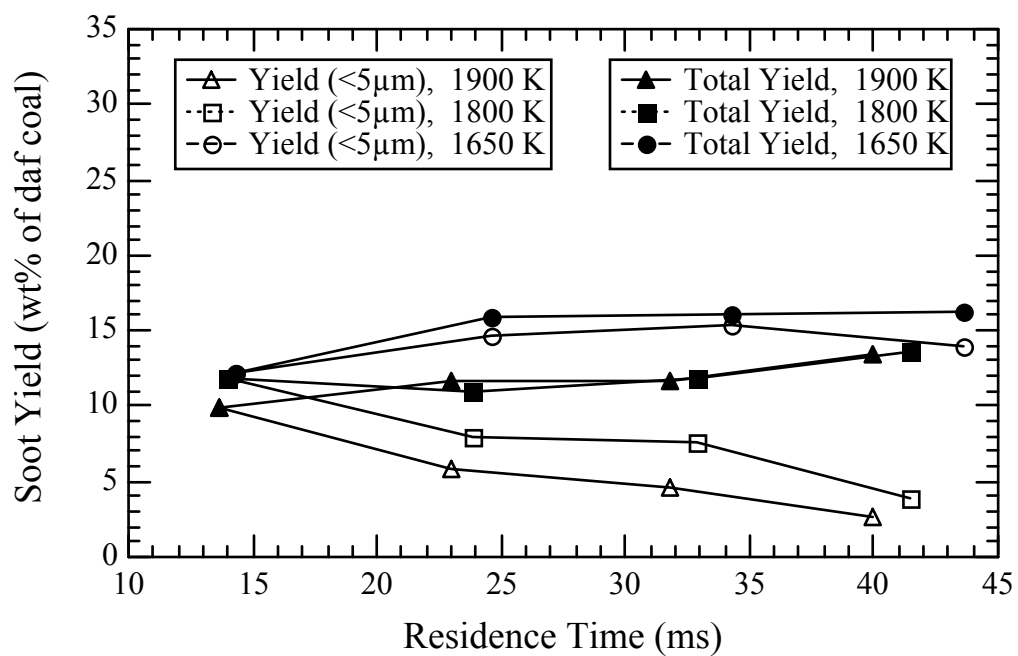
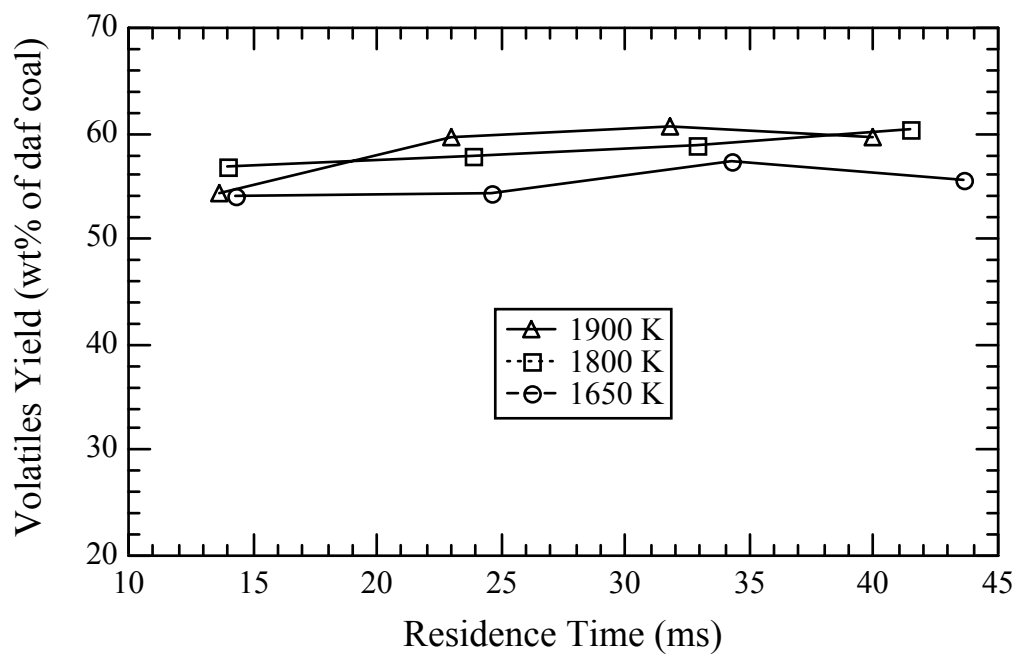


Figure 4.17. Measured volatiles yields and soot yields for Utah Hiawatha coal.

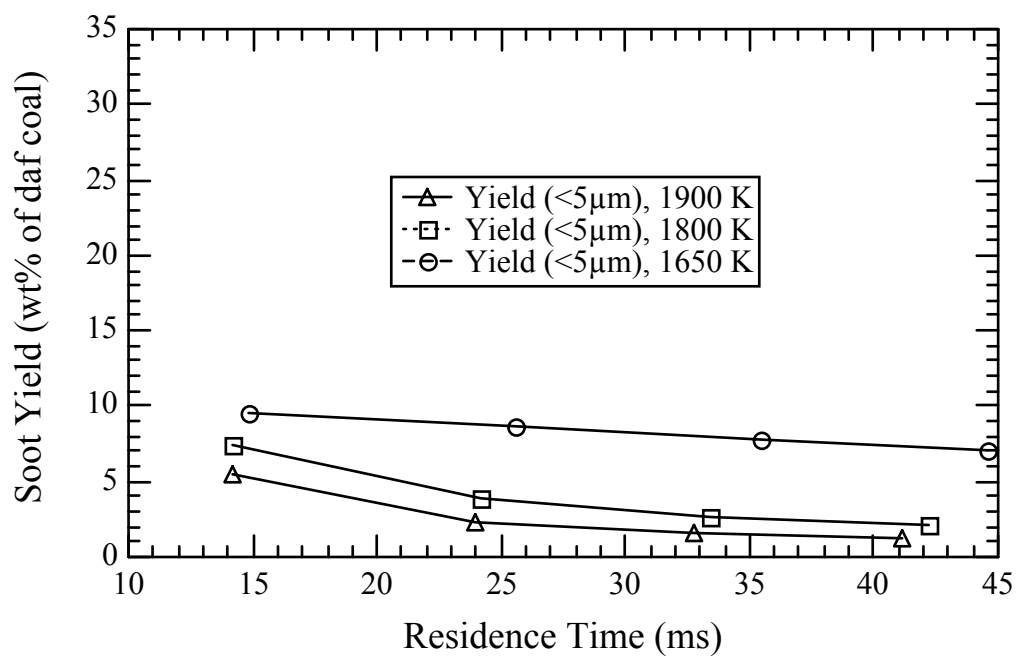
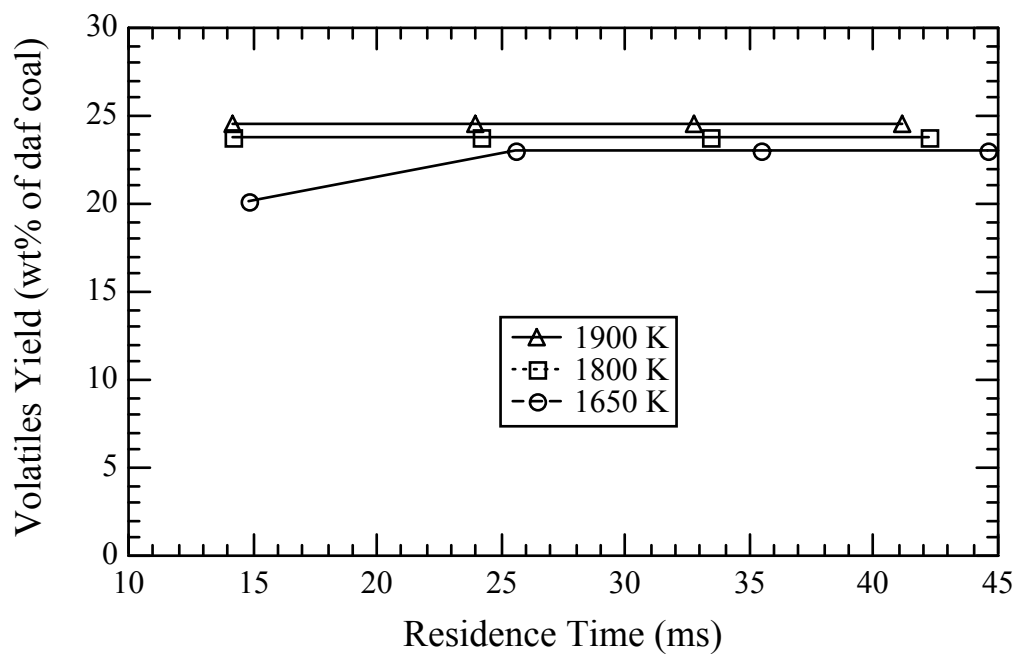


Figure 4.18. Measured volatiles yields and soot yields for Pocahontas #3 coal.

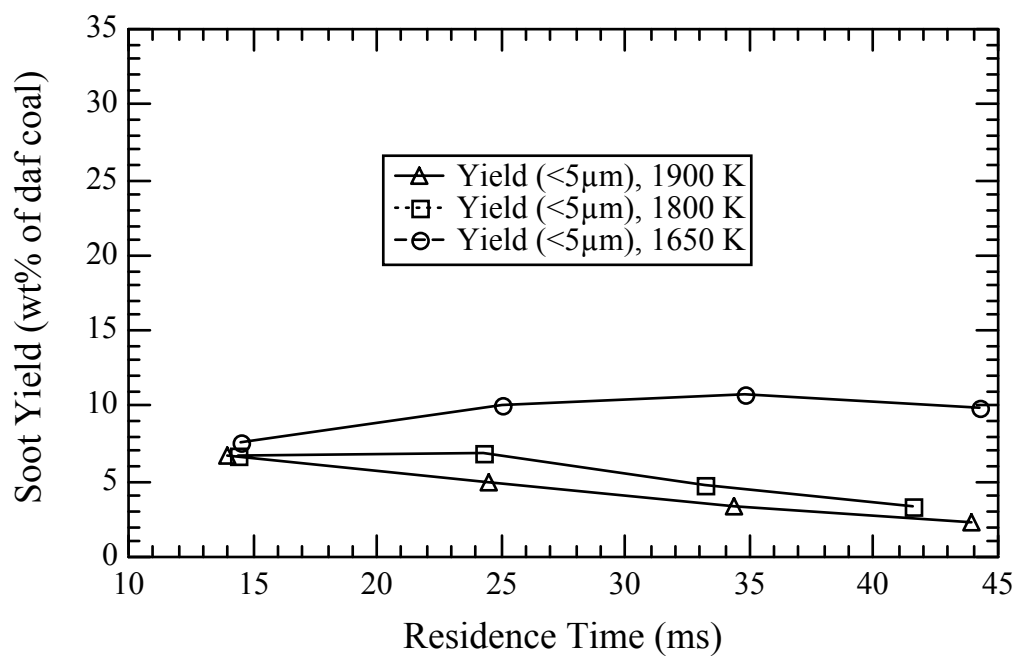
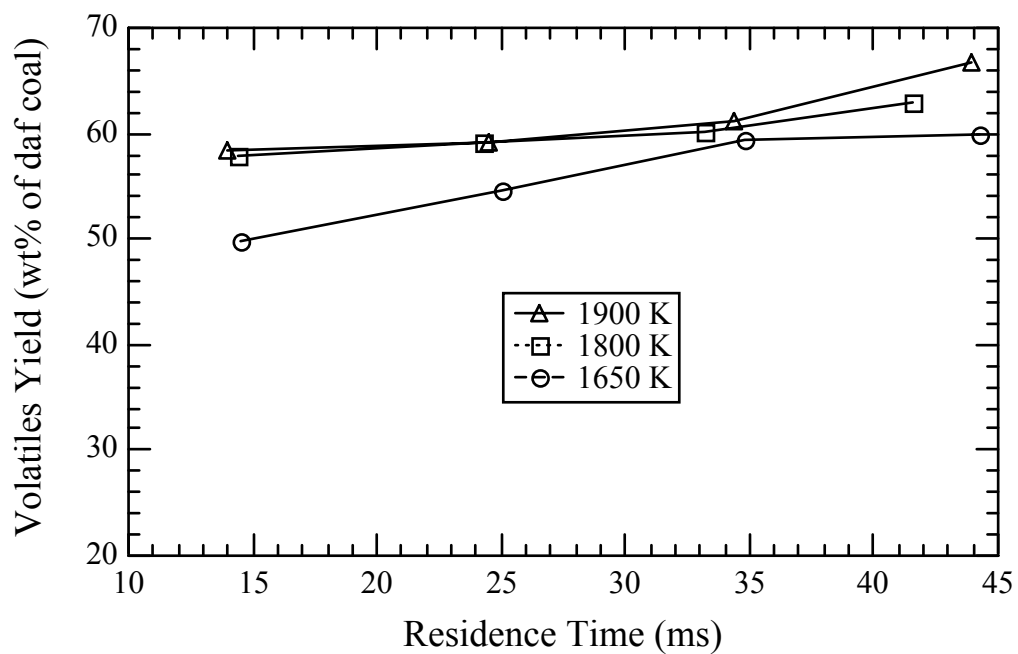


Figure 4.19. Measured volatiles yields and soot yields for Dietz coal.

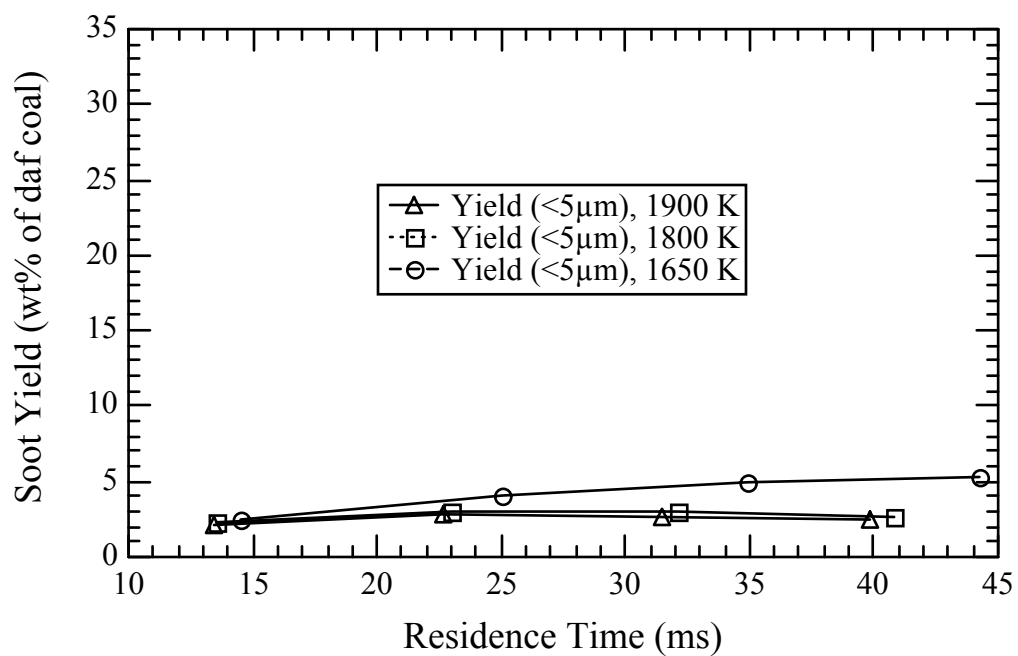
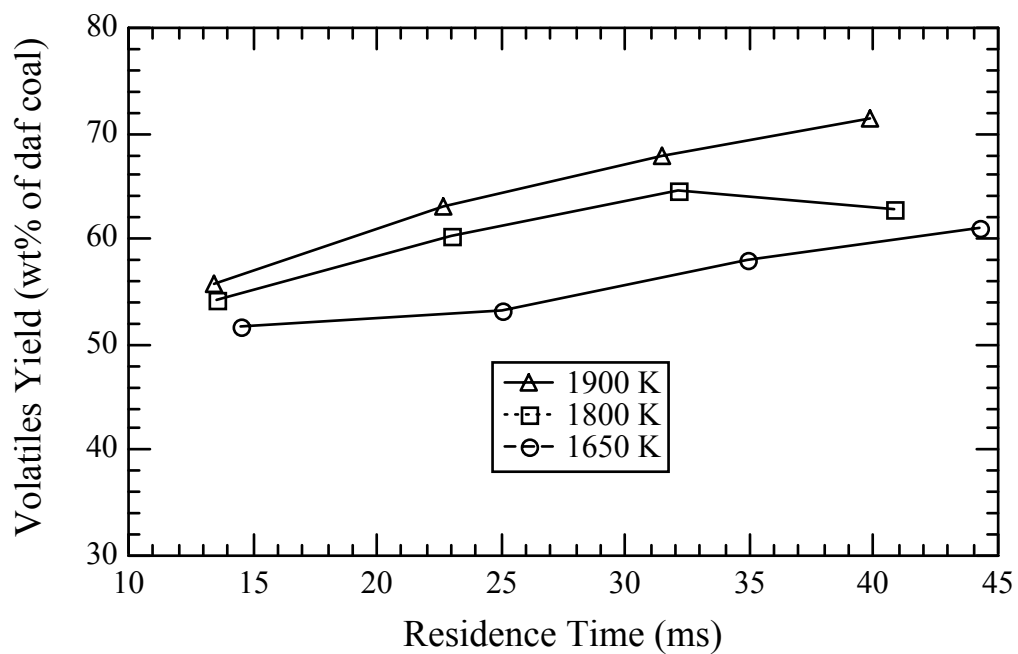


Figure 4.20. Measured volatiles yields and soot yields for Zap lignite.

15 ms), with no tar or light gases released after that time. On the other hand, the total volatiles yields of the Dietz coal and Zap lignite increased about 10% (daf) after the earliest collection point. This late devolatilization is expected for low rank coals, and is most likely due to the pyrolytic release of light gases from the char. Low rank coals and chars contain high percentages of side chains (i.e., aliphatic material) which are precursors to light pyrolysis gases. However, the increase in mass release could also be caused by the vaporization of certain mineral matter species, such as Na and Ca. The total volatiles yields plotted in Figs. 4.15 through 4.20 were based on mass balance measurements. The mass balance data were also checked using the Ti tracer technique. The values of mass release obtained by these two methods were very close (within 5% in calculated mass release), with ICP method usually showing a lower value. Figure 4.21 is a comparison between these two methods.

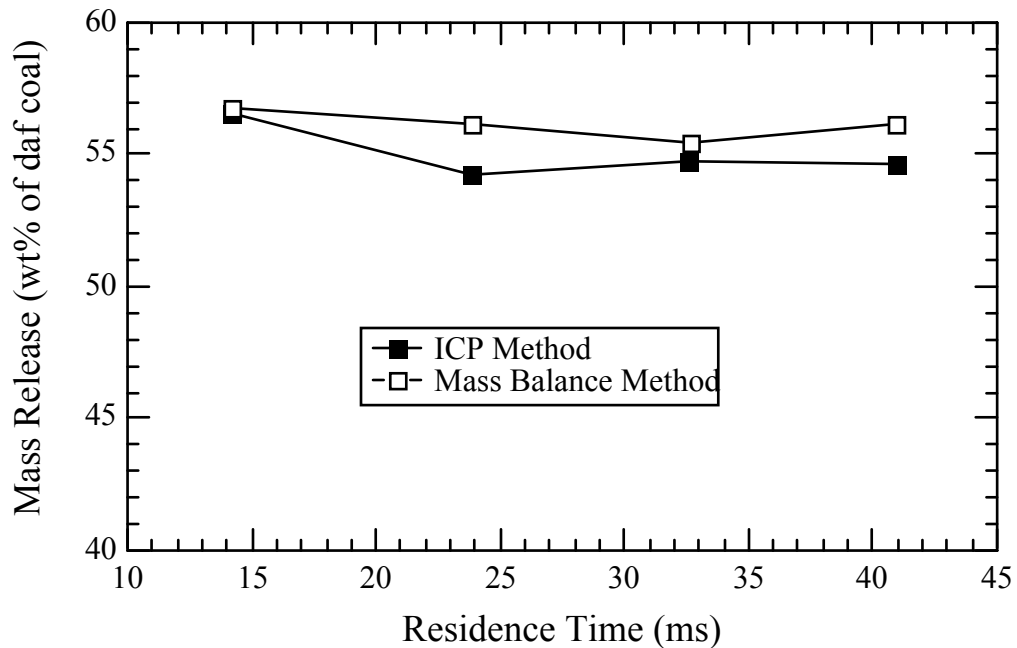


Figure 4.21. A comparison between mass balance method and ICP method (mass release of Pittsburgh #8 coal at 1800 K).

At 1800 K and 1900 K, the total soot yields for three coals (Pittsburgh #8, Illinois #6 and Utah Hiawatha) remained almost unchanged, with only a small increase after the lowest collection height, or 15 ms residence time. This means that the soot formation process is very fast in these two temperature conditions. At 1650 K, the increases of total soot yields between 15 and 25 ms were higher than those at 1800 K and 1900 K, which means significant amount of soot is still being formed during that period at lower temperatures. The slight increases in total soot yields at higher residence times (from 25 to 43 ms) were probably due to the mechanism that tar molecules are broken into small molecules which later attach to soot particles. Meanwhile, the almost constant soot yield or slight increase in soot yield after 15 ms indicates that oxidation or gasification of soot by oxygen-containing species (OH, H₂O, and CO₂) at long residence times is negligible. While the total mass of soot did not vary much with residence time, the size distribution of soot particles did change. At the lowest residence time (15 ms), all soot particles collected were smaller than 5 μm (i.e., there were no dark particles in the collected char sample). The percentage of larger agglomerates increases monotonically with residence time, indicating a continuous agglomeration process.

Temperature had a noticeable effect on the total soot yield. The total soot yields (at the 10.2 cm collection height) versus temperature for Pittsburgh #8, Illinois #6 and Utah Hiawatha coals are plotted in Fig. 4.22. In the temperature range examined, the total soot yield for each coal decreased slightly as the pyrolysis temperature increased. This trend might be related to changes of PAH stability at different temperatures or to the reactions of soot precursors with oxygen-containing species.

Temperature had significant effect on soot agglomeration. Figure 4.23 shows plots of soot yield (<5 μm) versus temperature at 10.2 cm collection height. For all six coals, the soot yields of small particles decrease drastically as the temperature is increased, due to the fast agglomeration of small particles at high temperatures. In Fig.

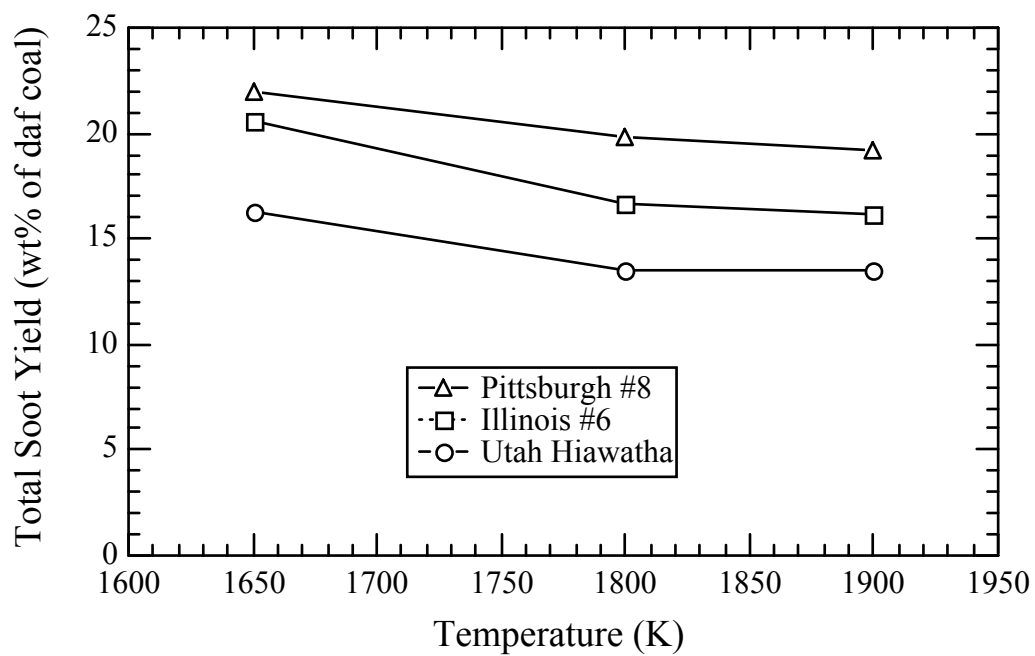


Figure 4.22. Effect of pyrolysis temperature on total soot yield.

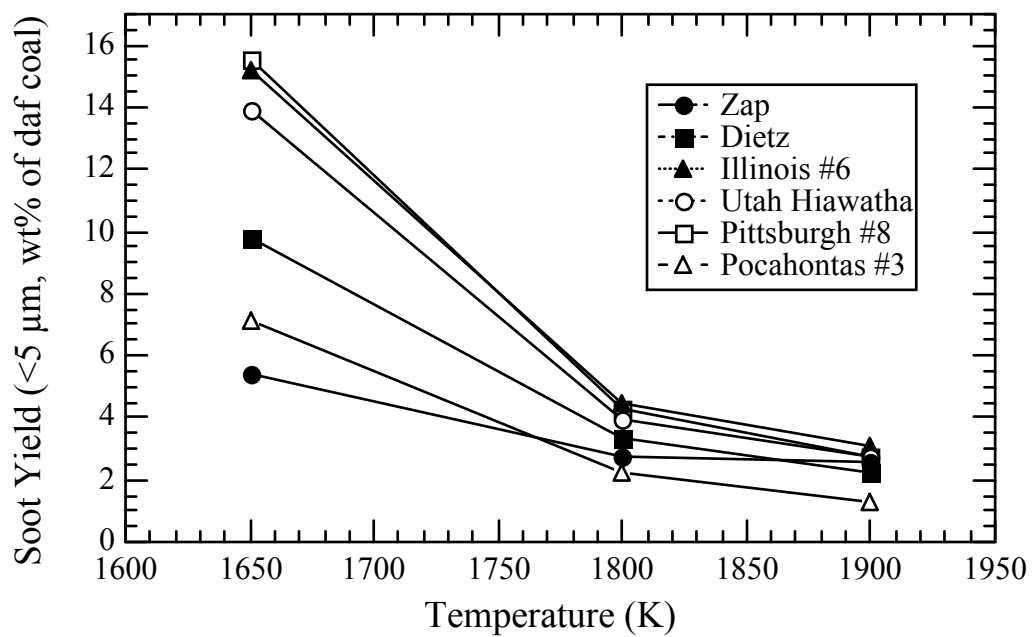


Figure 4.23. Effect of pyrolysis temperature on soot yield (< 5 μm).

4.23, the effect of temperature on small aerosol yield for Zap lignite is smaller, which is probably due to high percentage of ash is condensed onto the soot particles at higher temperatures (the data shown in Fig. 4.23 are actually for the aerosols including the possible ash content).

Elemental Composition of Products

Figures 4.24 through 4.28 are plots of weight percentages of carbon, hydrogen and nitrogen in the soot samples ($<5 \mu\text{m}$) versus pyrolysis temperature at the lowest and the highest collection heights for 5 coals (Pittsburgh #8, Illinois #6, Utah Hiawatha, Pocahontas #3 and Dietz). The reason that the elemental composition in these figures does not sum to 1.0 is the presence of S and O in the samples. Due to the limited accuracy of the CHN analyzer and the small amount of sample available for analysis, the data shown here contain large experimental errors ($\pm 2\%$ for C, $\pm 0.5\%$ for H and $\pm 0.3\%$ for N). However, some trends can still be seen in these figures. One trend is that the pyrolysis temperature has certain effect on hydrogen content in coal-derived soot. For soot samples from all 5 coals examined, the weight percentage of hydrogen at 1650 K is higher than those at 1800 and 1900 K. For instance, the weight percentage of the soot from the Pittsburgh #8 coal collected at 2.54 cm changed from 1.5% at 1650 K to 0.9% at 1800 K and 0.8% at 1900 K. Moreover, at 1650 K, hydrogen content is higher at the low residence time (~ 15 ms) than that at the high residence time (~ 45 ms). The corresponding C/H mole ratio for the 1650 K experiments changed approximately from 5 to 10 as a function of residence time. At high temperatures (1800 and 1900 K), the effect of residence time on hydrogen content is hardly seen, which indicates that the soot particles have been mature at 15 ms in these temperature conditions. The weight percentage of nitrogen in the soot samples collected is in the range from 0.3 to 0.9 percent. No clear effects of temperature and residence time on nitrogen content were found due to the large amount of scatter in these data.

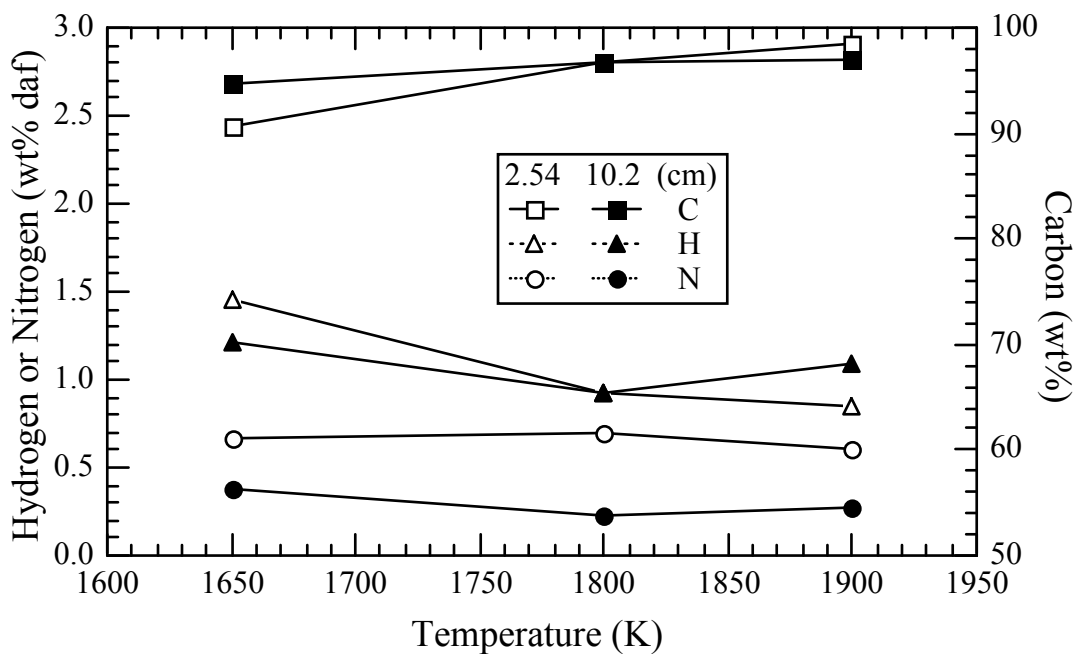


Figure 4.24. Elemental composition of the soot from Pittsburgh #8 coal.

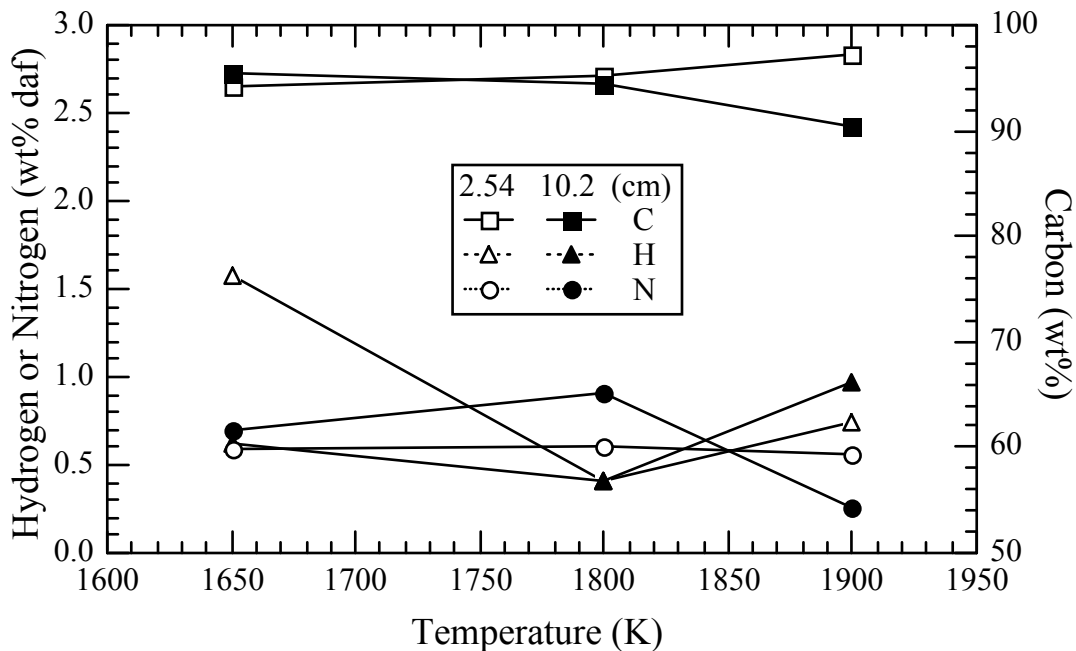


Figure 4.25. Elemental composition of the soot from Illinois #6 coal.

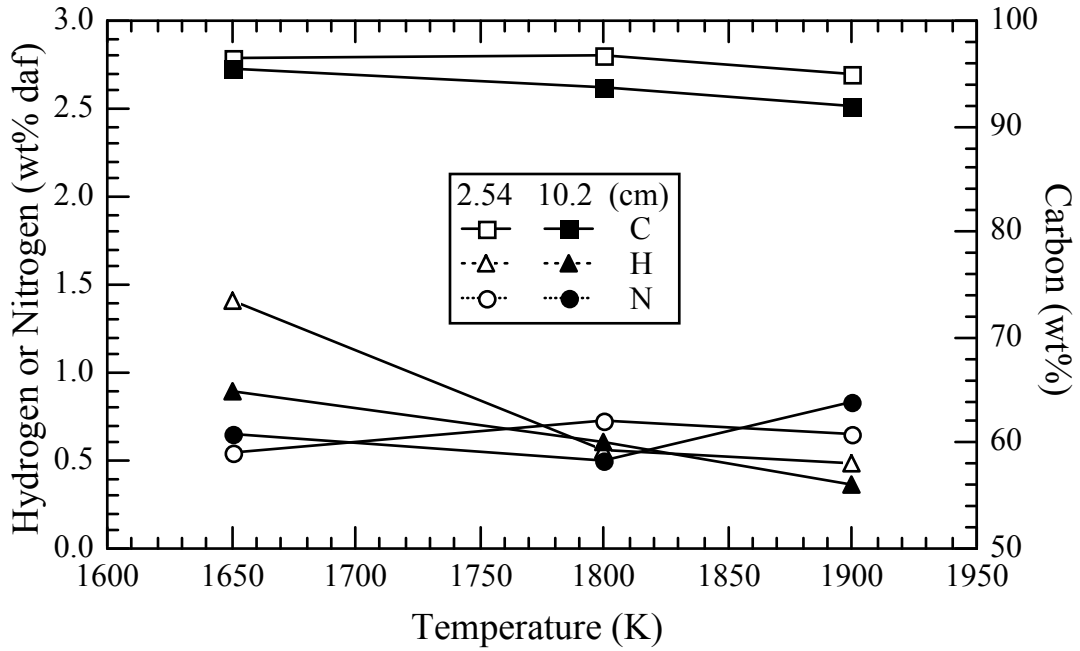


Figure 4.26. Elemental composition of the soot from Utah Hiawatha coal.

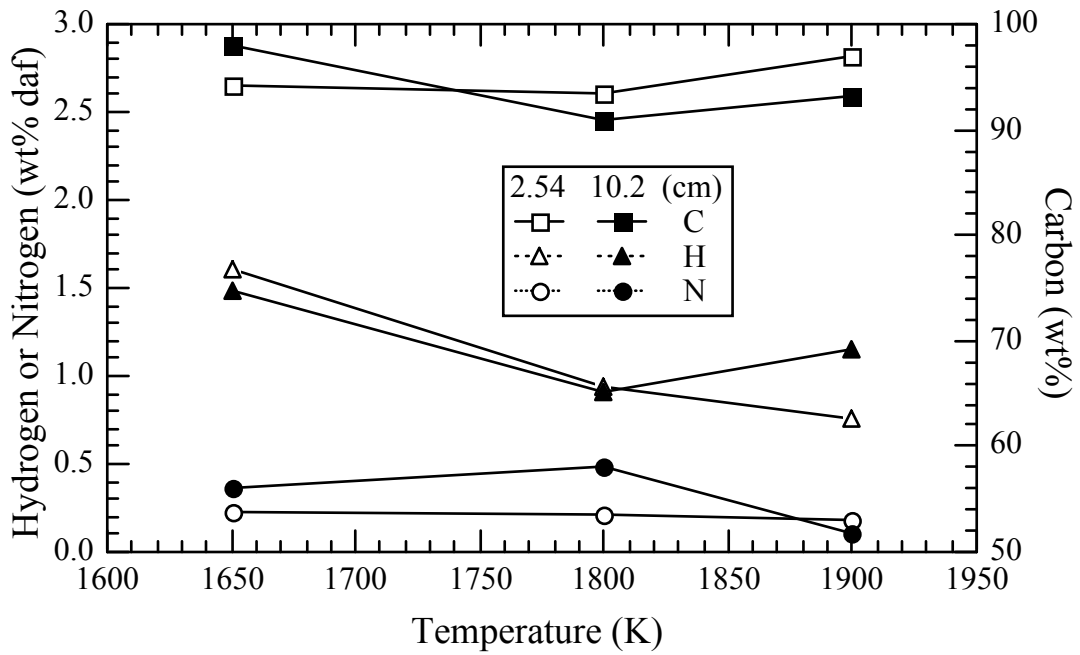


Figure 4.27. Elemental composition of the soot from Pocahontas #3 coal.

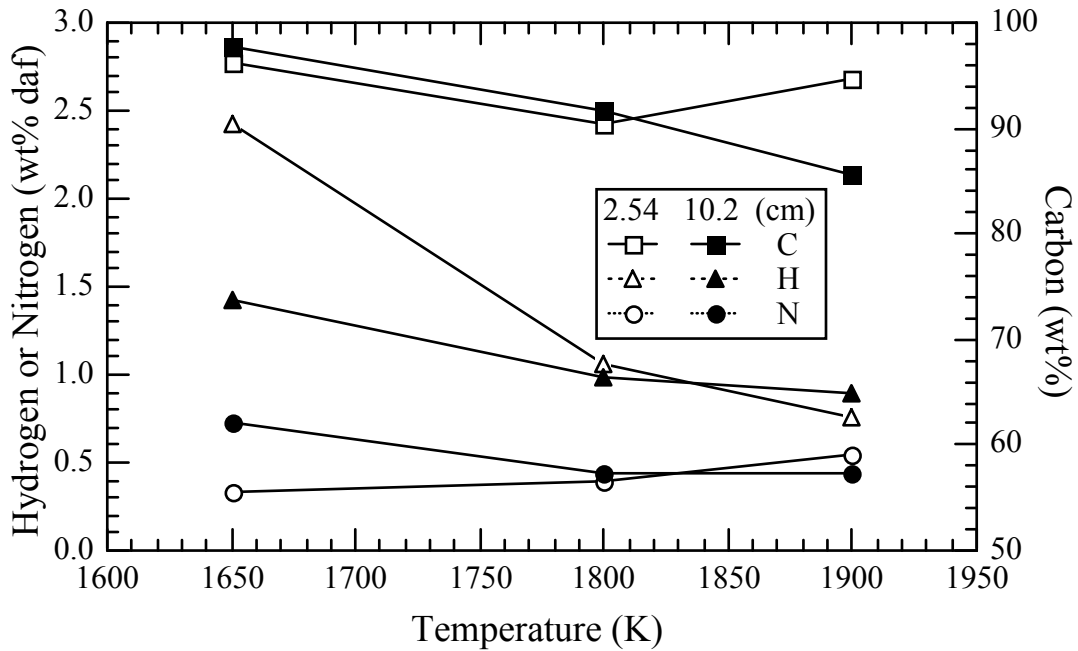


Figure 4.28. Elemental composition of the soot from Dietz coal.

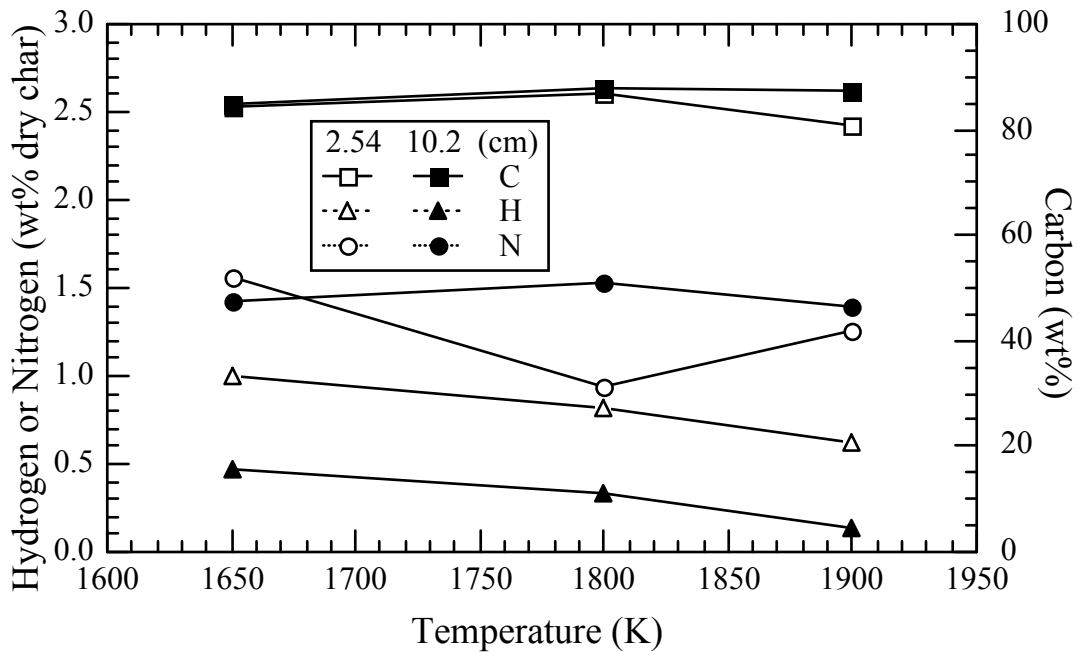


Figure 4.29. Elemental composition of the char from Pittsburgh #8 coal.

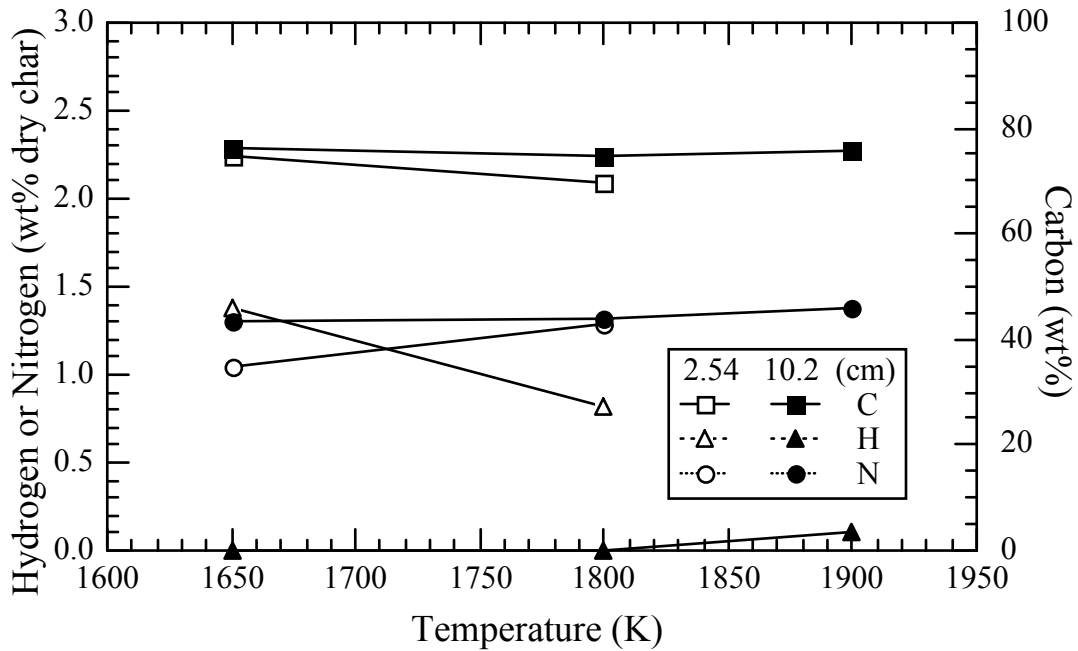


Figure 4.30. Elemental composition of the char from Illinois #6 coal.

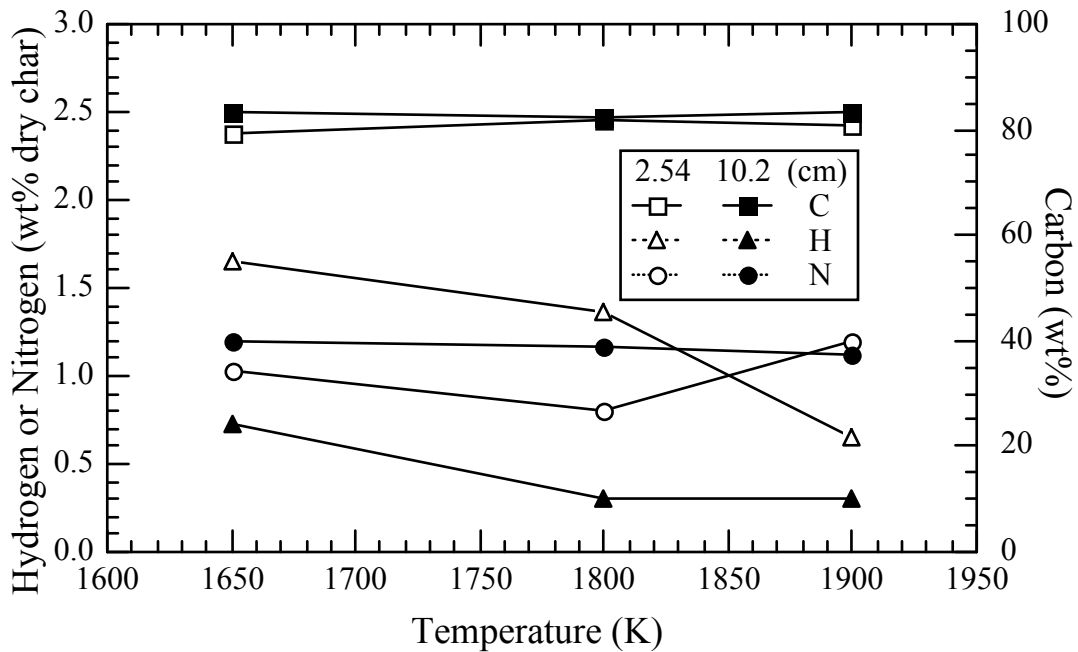


Figure 4.31. Elemental composition of the char from Dietz coal.

The compositions of carbon, hydrogen and nitrogen in the char samples for 3 coals (Pittsburgh #8, Illinois #6 and Dietz) at the lowest and highest collection heights are also plotted against the pyrolysis temperature, as shown in Figures 4.29 through 4.31. For the Illinois #6 char sample collected at 10.2 cm in the 1900 K condition, the contents of C, H and N were not analyzed. From these figures, it can be seen that hydrogen contents in all samples are related to residence time (i.e., collection height), with samples at higher residence time containing lower hydrogen. As temperature increases, the hydrogen content of the chars decreases, but the carbon and nitrogen contents remain relatively constant.

Chapter 5

PROCESS SIMULATIONS

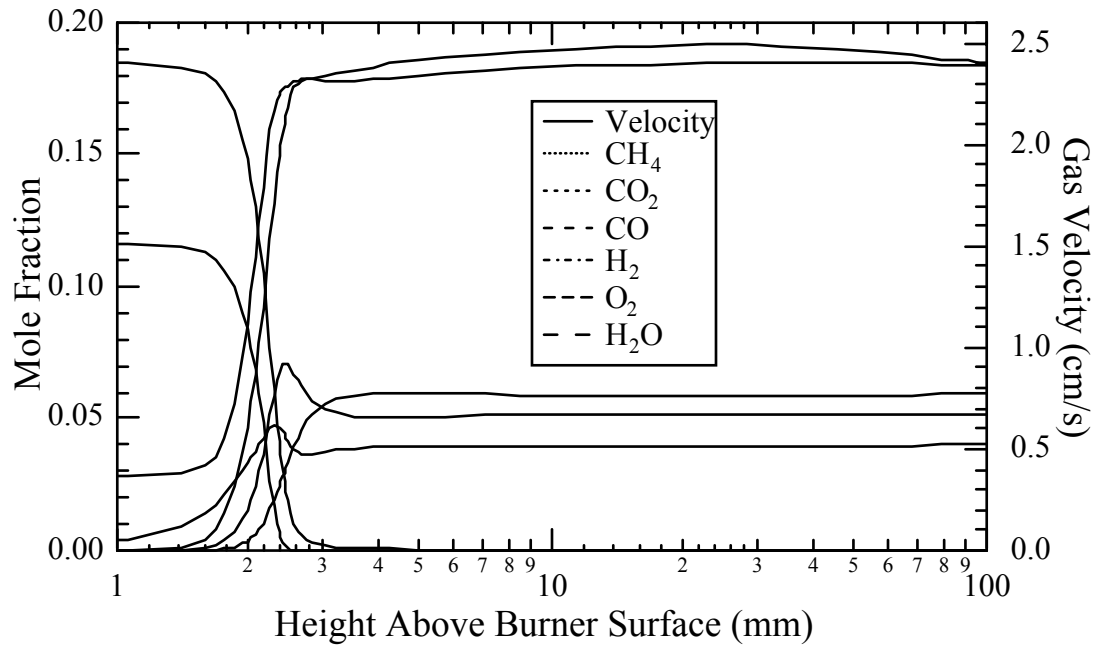
To understand the mechanisms of soot formation and agglomeration in the flame environment of this study, numerical simulations were performed of the flat flame structure, accounting for the associated processes of coal devolatilization, soot formation and agglomeration. The simulations provides valuable insight into the processes involved, as well as a basis for determining empirical kinetic parameters. These simulations are discussed below.

Flat Flame Structure

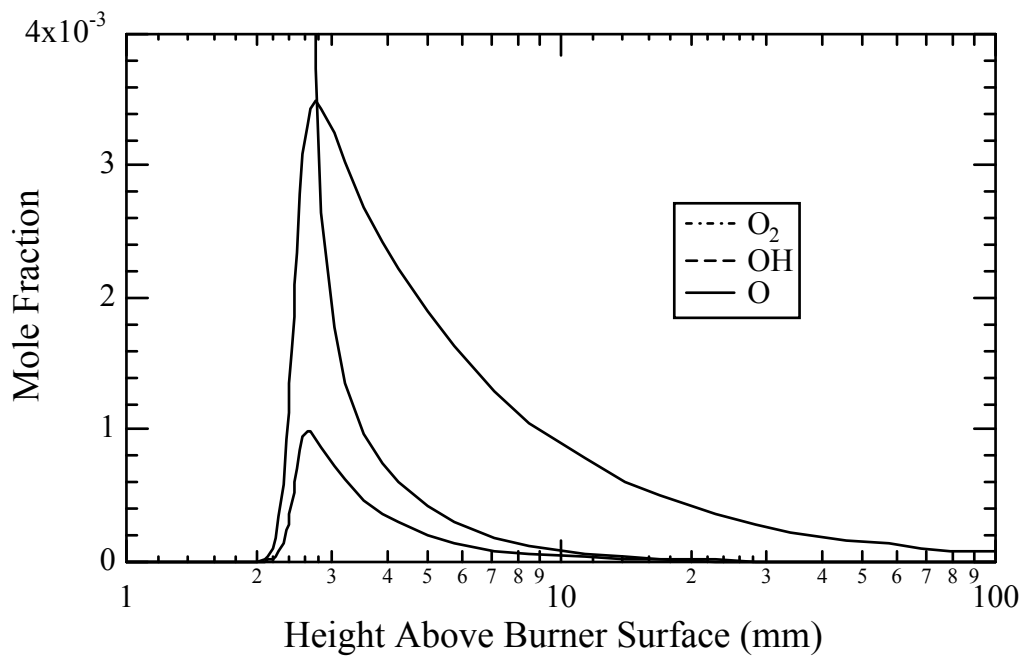
The objective of the flat flame simulations was to determine gas velocity and species concentrations in the post flame region where the coal particles were pyrolyzed. The concentrations of oxygen-containing species such as CO_2 , CO , H_2O , OH , and O_2 were of special interest, since these species have the potential to gasify or oxidize the tar and the soot. The simulation was conducted by modifying the Chemkin/Premix code developed by Sandia National Labs (Kee, et al., 1985). In this simulation, the flat flame was assumed to be a premixed flame, although in reality the flat flame consisted of dozens of tiny diffusion flames. Considering the rapid mixing nature of fuel and oxidizer on the burner surface, this should be a valid assumption. Another assumption was that the flow was one dimensional, as required by the Premix code. This assumption neglects the horizontal (“radial”) temperature and velocity distributions in the reactor. It is well known that boundary layers exist near the walls of the quartz tower, causing uneven velocity and temperature distributions. Therefore, the velocities from the simulations

must be viewed with caution. The original Premix code simulates an adiabatic flame and calculates the species concentrations based on a user-defined axial temperature profile, with temperature increasing monotonically. However, the measured axial temperatures in the flat flame reactor did not increase monotonically with height; instead they began to decrease with height due to reactor heat loss (see Fig. 3.3). The original Premix code was therefore modified to work with decreasing temperature profiles. Measured centerline temperature profiles were used as input for the Chemkin calculations, with the exception that the temperatures in the flame region were obtained through adiabatic calculations. A kinetic scheme for methane and hydrogen combustion consisting of 58 elemental steps, listed in the Chemkin manual (Kee, et al., 1985), was used for all simulations. This kinetic scheme is shown in Appendix F.

Simulations of flame structure for the three temperature conditions examined in this work are shown in Figs. 5.1 through 5.3. Simulation results are presented on with distance a logarithmic scale in order to better examine the flame region. Several trends are observed. First, the flame fronts were only 1 to 2 mm thick (based on the reactant concentration profiles), and the post-flame zone starts at $z \approx 3$ mm, which is where the coal particles were injected. Second, the velocity of the post-flame gas decreased slightly with temperature condition (from 2.5 m/s at 1900 K to 2.2 m/s at 1650 K). This trend matched the trend of measured particle velocities, i.e., longer particle residence times at the lower temperature conditions for the same collection height (see Fig. 4.2). Third, the calculated gas velocities were slightly lower than the measured centerline particle velocities because the calculated velocities neglect boundary layer effects and “radial” heat transfer. Fourth, the mole fraction of CO₂ at 1650 K was much lower than at 1900 and 1800 K, due to the higher equivalence ratio (see Table 3.1). Fifth, the peak values of the mole fractions of OH and O radicals were two orders of magnitude higher than the

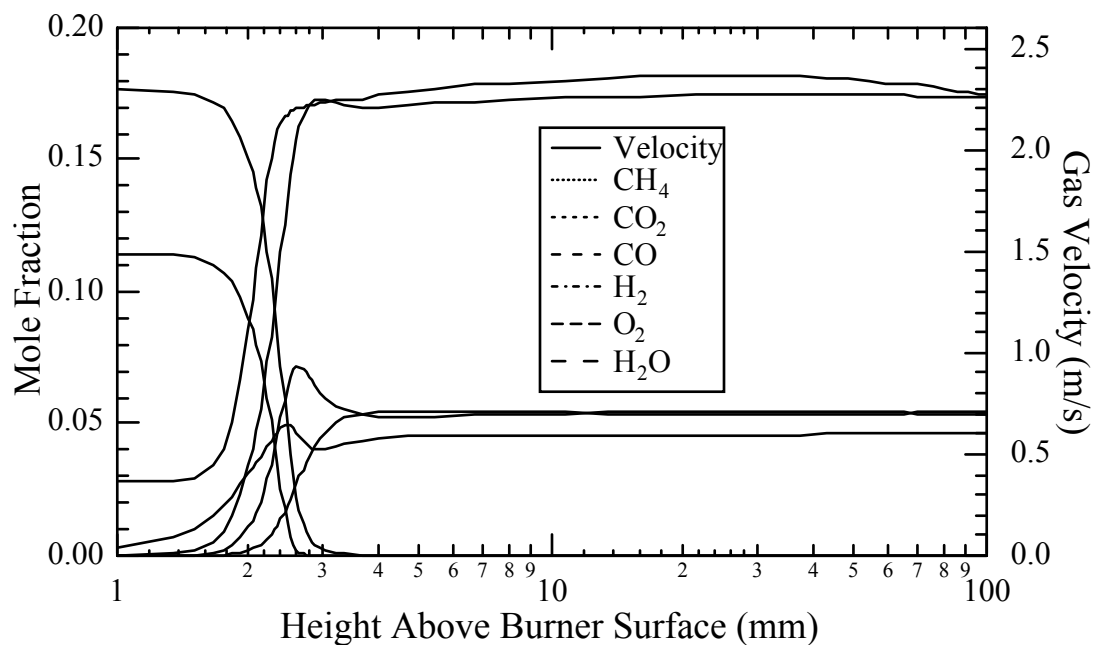


(a) molecular species and gas velocity

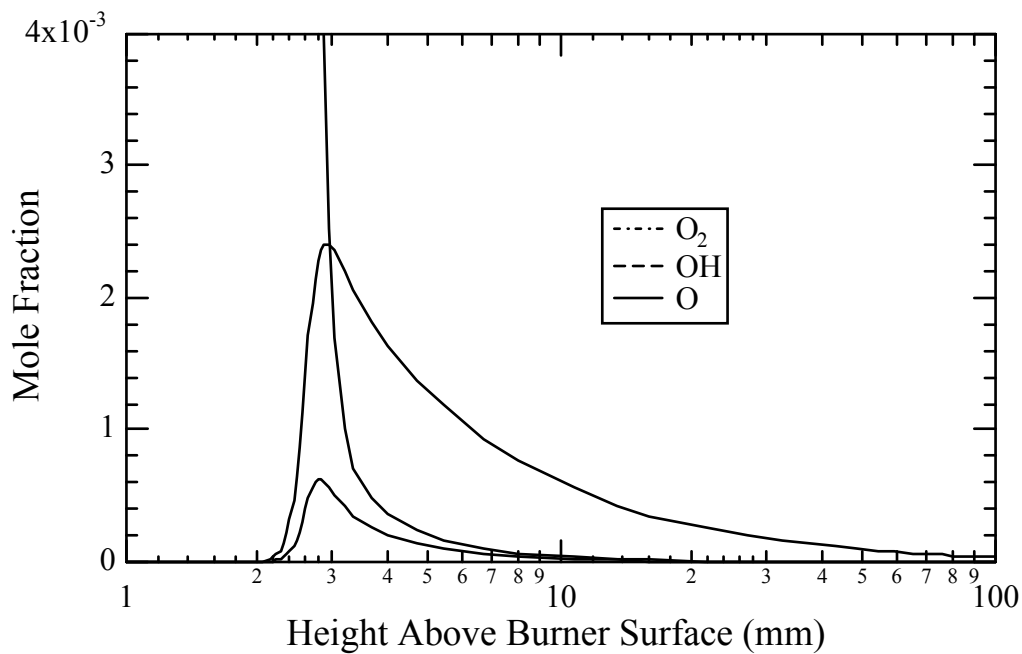


(b) major oxygen-containing species

Figure 5.1. Species mole fractions versus height at T=1900 K.

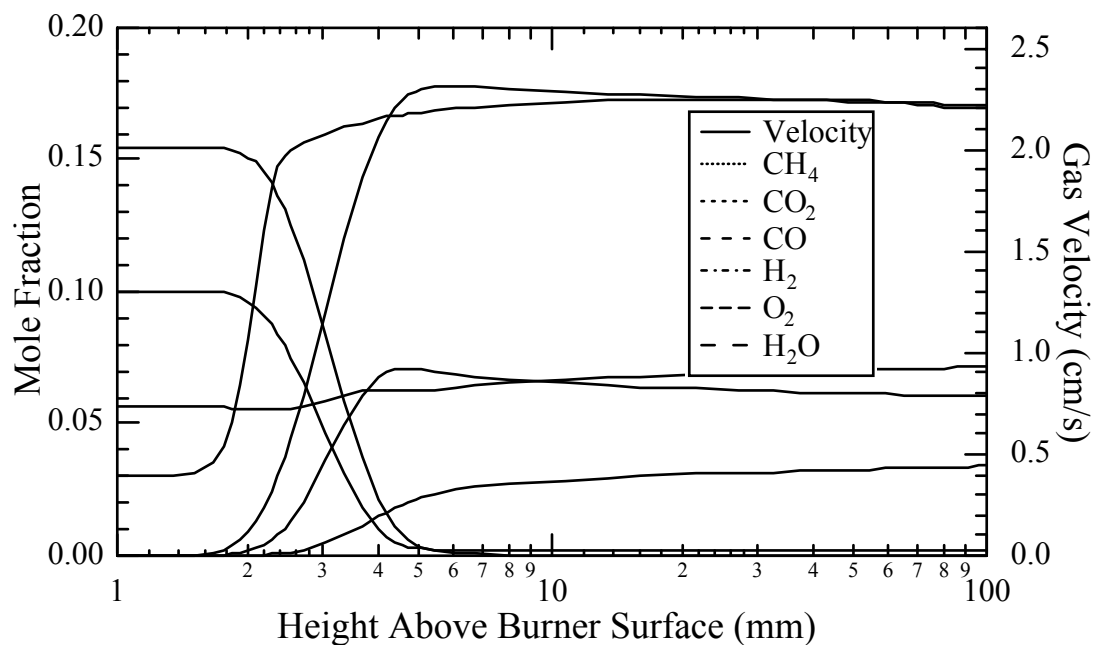


(a) molecular species and gas velocity

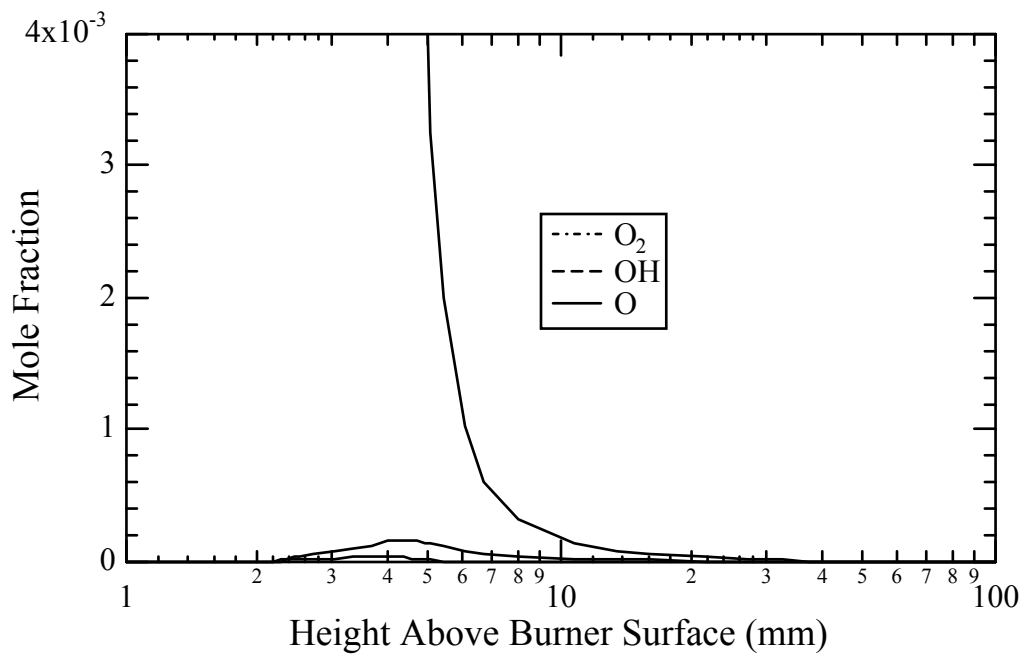


(b) major oxygen-containing species

Figure 5.2. Species mole fractions versus height at T=1800 K.



(a) molecular species gas velocity



(b) major oxygen-containing species

Figure 5.3. Species mole fractions versus height at T=1650 K.

equilibrium values, shown at large z . Finally, the peak values of mole fractions of OH and O radicals decreased by a factor of 30 when temperature condition changes from 1900 K to 1650 K.

Coal Devolatilization

Devolatilization is the initial reaction process that occurs when a coal particle is injected into the flat flame flow reactor. In the temperature conditions examined, devolatilization is completed within a very short period of time (<20 ms) due to the high particle heating rates ($\sim 10^5$ K/s). Primary devolatilization products are char, light gases and tar. Primary coal pyrolysis has been studied extensively, and can be adequately predicted by models such as the CPD model (Fletcher, et al., 1990b; 1992), FLASHCHAIN (Niksa, et al., 1991) and the FG-DVC model (Solomon, et al., 1988; 1990). The CPD (Chemical Percolation Devolatilization) model was used here to predict the generation of primary pyrolysis products. The coal-specific parameters needed for the CPD model are: (a) the fraction of intact bridge p_o ; (b) the coordination number $\sigma + 1$; (c) the average molecular weight of a cluster M_{clust} ; and (d) the average molecular weight of a side chain m_δ . These parameters can be either obtained from the solid-state ^{13}C NMR measurements on the parent coal (Fletcher, et al., 1990a) or can be predicted based on the elemental composition of the coal (Genetti, et al., 1995). The values of these parameters for the coals tested are listed in Table 5.1. One of the computer programs associated with the CPD model solves the transient particle energy equation to determine particle temperature. The program reads in a gas temperature profile, a particle velocity profile, and coal-specific parameters, and then calculates the percentage yields of tar, light gases and char as a function of residence time (Fletcher and Hardesty, 1992).

The calculated tar yields versus height in the 1900 K condition are plotted in Fig. 5.4. It can be seen from the figure that at 1900 K, tar evolution starts at 5 mm above the

flat flame and stops before the 20 mm location (or <12 ms), which is below the earliest collection point (25.4 mm). Pittsburgh #8 exhibits the highest predicted final tar yield, followed by Illinois #6, Utah Hiawatha, Dietz, Pocahontas #3 and Zap. Calculated results for the 1800 K and 1650 K conditions show similar tar evolution profiles, except that the tar evolution stops about 3 ms later at the lower temperatures. The predicted final tar yields show little sensitivity to temperature, as shown in Fig. 5.5, since all of these temperatures are above normal pyrolysis temperatures (~900 to 1000 K at 10^5 K/s). The calculated total volatiles yields versus height in the 1900 K condition are displayed in Fig. 5.6. From the figure, it can be seen that the low rank coals and high volatile bituminous coals have high total volatile yields, while the high rank coal (Pocahontas #3) has a low volatile yield. Although the tar evolution ceases below 20 mm, volatile release continues until 25 to 30 mm, due to the release of light gases. The calculations also show that total volatiles yield increases only by approximately 0.3% when the temperature is changed from 1650 K to 1900 K (see Fig. 5.7).

Based on the above observations, coal devolatilization starts at 5 to 7 mm above the flat flame (4 to 5 ms), and tar formation and total volatile release are complete before the lowest sampling location. Final tar and total volatiles yields of a coal are rank-dependent.

Table 5.1. Chemical structure parameters for six coals tested.

Coal Type	p_o	$\sigma + 1$	M_{clust}	m_δ
Pittsburgh #8 ^a	0.45	5.0	356	34
Illinois #6 ^a	0.56	4.1	270	34
Utah Hiawatha ^b	0.49	5.1	367	36
Pocahontas #3 ^c	0.59	4.0	316	23
Dietz ^b	0.52	4.9	395	41
Zap ^c	0.48	5.2	440	52

^a Data from Fletcher, et al., (1992)

^b Data predicted, using the method of Genetti, et al. (1995).

c Data from Fletcher and Hardesty (1992)

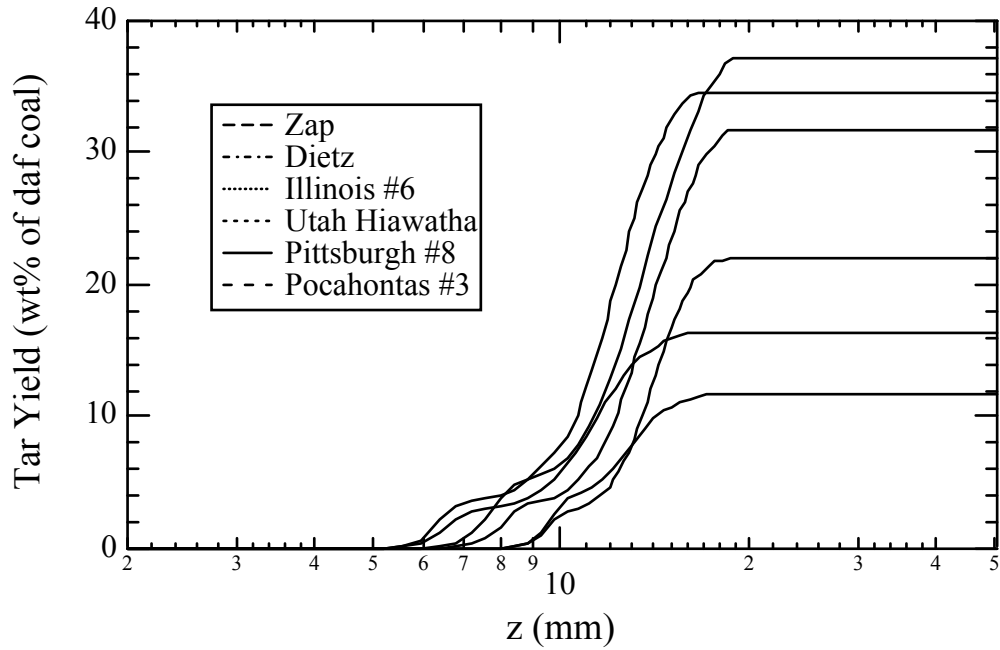


Figure 5.4. Calculated tar yields versus height in the 1900 K condition.

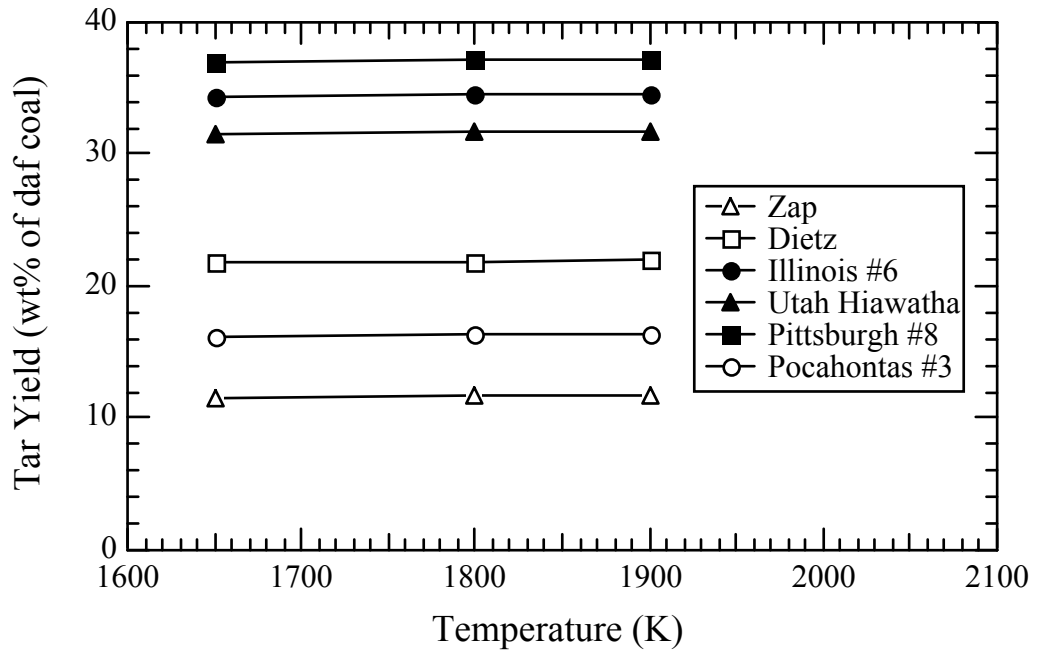


Figure 5.5. Calculated tar yields versus temperature.

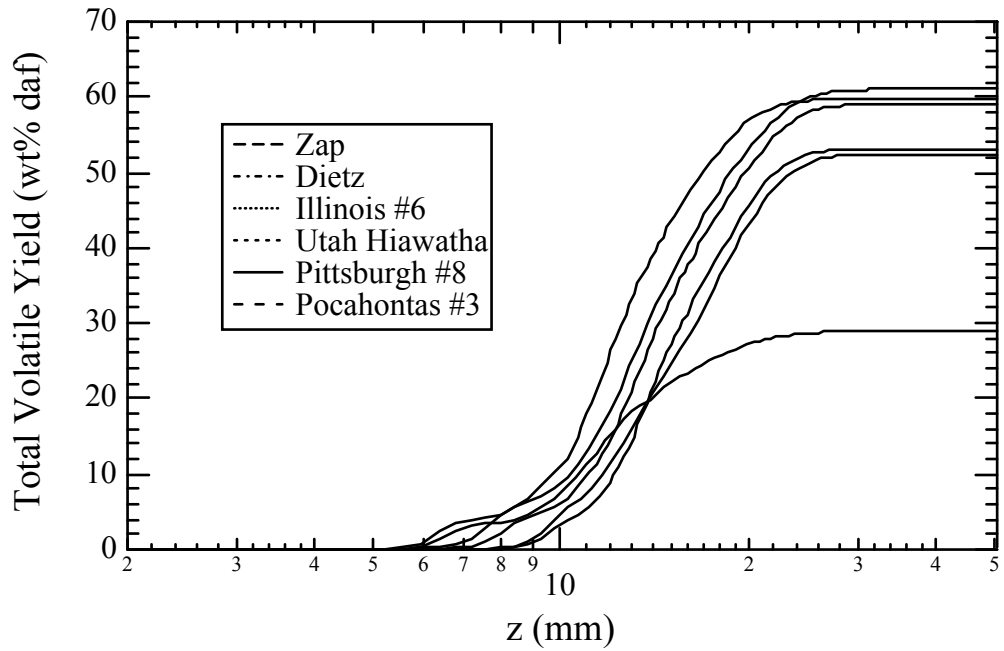


Figure 5.6. Calculated total volatile yields versus height at 1900 K.

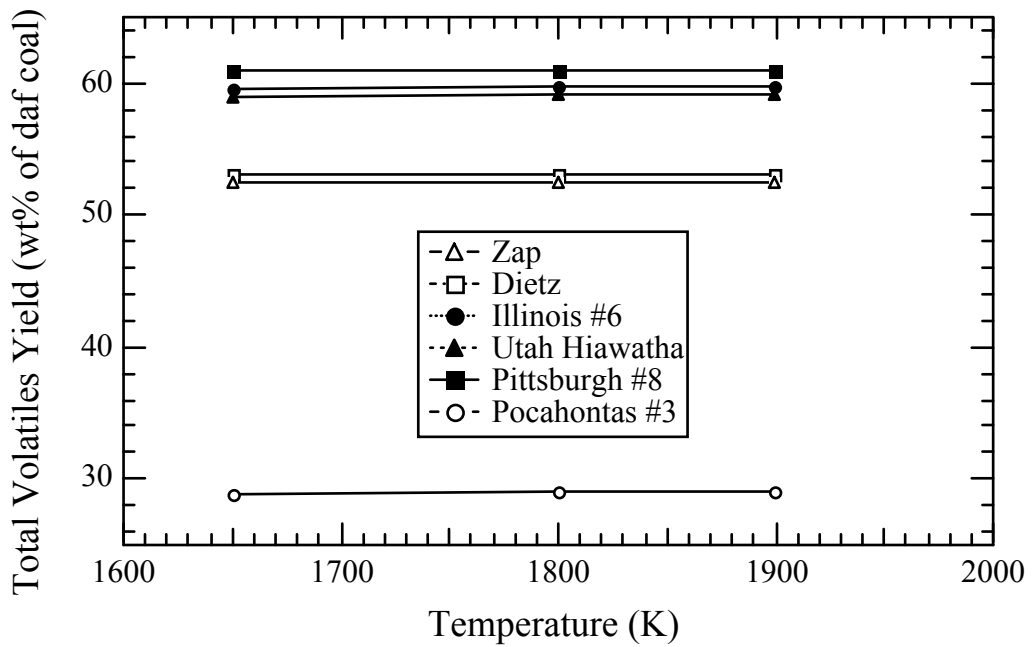


Figure 5.7. Calculated total volatiles yields versus temperature.

Soot Formation and Agglomeration

Based on the experimental results shown in Chapter 4, soot was formed in a very short period of time at the temperature conditions examined. Moreover, the soot yield versus residence time for each coal was dependent on the temperature condition. Unlike results reported on experiments in inert atmospheres, where soot yield increased monotonically with temperature, peak soot yields in this study decrease with temperature for high volatile and low volatile bituminous coals (see Fig. 4.22). This discrepancy in soot yield versus temperature can only be explained by the difference in the composition of the gases in the reactor where the secondary reactions take place. While the soot oxidation or gasification seems negligible in the experiments, tar molecules may react with molecules or radicals in the gas phase such as H_2O , CO_2 or OH . To model this effect in the soot formation processes, it was assumed that there are two competing reactions as shown in Fig. 5.8; one reaction to form soot from tar and the other reaction to gasify the tar. As discussed in Chapter 2, the soot formation process is very complicated, and usually involves hundreds of reactions. To simplify the problem, it was assumed that the transformation from tar to soot can be lumped into a first order reaction, i.e., the reaction rate is proportional to the instantaneous tar percentage available for the reaction.

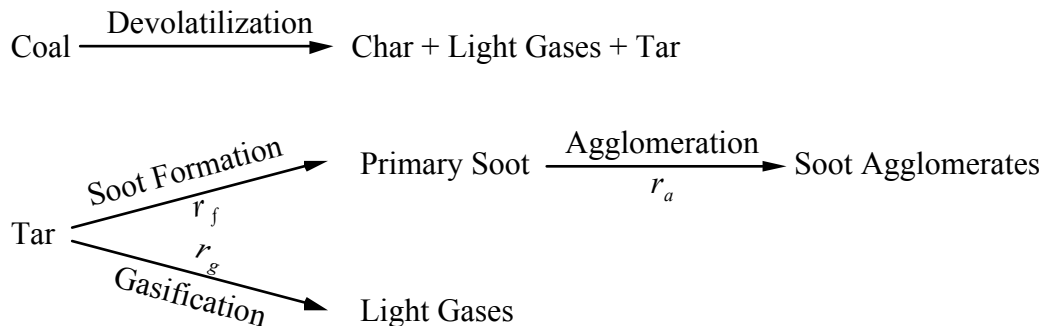


Figure 5.8. Reaction scheme used in the simulations of soot formation and agglomeration.

The tar evolution was obtained from the devolatilization calculations discussed in the previous section. The tar gasification process was also assumed to be first order with respect to the percentage of tar available.

Figure 5.8 also shows the agglomeration process after the primary soot product is formed. This agglomeration process is also very complicated; in reality, the size of agglomerates usually has a distribution. However, the thermophoretic sampling technique did not permit the collection of enough sample to measure the size distribution. In the bulk collection experiments, soot samples were categorized into two size bins: particles less than 5 μm in diameter, and particles larger than 5 μm in diameter. Accordingly, in the soot agglomeration simulation, soot particles were also divided into two groups. The primary soot was assumed to be less than 5 μm and the product of agglomeration was assumed to be larger than 5 μm . It should be mentioned that the primary soot in these simulations is not the same as the primary soot particles that constitute a chain-like agglomerate. The primary soot referred to in these simulations includes any soot particles or agglomerates that are smaller than 5 μm . The agglomeration process described in these simulations is to a certain extent an aggregation process (see Chapter 2). The agglomeration process was also assumed to be a first-order Arrhenius process. The descriptions of the rates are as follows.

$$r_f = A_f f_{tar} \exp\left(-\frac{E_f}{RT}\right) \quad (5.1)$$

$$r_g = A_g f_{tar} \exp\left(-\frac{E_g}{RT}\right) \quad (5.2)$$

$$r_a = A_a f_{sp} \exp\left(-\frac{E_a}{RT}\right) \quad (5.3)$$

$$\frac{df_{tar}}{dt} = -(r_f + r_g) \quad (5.4)$$

$$\frac{df_{sp}}{dt} = r_f - r_a \quad (5.5)$$

$$\frac{df_{sa}}{dt} = r_a \quad (5.6)$$

where E , A and f are activation energy, pre-exponential factor and dry ash-free mass fraction, respectively. Subscripts f , g , a , $tar\ sp$, sa stand for soot formation, tar gasification, soot agglomeration, tar, primary soot (<5 μm) and soot agglomerate (>5 μm), respectively.

The profile of tar mass fraction yield f_{tar}^o versus residence time or height without secondary reaction was obtained from the devolatilization calculations, as shown in Fig. 5.4. The instantaneous tar mass fraction available for the secondary reactions f_{tar} versus residence time was calculated using the equation shown below:

$$f_{tar}(t) = f_{tar}^o(t) - \int_0^t (r_f + r_g) dt \quad (5.7)$$

If the activation energies and the pre-exponential factors for the three first-order reactions are known, the yields of primary soot and soot agglomerate versus residence time can be calculated by integrating Eqs. 5.1 through 5.6. In this study, the profiles of soot yield versus residence time at different temperatures were obtained from the bulk soot collection experiments, and these profiles were used to determine the activation energies and pre-exponential factors for the kinetic scheme. The soot yield data of the Dietz coal and Zap lignite were not used because the soot samples of these two lower rank coals may be contaminated by recondensed minerals. In addition, it was assumed that the tars from the remaining four coals have the same properties with respect to the soot formation, tar gasification and soot agglomeration processes, (i.e., they have the same E and A values). The rate constants were determined by minimizing the sum-square error between the calculated soot yield value and the measured soot yield value. This minimization was performed using an optimization code called OptidesX™ (Balling, et al., 1994). The subroutine for calculating the objective function is presented in Appendix E. Figures 5.9 through 5.12 show the comparisons between the calculated soot yields (using the optimized kinetic coefficients) and the experimental data. Table 5.2 shows the values of kinetic coefficients obtained through the optimization procedure.

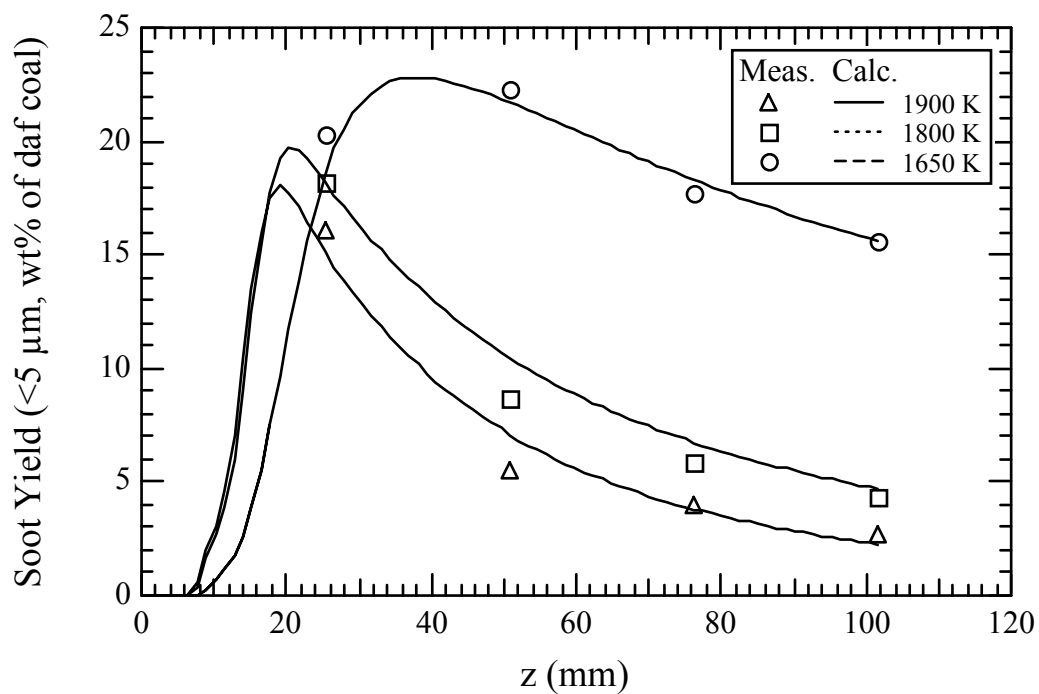


Figure 5.9. Calculated soot yield profiles for Pittsburgh #8 coal using the optimized kinetic coefficients in Table 5.2.

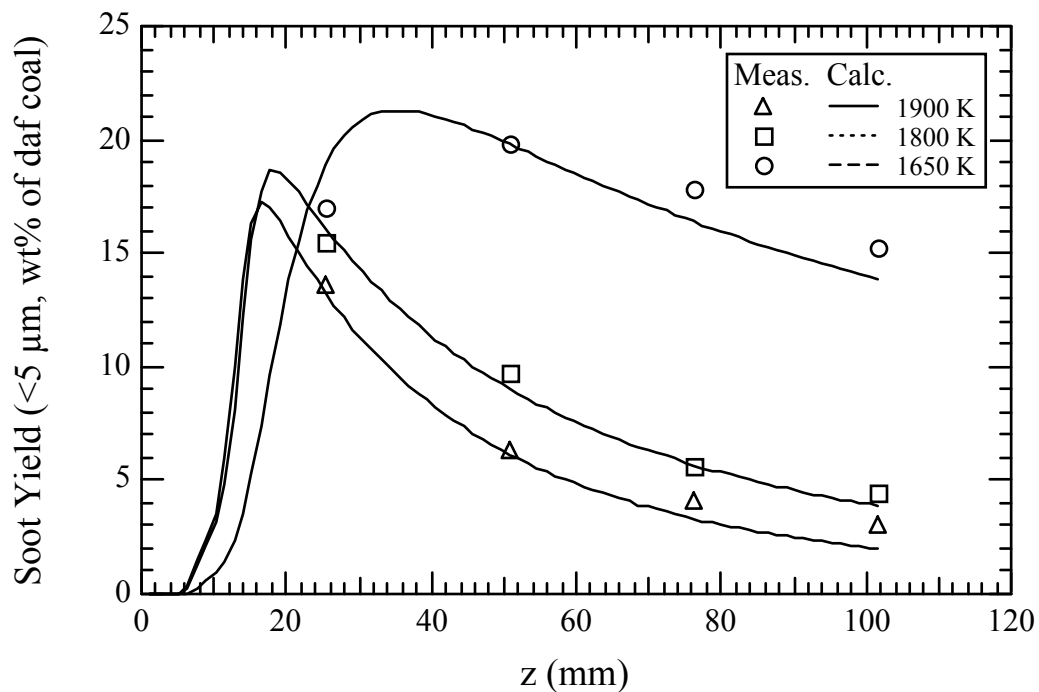


Figure 5.10. Calculated soot yield profiles for Illinois #6 coal using the optimized kinetic coefficients in Table 5.2.

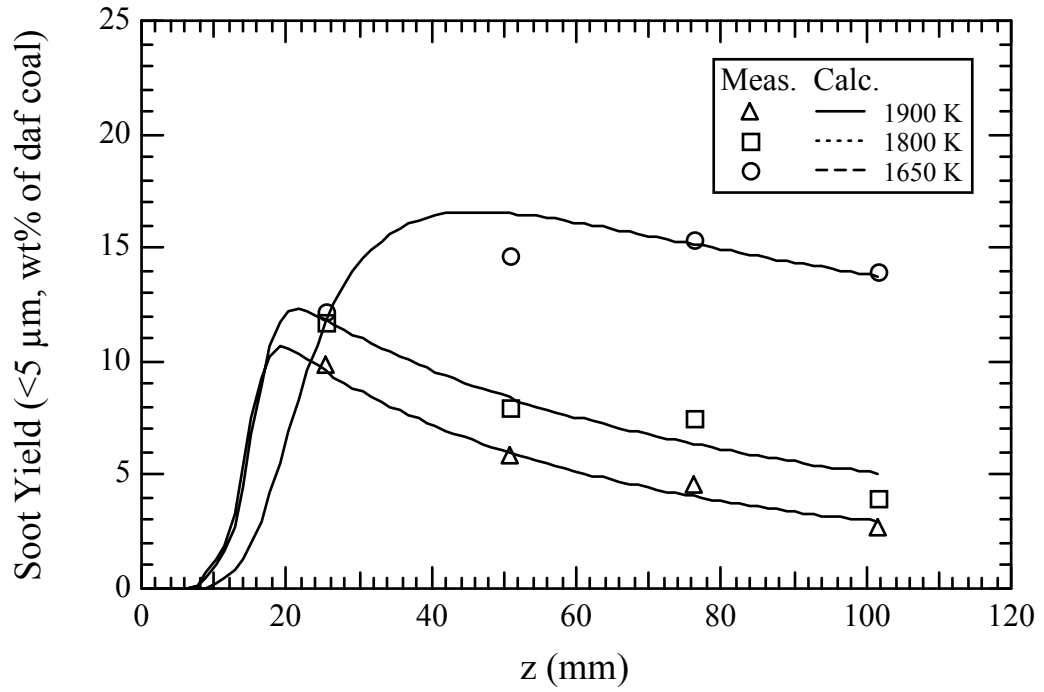


Figure 5.11. Calculated soot yield profiles for Utah Hiawatha coal using the optimized kinetic coefficients in Table 5.2.

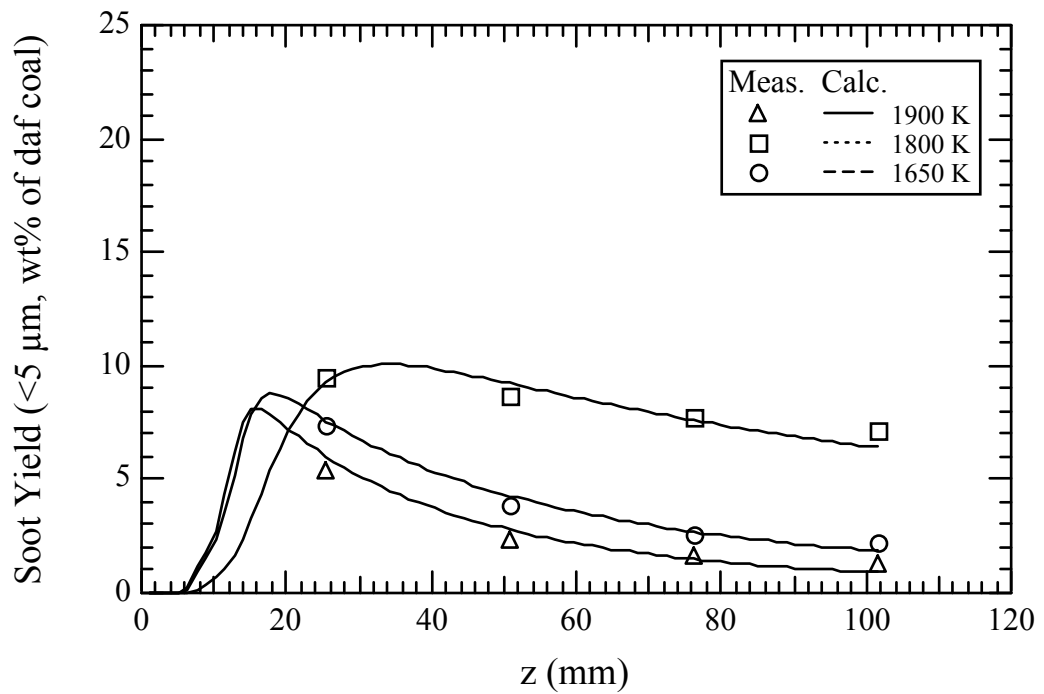


Figure 5.12. Calculated soot yield profiles for Pocahontas #3 coal using the optimized kinetic coefficients in Table 5.2.

Table 5.2. Optimized activation energies and pre-exponential factors.

Soot Formation	E_f (kJ/mol)	198.9
	A_f (1/s)	5.02×10^8
Tar Gasification	E_g (kJ/mol)	286.9
	A_g (1/s)	9.77×10^{10}
Soot Agglomeration	E_a (kJ/mol)	129.9
	A_a (1/s)	3.10×10^5

From these figures, it can be seen that good agreement between experimental data and calculated soot yield values was achieved by using coal-independent activation energies and pre-exponential factors. The good agreement also indicates that the tar yield as a function of particle residence time predicted by the CPD model represents the adequately the coal devolatilization process. The obtained activation energies for soot formation and agglomeration are lower than activation energies for coal devolatilization (from 232 kJ/mol to 288 kJ/mol; Fletcher, et al., 1990b), which means that soot formation and agglomeration are rapid processes compared to devolatilization.

Chapter 6

DISCUSSION OF RESULTS

Thermophoretic Soot Sampling

Both tar and soot yields in drop tube pyrolysis experiments have been found to be functions of pyrolysis temperature, particle residence time, and coal type (Chen, 1992c; Wornat, et al., 1987, 1988a; Nenniger, 1986). This is also true for coal pyrolysis experiments conducted in the post-flame environment in this study (Ma, et al., 1995b). When sampling close to the burner (low particle residence times), coal particles are still heating up, and may still be at a low enough temperature to exhibit low yields of tar and soot. A correlation between the size and number of soot deposits and the residence time for this reactor has not been determined. Even though all three coals examined are high volatile bituminous coals, the compositions of volatiles released during pyrolysis may be different. Apparent differences in sooting tendencies of pure hydrocarbons depend on chemical structures (Olson and Pickens, 1984, 1985), and therefore, the composition of the evolved coal tar likely relates to sooting tendency.

The droplet-like evaporating deposits observed on the TEM grid are thought to be tar at some stage of secondary reaction. Tar formed during coal pyrolysis can often be extracted chemically from aerosol samples collected by suction probes (Chen, 1992c; Wornat, et al., 1987, 1988a; Nenniger, 1986). Primary tar forms rapidly based on the devolatilization simulations and is thought to react quickly in the high temperatures in the present experiment. Therefore, the evaporating deposits are thought to be reacted tar (i.e., polycyclic aromatic hydrocarbons, or PAH) that are not yet as thermally stable as soot. For simplicity, these droplets on the TEM grids will be referred to as tar (which is

presumed to be at some stage of evolution to PAH). The presence of the tar on the TEM grid can be explained as follows. In the absence of a volatiles flame surrounding individual particles, tar and small soot particles are free to expand radially away from the particle surface. As a cold sampling grid (around 100 °C) is inserted into the soot cloud in this pyrolysis experiment, the soot particles and agglomerates thermophoretically deposit on the grid. At the same time, because the temperature of the grid is below the dew point of the tar vapor (or the boiling point of the tar), the tar will also condense on the grid surface. The boiling material seen under the electron microscope is the condensed tar. Because of the high vacuum within the microscope and the heating under the high-energy electron beams, the condensed tar undergoes reactions, and the low molecular weight material is vaporized.

The copper bars that form the grid have higher heat capacity than the carbon film. Therefore, particles and tar are both more likely to deposit near the copper bars. If the grid is passed through a region where both soot and tar are present, a tar droplet may condense on top of a soot particle (or vice versa), and hence soot particles are observed "inside" tar droplets. It is also possible that a portion of a tar molecule has become attached to soot particles in the reactor, and is in the process of coagulation or growth when the sample is taken.

Unstable liquid-like deposits were not seen in the thermophoretic samples from the butane flame. No report of "boiling" phenomena on TEM grids have been reported previously. This suggests that the concentration of high molecular weight hydrocarbon molecules (similar to coal tar) should be very low in the simple hydrocarbon flames. One proposed principal pathway for soot formation in hydrocarbon flames is the addition of small molecules to the soot nuclei (Howard, 1990). It has been suggested that large tar molecules add to soot nuclei directly in coal combustion flames, rather than breaking up into small molecules such as acetylene, followed by addition of these small molecules to

soot nuclei (Wornat, et al., 1988b). The presence of evaporating deposits in the coal experiments (but not in the butane experiments) is consistent with this hypothesis.

The flat-flame burner experiment described here, where coal pyrolyzes in an oxygen-free environment, is thought to be representative of the pyrolysis environment in large-scale pulverized coal furnaces. In these large-scale systems, the particle loading is high enough to prevent oxygen from penetrating very far into the volatiles cloud. A turbulent diffusion flame exists at the edges of the volatiles cloud where the oxygen is totally reacted. Inside the diffusion flame, since no oxygen is present, it is not possible to have individual flames surrounding individual particles. However, post-flame gases (such as H₂O and CO₂) and oxygen-containing radicals (such as OH) are thought to be present in the volatiles cloud, since product recirculation is essential to many burner stabilization schemes. The flat flame burner experiments are therefore an attempt to reproduce the gas environment in a volatiles cloud, and differ from previously-reported experiments conducted in pure argon. However, due to the high temperatures and existence of such oxygenated species (H₂O, CO₂, OH, etc.), it is possible that the tar, soot, and/or char may be partially gasified during these experiments (Ma, et al., 1995b). This may also happen in volatiles clouds in large pulverized coal furnaces. Therefore, the soot particles generated in the present experiments are thought to be representative of the size and composition of soot particles generated in large-scale furnaces.

It is interesting to contrast the results presented here with results obtained in the post-flame region of a CH₄/H₂/O₂/N₂ flat flame burner where post-flame O₂ was present. Using high magnification shadowgraphs and high-speed cinematography, McLean, et al. (1981) observed that volatile matter undergoes polymerization reactions to form a soot-like condensed cloud around single combusting coal particles, as illustrated in Fig. 6.1. McLean's experiments were conducted in a flat flame methane-air reactor with 8% post-flame oxygen. They suggested that the condensed cloud consisted of small soot particles called soot nuclei. Primary soot particles are much smaller than coal or char particles,

and therefore travel at the gas velocity rather than the particle velocity, as does the tar cloud. Soot nuclei undergo surface growth as surrounding organic matter adheres to the soot surfaces. In McLean's experiment, the soot particles impacted each other in the vicinity of the coal particle and coalesced to form agglomerates, which were generally in the form of long rod-like structures. As soot traveled around the coal particle in the Stokes flow regime, soot particles formed agglomerates in the form of streamers. These rods or "tails" were observed by McLean and coworkers to be as long as 500 μm , but only about 40 μm in diameter. The average initial coal particle diameter in McLean's experiments was 65 μm . The initial soot particles formed did not escape the vicinity of the particle during devolatilization due to the surrounding volatiles flame. The temperature gradient between the flame and the coal particle surface is a thermophoretic driving force that pushes soot particles back towards the surface. Also, soot particles that travel through the flame are oxidized. Therefore, in the single particle coal combustion experiments (with O_2 present) examined by both McLean, et al. (1981) and Seeker, et al. (1981), most of the soot is observed in large agglomerates in the form of streamers.

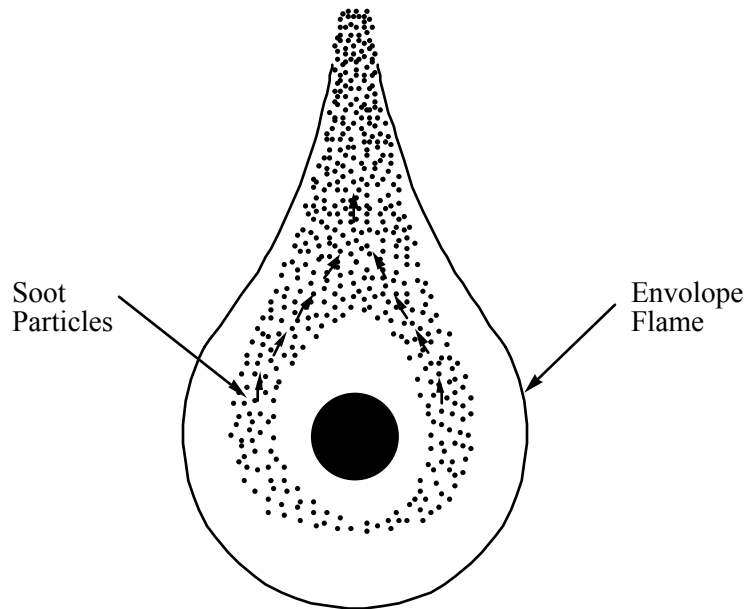


Figure 6.1. Formation of soot streamer around a coal particle in oxygen-rich environment.

In the experiments presented here, the coal pyrolyzes in an oxygen-free environment, and hence there is no volatiles flame surrounding individual particles. It might be possible that oxygen-containing species react with the tar, and the resulting exothermic reactions raise the temperature near the volatile envelope. The phase change associated with gas release and tar evolution creates a convective velocity (Stefan flow) away from the particle, and the tar continues to spread radially away from the char particle surface. The observed radial spread of the soot cloud when no O₂ is present (see Fig. 3.2) indicates that soot leaves the vicinity of the coal particle. In the absence of a volatiles flame surrounding individual particles, the thermophoretic driving force on the soot particles formed from the tar is much smaller, and the soot particles do not remain in the vicinity of the char particle. Therefore, the large agglomerates observed by McLean, et al. (1981), with a size of 500 μm, were not observed.

Bulk Soot Sampling Experiments

Volatiles Yield

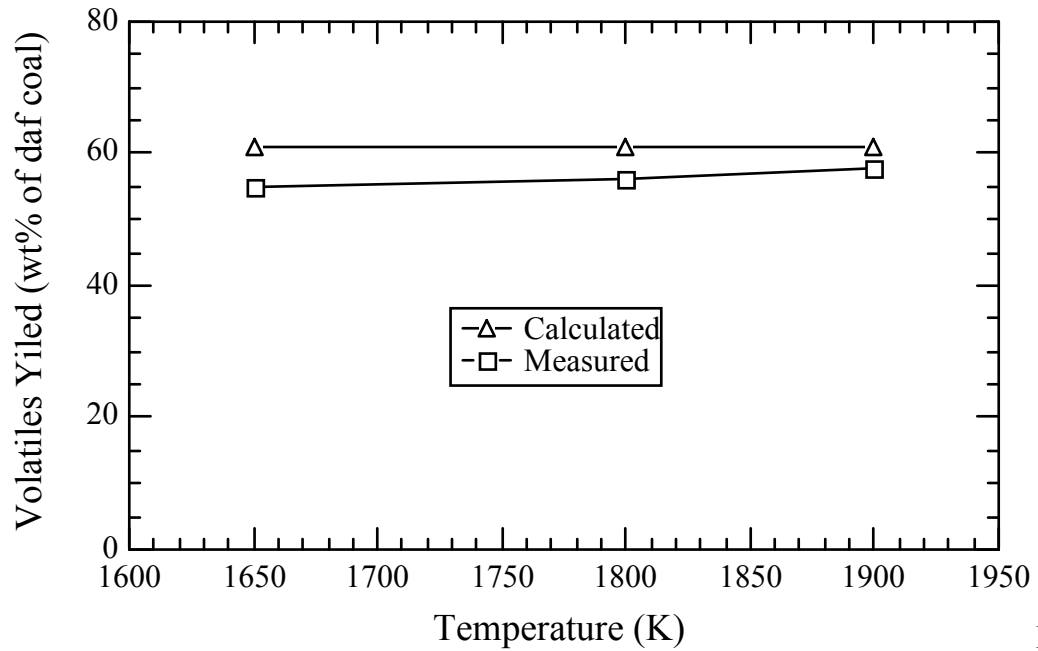
Based on the result shown in Figs. 4.15 through 4.20, volatiles yields for the three high volatile bituminous coals and the Pocahontas #3 low volatile bituminous coal are almost constant with respect to particle residence times when the residence time is larger than 15 ms, while volatiles yields of the two low rank coals show a trend of increasing volatiles yield with residence time. The constant volatiles yield for the higher rank coals means that even in the conditions of high temperatures and post-flame gases, char particles are not reactive with gas phase species, and that no volatiles will be released after 15 ms. The increases in volatiles yield versus residence time for the low rank coals may be due to the vaporization of mineral matter existing in the parent coals, since the devolatilization simulations show that the devolatilization process ceases within 15 ms

(see Fig. 5.6). Based on the devolatilization simulations shown in Figs. 5.4 and 5.6, tar release stops earlier than the volatile release, which means that the functional groups in the side chains continue to disconnect from the coal matrix to form light gases, even after tar formation and evolution cease. Moreover, temperature usually has some effect on total volatiles yield in low-temperature coal pyrolysis. Higher gas temperature and higher heating rate usually results in higher tar yield and higher volatiles yield. At such high temperatures as were used in this study, the effect of temperature on volatiles yield should be less significant. The devolatilization simulations showed that total volatiles yield increased slightly with temperature for each coal tested (see Fig. 5.7). Higher volatiles yields were also obtained experimentally at the higher temperature conditions. The trend of measured volatiles yield versus temperature agrees with the calculated volatiles yields as shown in Fig. 6.2. The measured volatiles yields in Fig. 6.2 are the average values from 4 different residence times, and the calculated volatiles yields are the asymptotic values. Figure 6.3 shows a comparison between the measured volatiles yields and the volatiles yields calculated with the CPD code as a function of coal rank (the C% is used as a indication of coal rank). The measured volatiles yields shown in Fig. 6.3 are averages from the 1900 K condition. Overall, the data follow the trend that low rank lignite and high volatile bituminous coal exhibit high volatiles yields, whereas the low volatile bituminous coal exhibits a low volatiles yield. The calculated volatiles yields agree well with the measured volatiles yields for the high rank coals, including both the high and low volatile bituminous coals. However, the measured volatiles yields for the low rank coals are larger than the calculated volatiles yields. This discrepancy for the low rank coals may be due in part to vaporization of mineral matter, such as Na and Ca.

Total Soot Yield

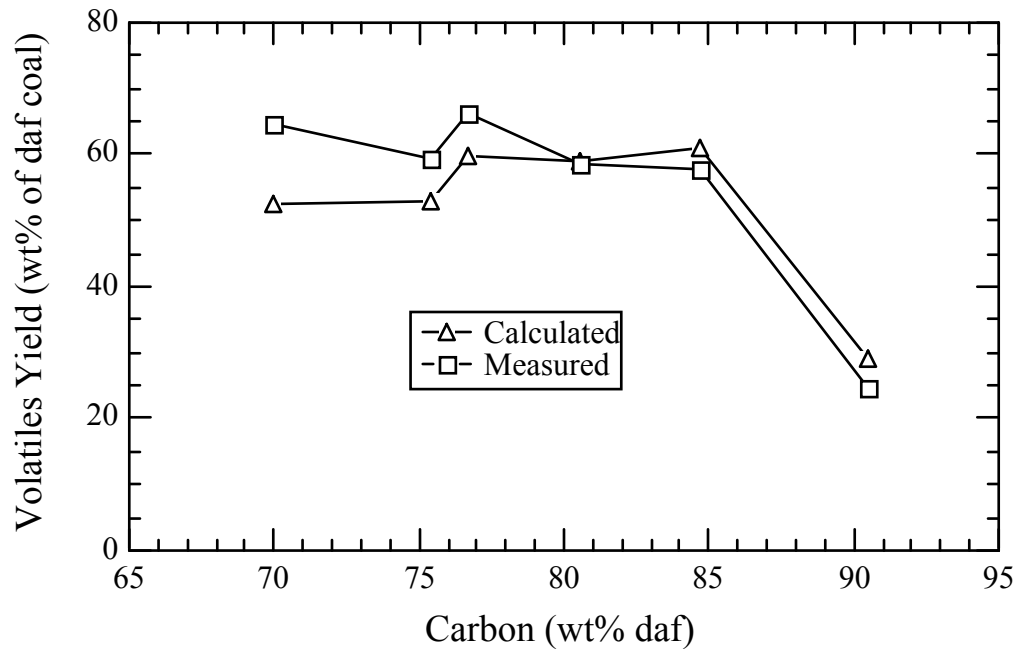
Tar is believed to be the precursor of coal-derived soot, as suggested by many researchers (McLean, et al., 1981; Nenniger, 1986; Wornat, et al., 1987; Chen, 1991).

Consequently, a coal with a high tar yield should also have a high soot yield when it is



Figure

6.2. Measured and calculated volatiles yields versus temperature for the Pittsburgh #8 coal.



Figure

6.3. Measured and calculated volatiles yields versus coal rank in the 1900 K condition.

exposed to a secondary pyrolysis environment. For the six coals used in this study, the rank, in order of decreasing tar yield calculated using the CPD model, is: Pittsburgh #8, Illinois #6, Utah Hiawatha, Dietz, Pocahontas #3 and Zap. The measured total soot yields are also in this order (see Figs. 4.15 through 4.20). Other investigators have shown that in inert environments, the yield of soot plus tar remains constant. It is therefore reasonable to compare the soot yields measured here to the tar yields reported in the literature. A comparison between soot yields measured in this study and reported tar yields (Freihaut, et al., 1989) is illustrated in Fig. 6.4. In this figure, the percentage tar and soot yields for different coals are plotted against the carbon percentage in the parent coals, which is an indicator of coal rank. High volatile bituminous coals have both high tar and soot yields, as can be seen in this figure. Note that two sets of tar yield data were reported by Freihaut and coworkers; one from heated-grid experiments and the other from entrained flow experiments. The heating rates in the heated grid experiments

are approximately 1000 K/s and the heating rates in the entrained flow experiments are on the order of 10^4 K/s. Both coal pyrolysis methods used by Freihaut should result in lower primary tar yields than the method used in this study because of their lower heating rates relative to this study. However, the trend of soot or tar yield versus coal rank can still be seen. The fact that the soot yields in this study are lower than the tar yields observed by Freihaut suggest a certain degree of tar gasification in the post-flame gases of the reactor environment.

The total soot yields measured in this experiment were comparable with soot yields obtained in inert pyrolysis conditions (Nenniger, 1986; Wornat, et al., 1987; Chen, 1991), although Chen's maximum soot yield was higher than all of the other data. A comparison of soot yields from several Pittsburgh high volatile bituminous coals is presented in Fig. 6.5. The Pittsburgh coals used by other researchers were not exactly the same as the Pittsburgh coal used in this research in terms of size cuts and seam locations,

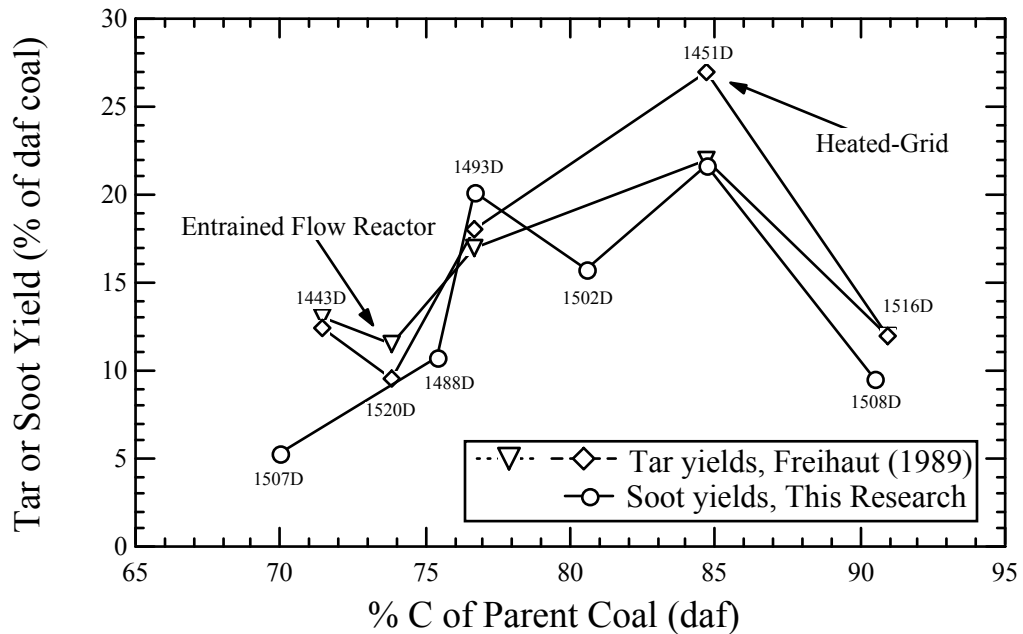
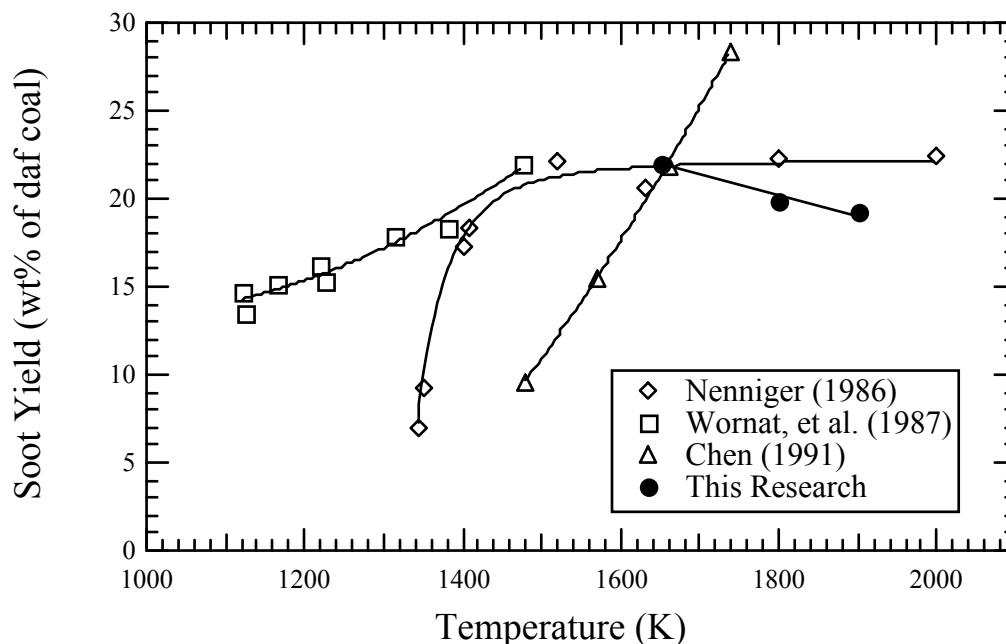


Figure 6.4. Comparison of soot yield with tar yield for several coals.

but should be very close in composition. Nenniger and Wornat used a Pittsburgh Seam high volatile bituminous coal (PSOC 997) with size ranging from 44 to 53 μm . Chen used the same coal type as this study (PSOC 1451D), but used the size fraction from 75 to 106 μm . The temperatures shown in Fig. 6.4 for Chen's data are actually the reactor wall temperature, which are several hundred degrees higher than the actual particle temperatures. Nenniger's data show that an asymptotic value was reached at increased temperatures, while Wornat's and Chen's data do not show a limit. The data obtained by Nenniger, Wornat and Chen all show that soot yield increases or remains constant with temperature. One interesting result of the current research is that the total soot yield decreased with increases in temperature. This result is different from the result in inert coal pyrolysis experiments, but is comparable with the results obtained in the hydrocarbon flame experiments or hydrocarbon pyrolysis experiments (Frenklach, et al., 1986). The soot yield in the hydrocarbon experiments always shows a bell-shaped profile when plotted against temperature. In the current coal pyrolysis study, the soot yield data are apparently on the right side of the bell-shaped curve, which means that soot yields at 1650 K may be close to the peak yield. If the pyrolysis temperature is reduced, as in lower temperature pyrolysis experiments, the soot yield will also be reduced. Of course, if the temperature is too low (<900 K), no secondary reactions will take place (Serio, 1987) and the soot yield will be zero. Therefore, even though the soot yield versus temperature curve in this research shows a decreasing trend, the entire soot yield curve should still be bell-shaped if low temperature effects are considered. This can be seen by combining Wornat's soot yield profile in Fig. 6.5 with the profile of this research.



- Notes: 1. Data reported by Nenniger, Wornat, et al. and Chen were obtained in an inert atmosphere (Ar).
2. Temperatures reported by Chen were wall temperatures of the reactor. Particle temperatures were several hundred degrees lower.

Figure 6.5. Comparison of soot yield versus temperature.

The decrease in soot yield with temperature can be explained by the stability of tar molecules at high temperatures and the reactions of tar by gaseous species existing in the post-flame region of the flat flame reactor. As discussed in the literature review section, polymerization and PAH cracking are competitive reactions in the soot formation processes, and the stability of the high molecular PAH tends to decrease with temperature. On the high temperature side of the bell-shaped soot yield curve, increases in temperature favor the cracking reaction, which leads to a lower soot yield. Another reason for the low soot yield at high temperature might be the reactions of the oxygen-containing species, especially OH and O radicals, with tar molecules and intermediate PAH. The concentrations of oxygen-containing radicals such as OH and O increases drastically with increases in temperature, as calculated by the modified Chemkin Code

(see Figs. 5.1 through 5.3). Because of the increased attack of PAH molecules by these radicals, the stability of PAH is reduced further. This could explain why the soot yields obtained in inert atmospheres were higher than the yields obtained in the post-flame gas environment in this study.

It is also interesting to compare the temperature at the peak soot yield in this study (~1650 K) with those for simple hydrocarbons. From Fig. 2.1, it can be seen that the peak soot yield temperatures for benzene and butadiene are around 1950 K and 2050 K respectively. Based on the current research, the peak of the soot yield curve for coal-derived soot seems to occur at a lower temperature than benzene and butadiene. Therefore, it appears that lower temperatures favor the formation of soot from coal-derived high-molecular-weight tar. One explanation of this temperature difference is that tar molecules form soot through a different mechanism. It is very possible that tar molecules can be polymerized directly to soot, with only a minor amount of tar cracking to small hydrocarbons (such as acetylene) at a relatively low temperature. High molecular weight PAH are believed to be the precursor or intermediate species in the process of soot formation. In the case of coal pyrolysis, these intermediate PAH already exist and are ready to undergo condensation or polymerization. In the case of benzene or butadiene pyrolysis, for example, large PAH molecules need to be formed first in order to generate soot, which requires a relatively high temperature. Butadiene requires an even higher temperature than benzene to form soot because there is even no aromatic ring before the reaction. Another possible reason for the lower peak yield temperature for coal-derived soot in this study is that concentrations of oxygen-containing radicals are very sensitive to temperature. At a high temperature, the attack of tar molecules or intermediate PAH by these oxygen-containing radicals will be very severe, which causes the shift of the peak towards a lower temperature.

Soot Agglomeration or Aggregation

Soot formation is always followed by soot agglomeration, as discussed in Chapter 2. Most soot agglomerate structures reported in the literature consist of 10 to 100 primary particles (Jagoda, et al., 1980; Megaridis and Dobbins, 1989; Saito, et al., 1991), i.e., the size of an agglomerate or aggregate is limited. However, in special situations such as at microgravity (Ito, et al., 1994; Jackson, et al., 1992), primary particles are formed in a limited region of a flame or a reactor and are not able to leave that region. As a result, soot agglomerates or aggregates as large as 0.5 mm can be formed. The reason that these big agglomerates are seldom found in most simple diffusion or premixed flames at normal gravity is that free convection provides a mechanism for soot particles to disperse and leave the region in which they are generated.

In this study, larger agglomerates were observed at higher residence times, as discussed in the previous chapters. It is possible that these large agglomerates could be formed in the suction probe and separation system (virtual impactor and cyclone). While this hypothesis can not be conclusively eliminated, the residence time did have effect on agglomeration (i.e., at the lowest residence time, no large agglomerates were observed). Since the collection system did not cause soot particles to form large agglomerates at the lowest residence time, the agglomeration phenomena can not be ascribed only to alteration by the collection system. Based on the trends of total soot yield profile and small soot ($<5 \mu\text{m}$) yield profile, agglomeration appeared to occur before sample collection. However, the mechanism of formation of the large agglomerates is still unclear. One possible explanation is that the tar or soot particles that remain in the vicinity of a coal particle grow due to thermophoretic forces or other mechanisms. In an oxygen-rich environment, a volatile flame around a coal particle exists and large soot-like particles form in the wake of the coal particles (as reported by McLean, et al., 1981). In the oxygen-free environment of this study, the reactions between the tar and the oxygen-containing radicals may still form some type of flame even though some agglomerates escape the vicinity of the coal particles. Another explanation is that upon

heatup, tar ejects from a coal particle in form of volatile jets as described by Seeker, et al. (1981), and these tar jets are entrapped by the hot gases. Soot forms inside the jet and tends to agglomerate in the limited jet volume, given sufficient residence time. If soot and char samples are collected at a lower residence time, the turbulence at the tip of the collection probe can break the small entrapped volumes and therefore stop the soot agglomeration. The jet-like release of coal volatile should be enhanced at high temperature pyrolysis, which may lead to a high yield of large soot agglomerates as being observed in this study (see Figs. 4.15 through 4.20 and Fig. 4.23). At a lower temperature, tar release is distributed more evenly around the surface of a coal particle, and the formation of large soot agglomerate is limited.

In the thermophoretic sampling experiments, the largest soot agglomerate collected was around 800 nm. The large agglomerates ($> 5 \mu\text{m}$) found in the bulk collection experiments are too large to be collected thermophoretically. However, the size of primary particles in these large agglomerates collected in this study is very comparable to the size of primary particles in the soot agglomerates obtained by thermophoretic sampling. The presence of large agglomerates explains why no clear trend in the soot particle size was observed as a function of either coal type or residence time in the thermophoretic sampling experiments.

Elemental Composition of Products

Based on Figs. 4.24 through 4.28, the elemental composition (i.e., carbon, hydrogen and nitrogen) in soot samples obtained at high temperatures (1800 K and 1900 K) do not show dependence on collection height or residence time. The corresponding C/H mole ratios for these samples are in the neighborhood of 10, which is close to the value reported for mature soot from simple hydrocarbon flames (Haynes, 1991). This suggests that the soot particles collected at the 2.54 cm above the flat flame (~15 ms) were mature particles in these conditions and that the dehydrogenation process happened

before 15 ms. On the other hand, in the 1650 K temperature condition, the hydrogen contents decreased with the increase in residence time (C/H ratio increased approximately from 5 at 15 ms to 10 at 45 ms), which means that the dehydrogenation continued after 15 ms and the soot became mature at the high residence time (~45 ms). The result in the 1650 K condition is comparable to the result reported by Chen (1991). In Chen's coal pyrolysis experiments (in argon at a particle temperature lower than 1650 K), the C/H mole ratio of soot increased from 2 to 10 when the reactor wall temperature was raised from 1480 K to 1750 K.

No clear dependence of the nitrogen content of soot samples on residence time or temperature was observed in Figs 4.24 through 4.28. The scatter in the data shown in these figures is probably due to experimental error. The overall appearance of the data seems to indicate that the nitrogen content does not change much with temperature or residence time. This observation is different from the trend reported by Chen (1991), which showed that the nitrogen content decreased with increase in reaction temperature.

The lower hydrogen content of chars collected at higher residence time (shown in Figs. 4.29 to 4.31) suggests that there is a continued dehydrogenation process after 15 ms in all three temperature conditions. However, a similar trend for nitrogen content in chars is not seen. Compared with data for soot samples, the nitrogen content of chars (around 1.0% to 1.5%) is higher than that in soot samples (around 0.5%). This means that the fuel nitrogen in parent coal is more likely to stay in the char than in the soot.

Kinetics of Soot Formation and Agglomeration

Soot formation in coal pyrolysis is a very fast process. A low activation energy for soot formation (198.9 kJ/mol or 47.6 kcal/mol) was obtained based on the soot formation simulation. The fast reaction is probably due to the similarity of the tar structure to that of the soot; the multi-ring aromatic molecules are able to polymerize very rapidly. The fast reaction may have implications in turbulent systems, so that

mixing-limited turbulent reactions may be applicable. Even though the soot formation process is very complicated and involves many steps, the first order global mechanism presented in Chapter 5 (Fig. 5.7) can be used to simplify the description of the process. The calculated soot yields are in very good agreement with the experimental data.

Agglomeration or aggregation is also a fairly rapid process in coal pyrolysis. The distribution between small soot agglomerates ($<5 \mu\text{m}$) and large agglomerates ($>5 \mu\text{m}$) changed significantly within a residence time of 45 ms, as shown in Figs. 4.15 through 4.20. Based on the above discussion, the agglomeration process in coal pyrolysis is very different from that in conventional hydrocarbon pyrolysis or combustion. Transport processes are involved, which may be difficult to model. The model shown in Fig. 5.7 is probably an oversimplification of the process. However, this model does predict the variation in the distribution between small and large soot agglomerates with residence time (see Figs. 5.9 through 5.12). The simulation results show that the soot agglomeration rate does follow an Arrhenius rate expression.

Chapter 7

CONCLUSIONS AND RECOMMENDATIONS

In a large-scale pulverized coal furnace, soot is formed due to the secondary gas-phase reactions of coal volatiles that are released during particle heatup. In practical pulverized coal furnaces, the existence of soot particles in the near-burner region is important because it lowers the flame temperatures in that region due to radiative heat transfer. The reduced temperature will in turn influence the formation of NO_x and other pollutants. Determination of the properties of coal-derived soot, soot formation chemistry in a typical pulverized coal firing condition, and product and element distributions in pyrolysis of coals of various rank is essential to the development of comprehensive coal combustion models.

In this study, a flat-flame laminar flow reactor was used to simulate the temperature and gas-phase environment in the flame region of an industrial furnace. Coal particles were pyrolyzed in the post-flame zone of a $\text{CH}_4/\text{H}_2/\text{air}$ flat-flame operated under fuel rich conditions with almost no oxygen existing in the post-flame region. This oxygen-free environment is thought to be representative of the pyrolysis environment in large-scale pulverized coal furnaces. Previously-reported experiments were conducted in pure argon. In large-scale systems, the particle loading is high enough to prevent oxygen from penetrating very far into the volatiles cloud. However, post-flame gases (such as H_2O and CO_2) and oxygen-containing radicals (such as OH) are thought to be present in the volatiles cloud, since product recirculation is essential to many burner stabilization schemes. Therefore, soot particles obtained in the present experiments are thought to be

representative of the size and composition of soot particles generated in large-scale furnaces.

A thermophoretic technique was applied to extract soot and other aerosol deposits from the soot cloud in the laminar flat flame reactor. The sampling method yielded high quality images of deposits using the transmission electron microscopy (TEM), which allowed a detailed examination of soot particle morphology as a function of particle residence time.

Based on observations of the TEM micrographs, soot was found to exist in both distinct single particles and agglomerates. The primary soot particles range from 25 to 60 nm in diameter. The sizes of non-spherical soot agglomerates can be as large as 800 nm under the experimental conditions examined here (i.e., O₂-free conditions). These observations in soot clouds during coal devolatilization are different from previous results obtained from visual observations of single particle combustion (in 8% O₂), where soot formed streamers in the particle wake.

Unstable liquid deposits were also observed with the TEM for samples obtained at low and intermediate residence times. The liquid droplets are thought to be high molecular weight tars that were released during coal pyrolysis, that have undergone some degree of secondary reaction (and hence are soot precursors), and that condensed on the cold TEM grid. This tar deposition was not observed at high residence times. No such tar deposits were observed in thermophoretic sampling experiments in a butane flame. This supports the hypothesis that soot formation in coal combustion proceeds by a different mechanism (Wornat, et al., 1988b) than reported for simple hydrocarbon fuels (such as butane).

Bulk sampling experiments were also performed to collect soot from six coals of various rank in the laminar flat flame reactor. A nitrogen-quenched and water-cooled suction probe was used to collect char and soot samples. Small soot particles were aerodynamically separated from char particles by the combination of a virtual impactor

and a cyclone. Bulk collection experiments were conducted at three temperature conditions and four residence times for each coal. All soot and char samples were weighed and analyzed to obtain total volatiles yield, soot yields, and elemental compositions of char and soot.

Samples collected in the cyclone and on the soot filters were examined under a scanning electron microscope (SEM). The size of the primary soot particles was comparable to that obtained in the thermophoretic experiments. Large soot agglomerates were found to be mixed with the char particles in the cyclone. These large soot agglomerates ranged in size from 10 to 30 μm , and were much larger than the soot agglomerates obtained in hydrocarbon flames. The large soot agglomerates were separated from char particles by a sieve with openings of 38 μm . The formation mechanism of these large soot agglomerates is unclear. Long residence times in a limited region are generally required for the formation of large soot agglomerates, the scenario similar to an individual volatile flame around a char particle existing in oxygen rich conditions may also be present (to a small degree) in this O_2 -free environment.

Volatile yields in these experiments are slightly higher than the reported values in the literature, due to the high temperature and high heating rate conditions in the flat flame reactor. Most of volatiles are released in a short period of time (within 15 ms). Tar release was completed earlier than total volatile release. For the two low rank coals examined, increases in mass release continued after predicted volatile release ceased, which may be indicative of the vaporization of mineral matter such as Na. No such indication of mineral matter release was observed for the higher rank coals.

Total soot yield is related to temperature and coal rank. Residence time showed little effect on total soot yield in this study because the soot formation was very fast at the high temperature conditions examined. High soot formation rates in the temperature range from 1650 K to 1900 K suggest that mixing-limited turbulent reactions may be applicable to turbulent systems. Soot yield decreased with increases in temperature for

the temperature range examined. The soot yield at 1650 K was higher than the soot yield at the other two temperature conditions. Plots of coal-derived soot yield versus temperature are bell-shaped when soot yields reported in the literature at lower temperature are combined with the data in this study. The temperature for peak soot yield for coal-derived soot seems to be lower than that reported for benzene or butadiene. This suggests that soot from coal volatiles is formed at a lower temperature than from simple hydrocarbons. One example for this phenomena is that large aromatic structures already exist in coal tar, whereas the generation of higher molecular weight PAH from pyrolysis of benzene or butadiene requires high temperatures.

Total coal-derived soot yield was shown to be related to tar yield. Based on the results of this study, a coal with a high tar yield (such as a high volatile bituminous coal) would have a high soot yield, because tar is the precursor of soot. The trend in the soot yield versus coal rank was directly related to the tar yield. However, the soot yield in these experiments was always lower than the predicted tar yield, suggesting that some degree of tar gasification or cracking occurred. This may have been caused by the oxygen-containing species present in the post-flame gases in the reactor, such as OH and O radicals, H₂O, and CO₂.

Soot samples collected at the lowest residence time and at the lowest pyrolysis temperature exhibited the highest hydrogen content. In high temperature conditions, the dehydrogenation process stopped before the earliest collection point (<15 ms). The C/H mole ratios for the mature soot samples collected at longer residence times were comparable to those reported for soot from simple hydrocarbon flames. The content of nitrogen in each soot sample was found to be lower than the content of nitrogen in the corresponding char. The nitrogen contents in soot samples were roughly independent of residence time and temperature conditions, although a large amount of scatter was observed in the nitrogen data.

A simple kinetics model was proposed for soot formation and agglomeration. This model was used in conjunction with the CPD model for devolatilization. Kinetics data were obtained by fitting the experimental results. Very good agreement was shown between the calculated soot yields and measured soot yields. The modeling results indicated that soot formation from tar was very rapid, as indicated by a low activation energy.

Unfortunately, it was not possible to answer all of the questions regarding coal-derived soot in the limits of this work. Suggested future research should clarify the formation mechanism for large soot agglomerates, quantify the size distribution of soot agglomerates, perform *in-situ* measurements of the soot volume fraction and optical properties, and finally incorporate all experimental results into a comprehensive coal combustion model such as PCGC-3. The soot formation mechanism could be further examined by combining high and low temperature experiments. Also, pyrolysis experiments (such as performed here) should be combined with the combustion experiments that causes volatiles clouds around the individual particles.

REFERENCES

- Ahluwalia, R. K. and K. H. Im, "Spectral Radiative Heat Transfer in Coal Furnaces Using a Hybrid Technique," *Journal of the Institute of Energy*, **67**, 23 (1994).
- Axworthy, A. E., V. H. Dayan and G. B. Martin, "Reaction of Fuel-Nitrogen Compounds Under Conditions of Inert Pyrolysis," *Fuel*, **57**, 29 (1978).
- Balling, R., L. Borup, B. Busaker, T. Chambers, D. Davidson, G. Gritton, J. Free, A. Parkinson, J. Talbert, D. Warren, *OptdesXTM Users Manual*, Design Synthesis, Inc. (1994).
- Baxter, L. L., "The Release of Iron During Coal Combustion," *Sandia Report*, SAND95-8234 (1995a).
- Baxter, L. L., "The Release of Inorganic Material During Coal Combustion," *Sandia Report*, SAND95-8252 (1995b).
- Bertrand, C. and Delfau, J. L., "Mechanism of Soot Formation in Hydrocarbon Flames," *Combust. Sci. Tech.*, **44**, 29 (1985).
- Bruinsma, O. S. L., R. S. Geertsma, P. Bank and J. A. Moulijn, "Benzene and derivatives," *Fuel*, **67**, 327 (1988).
- Bruinsma, O. S. L., P. J. Tromp, H. J. Nolting and J. A. Moulijn, "Gas Phase Pyrolysis of Coal-Related Compounds in a Coiled Tube Flow Reactor, 2. Heterocyclic Compounds, Their Benzo and Dibenzo Derivatives," *Fuel*, **67**, 334 (1988).
- Cattolica, R. J., "OH Radical Nonequilibrium in Methane-Air Flat Flames," *Combustion and Flames*, **44**, 43 (1982).
- Chen, J., "Effect of Secondary Reactions on Product Distribution and Nitrogen Evolution From Rapid Coal Pyrolysis," Ph.D. dissertation, Stanford University (1991).
- Chen, J. and S. Niksa, "A Rapid Flow Reactor For High-temperature Reactivity Studies of Pulverized Solid," *Rev. Sci. Instrum.*, **63**, 3 (1992a)
- Chen, J. and S. Niksa, "Coal Devolatilization During Rapid Transient Heating. Part 1: Primary Devolatilization," *Energy & Fuels*, **6**, 254 (1992b).
- Chen, J., C. Castagnoli, and S. Niksa, "Coal Devolatilization During Rapid Transient Heating. Part 2. Secondary Pyrolysis," *Energy and Fuels*, **6**, 264 (1992c).

- Chen, J. and S. Niksa, "Suppressed Nitrogen Evolution From Coal-derived Soot and Low-volatility Coal Chars," *Twenty-Fourth Symposium (International) on Combustion*, The Combustion Institute, 1269 (1992d).
- Daines, R. L., *Collection and Characterization of Pyrolyzed Coal Char and Tar at High Pressure*, MS thesis, Brigham Young University (1990).
- Dobbins, R. A. and C. M. Megaridis, "Morphology of Flame-Generated Soot As Determined by Thermophoretic Sampling," *Langmuir*, **3**, 254 (1987).
- Doolan, K. R., J. C. Mackie, and R. J. Tyler, "Coal Flash Pyrolysis: Secondary Cracking of Tar Vapors in the Range 870-2000 K," *Fuel*, **66**, 572 (1987).
- Felske, J. D. and C. L. Tien, "Calculation of the Emissivity of Luminous Flames," *Combustion Science and Technology*, **7**, 25 (1973).
- Finlayson-Pitts B. J. and J. N. Pitts, Jr., *Atmospheric Chemistry: Fundamentals and Experimental Techniques*, John Wiley & Sons (1986).
- Fletcher, T. H., "Time-Resolved Particle Temperature and Mass Loss Measurements of a Bituminous Coal During Devolatilization," *Combustion and Flame*, **78**, 223 (1989).
- Fletcher, T. H., M. S. Solum, D. M. Grant, S. Critchfield, and R. J. Pugmire, "Solid-State ^{13}C and ^1H NMR Studies of the Evolution of the Chemical Structure of Coal Char and Tar During Devolatilization," *Twenty-Third Symposium (International) on Combustion*, The Combustion Institute, Pittsburgh, PA, 1231 (1990a).
- Fletcher, T. H., A. R. Kerstein, R. J. Pugmire and D. M. Grant, "Chemical Percolation Model for Devolatilization. 2. Temperature and Heating Rate Effects on Product Yields," *Energy and Fuels*, **4**, 54 (1990b).
- Fletcher, T. H. and D. R. Hardesty, "Compilation of Sandia Coal Devolatilization Data Milestone Report," *Sandia Report*, SAND92-8209 (1992).
- Fletcher, T. H., A. R. Kerstein, R. J. Pugmire, M. S. Solum and D. M. Grant, "Chemical Percolation Model for Devolatilization. 3. Direct Use of ^{13}C NMR Data To Predict Effects of Coal Type," *Energy and Fuels*, **6**, 414 (1992).
- Freihaut, J. D., M. F. Zabielski and D. J. Seery, "A Parametric Investigation of Tar Release in Coal Devolatilization," *Nineteenth Symposium (International) on Combustion*, The Combustion Institute, 1159 (1982).
- Freihaut, J. D., W. M. Proscia and D. J. Seery, "Chemical Characteristics of Tars produced in a novel low-severity, entrained-flow reactor," *Energy and Fuels*, **3**, 692 (1989).

- Freihaut, J. D., W. M. Proscia and J. C. Mackie, "Chemical and Thermochemical Properties of Heavy Molecular Weight Hydrocarbons Evolved During Rapid Heating of Coal of Varying Rank Characteristics," *Combust. Sci. and Tech.*, **93**, 323 (1993).
- Frenklach, M., D. W. Clary, W. C. Gardiner and S. E. Stein, "Detailed Kinetic Modeling of Soot Formation in Shock-Tube Pyrolysis of Acetylene," *Twentieth Symposium (International) on Combustion*, The Combustion Institute, 887 (1984).
- Frenklach, M., D. W. Clary, W. C. Gardiner and S. E. Stein, "Effect of Fuel Structure on Pathways to Soot," *Twenty-First Symposium (International) on Combustion*, The Combustion Institute, 1067 (1986).
- Frenklach, M. and H. Wang, "Detailed Modeling of Soot Particle Nucleation and Growth," *Twenty-Third Symposium (International) on Combustion*, The Combustion Institute, 1559 (1990).
- Gale, T. K., C. H. Bartholomew and T. H. Fletcher, "Decreases in the Swelling and Porosity of Bituminous Coals During Devolatilization at High Heating Rates," *Combustion and Flame*, **100**, 94 (1994).
- Genetti, D. B., T. H. Fletcher and R. J. Pugmire, "Predicting ^{13}C NMR Measurements Based on Coal Elemental Composition," *Proceedings of the 8th International Conference on Coal Science*, Oviedo, Spain, 331 (1995).
- Glassman, I., "Soot Formation in Combustion Processes," *Twenty-Second Symposium (International) on Combustion*, The Combustion Institute, 295 (1988).
- Grosshandler, W. L. and J. Vantelon, "Predicting Soot Radiation in Laminar Flames," *Combustion Science and Technology*, **44**, 125 (1985).
- Harold, R. Clark, R. P. Stawicki, I. P. Smyth, and E. Potkay, "Collection and Characterization of Soot from an Optical Fiber Preform Torch," *J. Am. Ceram. Soc.*, **73**, 2987 (1990).
- Haynes, B. S. and G. P. Prado, "Soot and PAH Formation in Coal Combustion," *Pulverized Coal Combustion: Pollutant Formation and Control*, EPA/600/8-90/049, PB90-229253 (1980).
- Haynes, B. S. and H. G. Wagner, "Soot Formation," *Prog. Energy Combustion Science*, **7**, 229 (1981).
- Haynes, B. S., "Soot and Hydrocarbons in Combustion," *Fossil Fuel Combustion-A Source Book*, John Wiley & Sons, Inc. (1991).
- Hodges, J. and D. Foster, "Soot Coagulation with Surface Growth Kinetics," *Combustion Science and Technology*, **51**, 235 (1987).

- Hospital, A. and P. Roth, "In-Situ Mass Growth Measurements of Charged Soot Particles From Low Pressure Flames," *Twenty-Third Symposium (International) on Combustion*, The Combustion Institute, 1573 (1990).
- Houser, T. J., M. E. McCarville and T. Biftu, "Kinetics of the Thermal Decomposition of Pyridine in a Flow System," *International Journal of Chemical Kinetics*, **12**, 555 (1980).
- Howard, J. B., "Carbon Addition and Oxidation Reactions in Heterogeneous Combustion and Soot Formation," *Twenty-Third Symposium on Combustion*, The Combustion Institute: Pittsburgh, PA, 1107 (1990).
- Ito, H. O. Fujita and K. Ito, "Agglomeration of Soot Particles in Diffusion Flames Under Microgravity," *Combustion and Flames*, **99**, 363 (1994).
- Jackson, G. S., C. T. Averdisian and J. C. Young, "Observations of Soot During Droplet Combustion at Low Gravity: Heptane and Heptane/Monochloroalkane Mixtures," *International Journal of Heat and Mass Transfer*, **35**, 2017 (1992).
- Jagoda, I. J., G. Prado and J. Lahaye, "An Experimental Investigation into Soot Formation and Distribution in Polymer Diffusion Flames," *Combustion and Flame*, **37**, 261 (1980).
- Kambara, S., T. Takarada, Y. Yamamoto and K. Kato, "Relation between Functional Forms of Coal Nitrogen and Formation of NO Precursors during Rapid Pyrolysis," *Energy and Fuels*, **7**, 1013 (1993).
- Kawamura, M., T. Ishiguro and H. Morimoto, "Electron Microscopic Observation of Soots in Used Diesel Engine Oils," *Lubrication Engineering*, **43**, 572 (1987).
- Kee, R. J., J. F. Grcar, M. D. Smooke and J. A. Miller, "A Fortran Program for Modeling Steady Laminar One-Dimensional Premixed Flame," *Sandia Report*, SAND85-8240 (1985).
- Kern, R. D. and K. Xie, "Shock Tube Studies of Gas Phase Reactions Preceding the Soot Formation Process," *Prog. Energy Combust. Sci.*, **17**, 191 (1991).
- Lau, C. W. and S. Niksa, "The Impact of Soot on the Combustion Characteristics of Coal Particles of Various Types," *Combustion and Flame*, **95**, 1 (1993).
- Lhuissier, N., G. Gouesbet and M. E. Weill, "Extensive Measurements in Soot Particles in Laminar Premixed Flames by Quasi Elastic Light Scattering Spectroscopy," *Combustion Science and Technology*, **67**, 17 (1989).
- Ma, J., T. H. Fletcher and B. W. Webb, "Thermophoretic Sampling of Coal-Derived Soot Particles During Devolatilization," *Energy and Fuels*, **9**, 802 (1995a).

- Ma, J., T. H. Fletcher and B. W. Webb, "Effect of Flame Environment on Soot Formation in Coal Combustion," *Proceedings of the 8th International Conference on Coal Science*, Oviedo, Spain, 869 (1995b).
- Mackie, J. C., M. B. Colket and P. F. Nelson, "Shock Tube Pyrolysis of Pyridine," *The Journal of Physical Chemistry*, **94**, 4099 (1990).
- Mackie, J. C., M. B. Colket, P. F. Nelson and M. Esler, "Shock Tube Pyrolysis of Pyrrole and Kinetic Modeling," *International Journal of Chemical Kinetics*, **23**, 733 (1991).
- Megaridis, C. M. and R. A. Dobbins, "Comparison of soot Growth and Oxidation in Smoking and Non-Smoking Ethylene Diffusion Flames," *Combustion Science and Technology*, **66**, 1 (1989).
- Mengüç, M. P. and R. Viskanta, "A Sensitivity Analysis for Radiative Heat Transfer in a Pulverized Coal-fired Furnace," *Combustion Science and Technology*, **51**, 51 (1987).
- Mengüç, M. P. and R. Viskanta, "Effect of Fly-Ash Particles on Spectral and Total Radiation Blockage," *Combustion Science and Technology*, **60**, 97 (1988).
- Mckinnon, J. T. and J. B. Howard, "The Roles of PAH and Acetylene in Soot Nucleation and Growth," *Twenty-Fourth Symposium (International) on Combustion*, The Combustion Institute, 965,(1991).
- McLean, W. J., D. R. Hardesty and J. H. Pohl, "Direct Observations of Devolatilizing Pulverized Coal Particles in a Combustion Environment," *Eighteenth Symposium (International) on Combustion*, 1239 (1981).
- Monson, C., "Char Oxidation at High Pressures," Ph.D. Dissertation, Brigham Young University (1992).
- Musarra, S. P., T. H. Fletcher, S. Niksa and H. A. Dwyer, "Heat and Mass Transfer in the vicinity of a Devolatilizing Coal Partilce," *Combustion Science and Technology*, **45**, 289 (1986).
- Nagle, J. and R. F. Strickland-Constable, "Oxidation of Carbon Between 1000-2000 °C," *Proceedings of the Fifth Carbon Conference*, **1**, 154 (1962).
- Nelson, P. F., M. D. Kelly and M. J. Wornat, "Conversion of Fuel Nitrogen in Coal Volatiles to NO_x Precursors Under Rapid Heating Conditions," *Fuel*, **70**, 403 (1991).
- Nenniger, R. D., J. B. Howard and A. F. Sarofim, "Sooting Potential of Coals," *Proceedings of the 1983 International Conference on Coal Science*, 521 (1983).
- Nenniger, R. D., *Aerosol Produced from Coal Pyrolysis*, D.Sc. dissertation, MIT (1986).

- Niksa, S., "FLASHCHAIN Theory for Rapid Coal Devolatilization Kinetics. 1. Formulation, 2. Impact of Operating Condition, 3. Modeling the Behavior of Various Coals," *Energy and Fuels*, **5**, 647 (1991).
- Olson, D. B. and J. C. Pickens, "The Effects of Molecular Structure on Soot Formation, I. Soot Thresholds in Premixed Flames," *Combustion and Flame*, **57**, 199 (1984).
- Olson, D. B. and J. C. Pickens, "The Effects of Molecular Structure on Soot Formation, II. Diffusion Flames," *Combustion and Flame*, **62**, 43 (1985).
- Park, C. and J. P. Appleton, "Shock-Tube Measurements of Soot Oxidation Rates," *Combustion and Flames*, **20**, 369 (1973).
- Perry, R. H. and D. Green, *Perry's Chemical Engineers' Handbook*, Sixth Edition, McGraw-Hill, Inc. (1984).
- Prado, G. P., M. L. Lee, R. A. Hites, D. P. Hoult and J. B. Howard, "Soot and Hydrocarbon Formation in a Turbulent Diffusion Flame," *Sixteenth Symposium (International) on Combustion*, The Combustion Institute, Pittsburgh, PA, p.649 (1976).
- Pugmire, R. J., M. S. Solum, D. M. Grant, S. Critchfield, and T. H. Fletcher, "Structural Evolution of Matched Tar/Char Pairs in Rapid Pyrolysis Experiments," *Fuel*, **70**, 414 (1991).
- Puri, R., R. J. Santoro and K. C. Smyth, "The Oxidation of Soot and Carbon Monoxide in Hydrocarbon Diffusion Flames," *Combustion and Flames*, **97**, 129 (1994).
- Radcliffe, S. W. and J. P. Appleton, "Soot Oxidation Rates in Gas Turbine Engines," *Combustion Science and Technology*, **4**, 171 (1971).
- Rosner, D. E., D. W. Mackowski and P. Garcia-Ybarra, "Size- and Structure-Insensitivity of the thermophoretic Transport of Aggregated Soot Particles in Gases," *Combustion Science and Technology*, **80**, 87 (1991)
- Saito, K., A. S. Gordon, F. A. Williams and W. F. Stickle, "A Study of the Early History of Soot Formation in Various Hydrocarbon Diffusion Flames," *Combustion Science and Technology*, **80**, 103 (1991).
- Sato, H., D. R. Tree, J. T. Hodges and D. E. Foster, "A Study on the Effect of Temperature on Soot Formation in a Jet Stirred Combustor," *Twenty-Third Symposium (International) on Combustion*, The Combustion Institute, 1469 (1990).
- Seeker, W. R., G. S. Samuelson, M. P. Heap, and J. D. Trolinger, "Thermal Decomposition of Pulverized Coal Particles," *Eighteenth Symposium (International) on Combustion*, The Combustion Institute, Pittsburgh, PA, p. 1213 (1981).

- Serio, M. A., W. A. Peter and J. Howard, "Kinetics of Vapor-Phase Secondary Reactions of Prompt Coal Pyrolysis Tars," *Ind. Eng. Chem. Res.*, **26**, 1831 (1987).
- Siegel, R. and J. R. Howell, *Thermal Radiation Heat Transfer*, Third Edition, Hemisphere Publishing Corporation (1992).
- Sivathanu, Y. R., J. P. Gore and J. D. Dolinar, "Transient Scalar Properties of Strongly Radiating Jet Flames," *Combustion Science and Technology*, **76**, 45 (1991).
- Smyth, K. C., J. H. Miller, R. C. Dorfman, W. G. Mallard and R. J. Santoro, "Soot Inception in a Methane/Air Diffusion Flame as Characterized by Detailed Species Profiles," *Combustion and Flame*, **62**, 157 (1985).
- Solomon, P. R. and M. B. Colhet, "Evolution of fuel nitrogen in coal devolatilization," *Fuel*, **57**, 749 (1978).
- Solomon, P. R., D. G. Hamblen, R. M. Carangelo, M. A. Serio and G. V. Deshpande, "General Model of Coal Devolatilization," *Energy and Fuels*, **2**, 405 (1988).
- Solomon, P. R., D. G. Hamblen, Z. Yu and M. A. Serio, "Network Models of Coal Thermal Decomposition," *Fuel*, **69**, 754 (1990).
- Syed, K. J., C. D. Stewart and J. B. Moss, "Modeling Soot Formation and Thermal Radiation in Buoyant Turbulent Diffusion Flames," *Twenty-Third Symposium (International) on Combustion*, The Combustion Institute, 1533 (1990).
- Timothy, L. D., D. Froelich, A. F. Sarofim and J. M. Beer, "Soot Formation and Burnout during the Combustion of Dispersed Pulverized Coal Particles," *Twenty-First Symposium (International) on Combustion*, The Combustion Institute, 1141 (1986).
- Ugarte, D., "Curling and Closure of Graphitic Networks Under Electron-Beam Irradiation," *Nature*, **359**, 707 (1992).
- Wang, H., Personal Communication (1994).
- Weill, M.E., N. Lhuissier and G. Gouesbet, "Mean Diameters and Number Densities in Premixed Flat Flames CH₄-O₂ By Diffusion Broadening Spectroscopy," *Applied Optics*, **25**, 1676 (1986).
- Wornat, M. J., A. F. Sarofim and J. P. Longwell, "Changes in the Degree of Substitution of Polycyclic Aromatic Compounds from Pyrolysis of a High-Volatile Bituminous Coal," *Energy and Fuels*, **1**, 431 (1987).
- Wornat, M. J., A. F. Sarofim, J. P. Longwell and A. L. Lafleur, "Effect of Pyrolysis Conditions on the Composition of Nitrogen-Containing Polycyclic Aromatic Compounds From a Bituminous Coal," *Energy & Fuels*, **2**, 775 (1988a).

Wornat, M. J., A. F. Sarofim and J. P. Longwell, "Pyrolysis-Induced Changes in the Ring number Composition of Polycyclic Aromatic Compounds from a High Volatile Bituminous coal," *Twenty-Second Symposium (International) on Combustion*, The Combustion Institute: Pittsburgh, PA, 135 (1988b).

Wornat, M. J., A. F. Sarofim and A. L. Lafleur, "The Pyrolysis of Anthracene as a Model Coal-Derived Aromatic Compound," *Twenty-Fourth Symposium (International) on Combustion*, The Combustion Institute, Pittsburgh, PA, 955 (1992).

Appendix A

EFFECT OF SOOT RADIATION ON FLAME TEMPERATURE

The estimation of the effect of radiation on the volatile flame temperature was based on Goudy case, a full-scale boiler case used extensively at the Advanced Combustion Engineering Research Center (ACERC) of BYU for comprehensive coal combustion modeling. In this case, the total air flow is around 130 kg/s. Burners are located on the four corners of the furnace and cover a height about 2 meters (including secondary air jets). Primary air consists of about 10% of the total air. Therefore, for each corner the flow rates of total air \dot{m}_{air}^t and primary air \dot{m}_{air}^p are

$$\dot{m}_{air}^t = \frac{130}{4} = 32.5 \quad \text{kg/s}$$

$$\dot{m}_{air}^p = 0.1\dot{m}_{air}^t = 3.25 \quad \text{kg/s}$$

Assuming that there is 20% excess air, the mole flow rate of oxygen needed for the combustion at each corner is

$$F_{O_2} = \frac{32.5}{1.2 \times 0.029 \times 4.76} = 196.2 \quad \text{mol/s}$$

Also assuming that coal is mainly consist of carbon and the coal combustion is basically carbon combustion, i.e.



then, the amount of coal injected at each corner \dot{m}_{coal}^Y can be calculated.

$$\dot{m}_{coal}^Y = 0.012F_{O_2} = 0.012 \times 196.2 = 2.354 \quad \text{kg/s}$$

If 10% of the coal survives in a volatiles flame as soot, the mass flow rate of soot particles at each corner is

$$\dot{m}_{soot} = 0.1\dot{m}_{coal} = 0.2354 \quad \text{kg/s}$$

To simplify the calculation, it is assumed that the soot-laden stream of primary air forms a cylindrical volatiles flame that is 0.5 m in diameter and 3 m in length, with a uniform temperature of 2000 K as shown in Fig. A-1. The volumetric flow rate of primary air at this temperature is

$$Q_{air}^p = \frac{\dot{m}_{air}^p RT}{PM_{w,air}} = \frac{3.25 \times 8.314 \times 2000}{1.013 \times 10^5 \times 0.029} = 18.4 \quad \text{m}^3/\text{s}$$

The density of soot ρ_{soot} is assumed to be 1800 kg/m³ (Felske and Tien, 1973). The average volume fraction of soot in the flame f_v is

$$f_v = \frac{\left(\frac{\dot{m}_{soot}}{\rho_{soot}} \right)}{Q_{air}^p} = \frac{\left(\frac{0.2354}{1800} \right)}{18.4} = 7.11 \times 10^{-6}$$

The mean path length L for the cylindrical flame can be estimated as (Siegel and Howell, 1992):

$$L = 0.9 \frac{4V}{A} = 0.9 \frac{4 \times 3 \times \left(\frac{\pi \times 0.5^2}{4} \right)}{2 \left(\frac{\pi \times 0.5^2}{4} \right) + \pi \times 0.5 \times 3} = 0.415 \quad \text{m}$$

The emittance of luminous sooting flames ε was studied by Felske and Tien (1973). According to their study, the total emittance is affected by emitting media such as gases (mainly water and carbon dioxide) and soot. Flame temperature also has effect on total emittance. If soot is very small, the scattering effect on ε is negligible. Based on the optical properties measured for soot from hydrocarbon flames, Felske and Tien calculated the tabulated the total emittance as a function of temperature, partial pressures of water and carbon dioxide, path length L , and the product of soot volume fraction and path length $f_v L$. From these tables, the emittance of gas consisting of 12% CO₂ and

13% H₂O at 1 atm and 1600 K with a path length of 0.2 m is around 0.2. In the case of coal combustion, the concentration of CO₂ and H₂O in a volatile flame is lower than these concentrations and, therefore, the emittance of gas should be less than 0.2. The emittance caused by the existence of char particles is hard to calculate due to their scattering nature. Even though the volume fraction of char is higher than that of soot, the imaginary part of the complex refractive index of char is usually much smaller than that of soot. Also the total surface area of char particles is much smaller than that of soot particles. Therefore, the absorption of radiative energy by char is limited. The product of soot volume fraction and path length in this case is

$$f_v L = 0.415 \times 7.11 \times 10^{-6} = 2.95 \times 10^{-6} \quad \text{m},$$

which corresponding to a flame emittance of about 0.95 based on Felske and Tien's calculation. Therefore, the consideration of the soot in the volatiles flame will increase the flame emittance drastically. If the emittance of the flame without considering soot is 0.2 (only consider gases and char), the decrease of flame temperature due to the addition of soot can be estimated as follows.

Assuming the calculated temperature without consideration of soot T_o is 2000 K, the real temperature is T , and the emittance of the flame is changed from $\epsilon_o = 0.2$ to $\epsilon = 0.95$, the real temperature of the cylindrical flame can be calculated based on the energy balance that the increase in radiative heat loss due to the emittance change is equal to the decrease in the enthalpy of the primary gas stream.

$$\left(\dot{m}_{coal} C_{p,coal} + \dot{m}_{air}^p C_{p,air} \right) (T_o - T) = \epsilon A \sigma (T^4 - T_w^4) - \epsilon_o A \sigma (T_o^4 - T_w^4) \quad (\text{A-2})$$

where $C_{p,air}$ and $C_{p,coal}$ are average heat capacities of air and coal respectively, σ is the Stefan-Boltzmann coefficient, A is the surface area of the volatiles flame, and T_w is the temperature of the furnace wall (assumed to be 800 K). The surface area available for emission is

$$A = 2\left(\frac{\pi \times 0.5^2}{4}\right) + \pi \times 0.5 \times 3 = 5.11 \quad \text{m}^2$$

The average heat capacity of air is assumed to be the heat capacity at 1800 K ($C_{p,air} = 1286 \text{ J / kg} \cdot \text{K}$). Heat capacity of coal $C_{p,coal}$ is around 1000 J / kg · K (Perry and Green, 1984). Solving Eq. A-2, the real temperature of the volatiles flame is

$$T = 1755 \text{ K}$$

This means the flame temperature will be lowered by 245 K if the effect of soot radiation is considered. If the flame dimension is smaller and emittance of gas plus char is higher than 0.2, the temperature difference could be lower. It is recognized that radiation calculations in a large furnace are significantly more complex than indicated by this simple analysis. However, this analysis illustrates the potential magnitude of the effect of soot radiation.

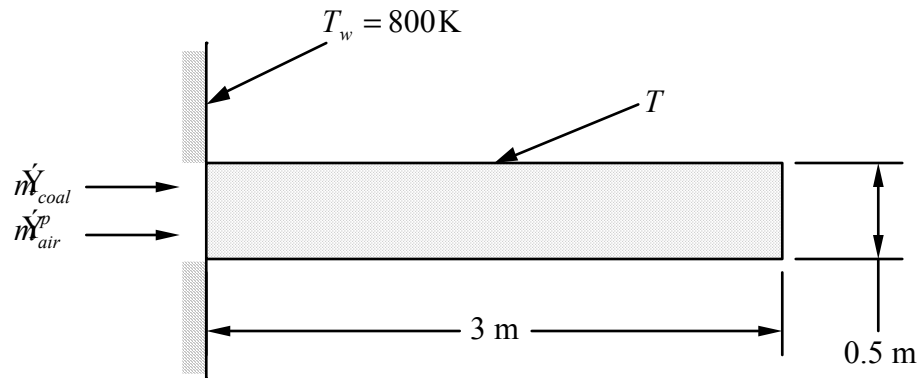


Figure A-1. The dimension of the volatile flame used for calculation.

Appendix B

CODE FOR GENERATION OF STEPPING SIGNAL (used to drive the step motor for the particle feeder)

```
// This is a program for pulse generation written in C++
#include <dos.h>
#include <iostream.h>
#include <time.h>
#include <sys\timeb.h>

main()
{
    long pp, tpp, tpv, twait = 0, tms = 0;
    float step, testtime;
    int port = 888;
    struct timeb t;
    long initials, initialms, tmsfinal;
    cout << "enter pulse period in ms:";
    cin >> pp;
    tpp = pp/2;
    tpv = pp-tpp;
    step = 60000./pp;
    cout << "enter test time in min:";
    cin >> testtime;
    cout << "The motor is working at " << step << " steps/min...";
    ftime(&t);
    initials = t.time;
    initialms = t.millitm;
    tmsfinal = testtime*60000.;
    while (tms < tmsfinal)
    {
```

```

    _asm
    {
        mov dx, port
        mov ax, 0001H
        out dx, al□
    }
    twait = twait + tpp;
    while (tms < twait)
    {
        ftime(&t);
        tms = t.millitm - initialms + 1000 * (t.time - initials);
    }
    _asm
    {
        mov dx, port
        mov ax, 0000H
        out dx, al□
    }
    twait = twait + tpv;
    while (tms < twait)
    {
        ftime(&t);
        tms = t.millitm - initialms + 1000 * (t.time - initials);
    }
}
return 0;
}

```

Appendix C

DESIGN OF THE VIRTUAL IMPACTOR

The most important dimensions of a virtual impactor are inlet tube diameter D_o , reception tube diameter D_1 and the size of the gap between them S , as illustrated in Fig. C-1. The dimensionless parameters that govern the performance of a virtual impactor are the Reynolds number and Stokes number, namely,

$$\text{Re} = \frac{VD_o}{\nu_g} \quad (\text{C-1})$$

$$\text{Stk} = \frac{\rho_p VD_p^2}{9\mu_g D_o} \quad (\text{C-2})$$

where μ_g , ν_g and V are gas viscosity, kinematic viscosity and velocity respectively, while D_p and ρ_p are particle diameter and density. If the inlet volumetric gas flow rate Q_o is used to calculate the gas velocity and substituted into Eqs. C-1 and C-2, they become

$$\text{Re} = \frac{4Q_o\rho_g}{\pi\mu_g D_o} \quad (\text{C-3})$$

$$\text{Stk} = \frac{4\rho_p VD_p^2}{9\pi\mu_g D_o^3} \quad (\text{C-4})$$

The suggested value for Stokes number is 0.425 and is usually used as a design parameter (Nenniger, 1986; Daines, 1990). Other guidelines for best impactor performance are: $\text{Re} \approx 5000$, $D_1/D_o = 1.35$ and $S/D_o = 1$.

The temperature of the gas entering the virtual impactor T was measured to be 650 K. The ambient pressure p is 8.53×10^4 Pa. Assuming the gas has the same

viscosity as air, this temperature corresponds to a viscosity of $3.225 \times 10^{-5} \text{ N} \cdot \text{s} / \text{m}^2$. The density of the gas at 650 K and ambient pressure can be calculated based on the equation of state for ideal gas

$$\rho_g = \frac{pM_w}{RT} = \frac{8.53 \times 10^4 \times 0.029}{8.314 \times 650} = 0.458 \quad \text{kg} / \text{m}^3$$

Based on the flow measurements using calibrated rotameters, the mass flow rate of the gas entering the virtual impactor was 87.03 slpm (see Table 3.2) or 1.72 g/sec, which corresponded to a volumetric flow rate of

$$Q_o = \frac{1.72 \times 10^{-3}}{0.458} = 3.76 \times 10^{-3} \quad \text{m}^3 / \text{s}$$

Assuming that the particle density of parent coal is $1300 \text{ kg} / \text{m}^3$, the weight loss after pyrolysis is 55% and there is no swelling or shrinking of coal particles after the pyrolysis in the rapid heating conditions of this research, the char particle density can be estimated to be

$$\rho_p = 1300(1 - 0.55) = 585 \quad \text{kg} / \text{m}^3$$

The cut point diameter of particles was selected to be 5 μm . From Eq. C-4, inlet tube diameter D_o can be calculated.

$$D_o = \sqrt[3]{\frac{4\rho_p Q_o D_p^2}{9\pi\mu_g \text{Stk}}} = \sqrt[3]{\frac{4 \times 585 \times 3.76 \times 10^{-3} \times 5^2 \times 10^{-12}}{9 \times 3.14 \times 3.225 \times 10^{-5} \times 0.425}} = 8.28 \times 10^{-3} \quad \text{m}$$

The final design for D_o was 0.32 inch or 8.13 mm. A diameter of 0.43 inch or 10.9 mm was used for reception tube. Therefore,

$$\frac{D_1}{D_o} = \frac{0.43}{0.32} = 1.344$$

The Reynolds number for this design was slightly higher than the recommended value of 5000.

$$\text{Re} = \frac{4Q_o\rho_g}{\pi\mu_g D_o} = \frac{4 \times 3.76 \times 10^{-3} \times 0.458}{3.14 \times 3.225 \times 10^{-5} \times 8.13 \times 10^{-3}} = 8360$$

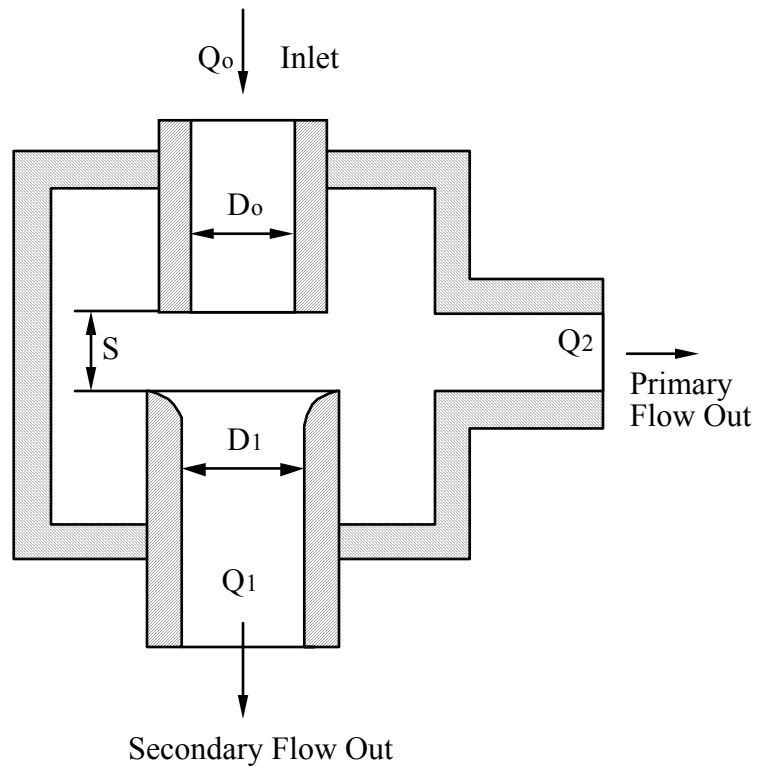


Figure C-1. Important dimensions in the design of virtual impactor.

Appendix D

DESIGN OF THE CYCLONE

The design of the cyclone was based on the guidelines described in Perry's Chemical Engineer's Handbook (1984). The dimensions of an ordinary cyclone in shown in Fig. D-1 along with some recommended relationships between these dimensions. The cut point diameter of particles D_p to be separated is related to the flow and dimension by

$$D_p = \sqrt{\frac{9\mu_g B}{2\pi N_e V(\rho_p - \rho_g)}} \quad (\text{D-1})$$

where, μ_g , V , ρ_p and ρ_g are gas viscosity, inlet velocity, particle density and gas density respectively. N_e is the effective number of turns made by the gas stream in the cyclone, and is approximately equal to 5. The inlet velocity can be expressed in term of the volumetric flow rate Q_1 .

$$V = \frac{Q_1}{BH} = \frac{Q_1}{\left(\frac{D}{4}\right)\left(\frac{D}{2}\right)} = \frac{8Q_1}{D^2} \quad (\text{D-2})$$

Putting $N_e = 5$, $B = D/4$ and Eq. D-2 into Eq. D-1 and rearranging, the design variable D can be expressed as,

$$D = \sqrt[3]{\frac{320\pi(\rho_p - \rho_g)D_p^2 Q_1}{9\mu_g}} \quad (\text{D-3})$$

According to Appendix C, $Q_1 = 0.2$, $Q_o = 0.2 \times 3.76 \times 10^{-3} = 7.52 \times 10^{-4}$, $\rho_p = 585 \text{ kg/m}^3$, $\rho_g = 0.458 \text{ kg/m}^3$ and $\mu_g = 3.225 \times 10^{-5}$. Using a cut point diameter of 5 μm , the inside diameter of the cyclone body can be calculated.

$$D = \sqrt[3]{\frac{320\pi(585 - 0.458)(5 \times 10^{-6})^2 7.52 \times 10^{-4}}{9 \times 3.225 \times 10^{-5}}} = 0.0336 \text{ m}$$

This calculated D was rounded off to 1.25 inch (0.0318 m). Circular instead of rectangular cross section of the inlet was used for simplicity of manufacturing. It was assumed that the inlet diameter D_i should be the hydraulic diameter.

$$D_i = \frac{4BH}{2(B+H)} = \frac{D}{3} = \frac{0.0318}{3} = 0.0106 \text{ m}$$

This value was also rounded off to 0.375 inch (0.0095 m). Because D_i is larger than suggested B , D' has to be smaller than the suggested value. Therefore, D' was set to be 10.9 mm. Other dimensions were determined using the suggested relations shown in Fig. D-1. All important dimensions are listed in Table D-1.

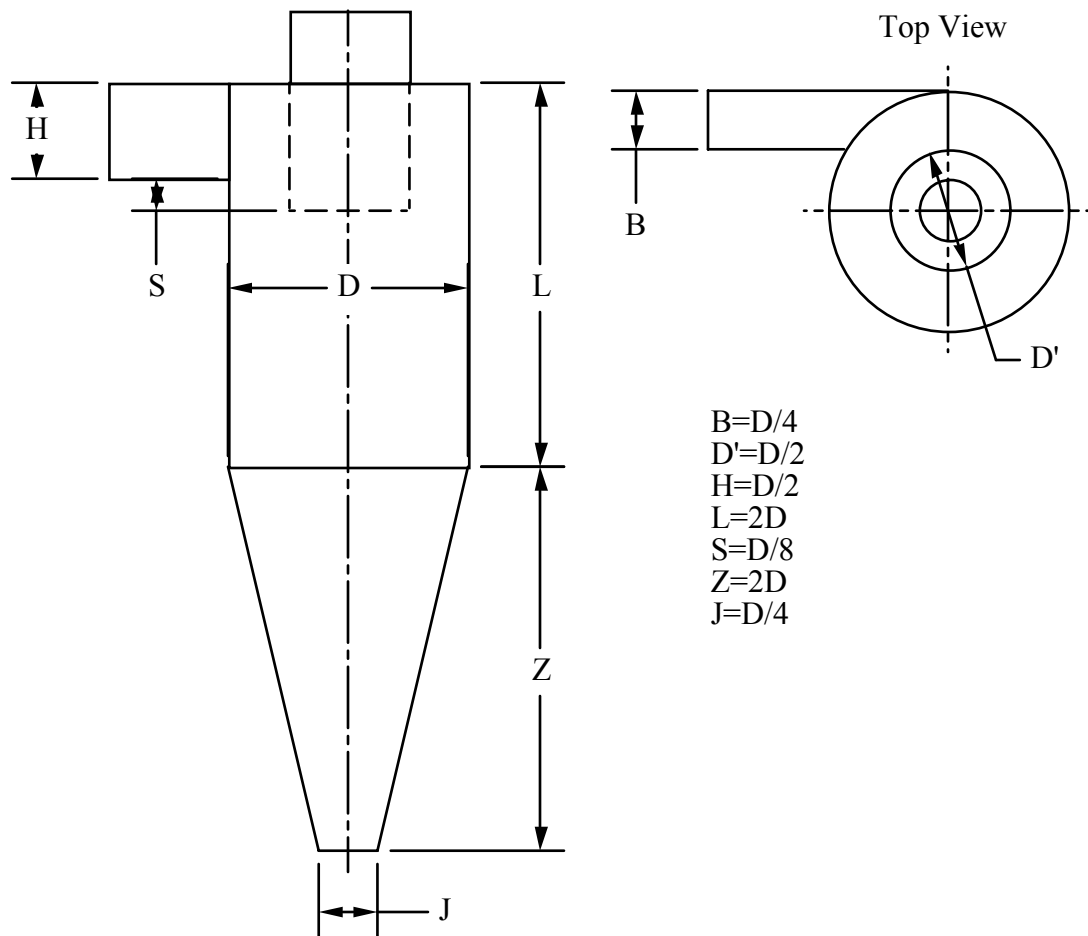


Figure D-1. Geometry of cyclone and design guidelines.

Table D-1. Major dimensions of the cyclone design.

D (mm)	D_i (mm)	D' (mm)	L (mm)	Z (mm)	S (mm)	J (mm)
31.8	9.5	10.9	63.5	63.5	3.8	7.6

Appendix E

CODE FOR OBTAINING KINETIC CONSTANTS FROM FITTING EXPERIMENTAL DATA (interfaced with optimization program)

This program is in FORTRAN.

```
CCCCCCCCCObjective function subroutineCCCCCCCCCCCCCCCCC
c-----ft: name of the out file from cpd calculation-----
c-----sexp: experimental soot yield-----
c-----ef, eg, ea, af, ag, aa: kinetic constants to be fitted-----
c-----obj: objective function to be returned-----
      subroutine fun(ef,eg,ea,af,ag,aa,obj)
      dimension z(4), sooty(4), sexp(6,3,4), tary(4)
      character*9 ft(3,6)
      double precision ef,eg,ea,af,ag,aa,obj
      open (20, file='soot.exp', status='unknown')
      ft(3,1)='pit16.out'
      ft(2,1)='pit18.out'
      ft(1,1)='pit19.out'
      ft(3,2)='ill16.out'
      ft(2,2)='ill18.out'
      ft(1,2)='ill19.out'
      ft(3,3)='uta16.out'
      ft(2,3)='uta18.out'
      ft(1,3)='uta19.out'
      ft(3,4)='poc16.out'
      ft(2,4)='poc18.out'
      ft(1,4)='poc19.out'
      ft(3,5)='die16.out'
      ft(2,5)='die18.out'
```

```

ft(1,5)='die19.out'
ft(3,6)='zap16.out'
ft(2,6)='zap18.out'
ft(1,6)='zap19.out'
z(1)=0.0254
z(2)=0.0508
z(3)=0.0762
z(4)=0.1016
do 3 ii=1,6
    do 2 jj=1,3
        do 1 kk=1,4
            read (20,*) sexp(ii,jj,kk)
1            continue
2            continue
3            continue
obj=0.0
do 30 i=1,4
    do 20 j=1,3
        call sootyield(ft(j,i),4,z,ef,eg,ea,af,ag,aa,sooty,tary)
        do 10 k=1,4
            obj=obj+(sooty(k)-sexp(i,j,k))**2.
10            continue
20            continue
30            continue
close (20)
return
end

```

```

CCCCCCCCCCCCC subroutine for soot yield at certain heights CCCCCCCCCC
CCCCCCCCCCCCC all units are metric (sec, m, K, J, kg, etc.) CCCCCCCCCC
subroutine sootyield(cond,nheight,height,ef,eg,ea,
$ af,ag,aa,sooth,tarh)
dimension sooth(nheight), ftar(500), dist(500), time(500)
dimension temp(500), height(nheight),tarh(nheight)

```

```

character*9 cond
double precision ef,eg,ea,af,ag,aa
open (10, file=cond, status='unknown')
C-----read cpd output data and do unit conversion-----
ii=0
100 ii=ii+1
read (10, *) time(ii), dist(ii), temp(ii), ftar(ii)
time(ii)=time(ii)/1000.
dist(ii)=dist(ii)/1000.
if (dist(ii).le.height(nheight)) goto 100
C-----set initail values-----
dt=0.00004
i=1
t=0.0
tarloss=0.0
soot=0.0
n=1
110 tem0=(t-time(i))/(time(i+1)-time(i))*
$ (temp(i+1)-temp(i))+temp(i)
fta0=(t-time(i))/(time(i+1)-time(i))*
$ (ftar(i+1)-ftar(i))+ftar(i)
tem5=(t+dt/2-time(i))/(time(i+1)-time(i))*
$ (temp(i+1)-temp(i))+temp(i)
fta5=(t+dt/2-time(i))/(time(i+1)-time(i))*
$ (ftar(i+1)-ftar(i))+ftar(i)
tem1=(t+dt-time(i))/(time(i+1)-time(i))*
$ (temp(i+1)-temp(i))+temp(i)
fta1=(t+dt-time(i))/(time(i+1)-time(i))*
$ (ftar(i+1)-ftar(i))+ftar(i)
dis=(t+dt-time(i))/(time(i+1)-time(i))*
$ (dist(i+1)-dist(i))+dist(i)
C-----k1-----
dgas1=ag*exp(-eg/8.314/tem0)*(fta0-tarloss)*dt
dsootf1=af*exp(-ef/8.314/tem0)*(fta0-tarloss)*dt
dsooto1=aa*exp(-ea/8.314/tem0)*soot*dt
C-----k2-----

```

```

    dgas2=ag*exp(-eg/8.314/tem5)*(fta5-tarloss-
$ (dgas1+dsootf1)/2)*dt
    dsootf2=af*exp(-ef/8.314/tem5)*(fta5-tarloss-
$ (dgas1+dsootf1)/2)*dt
    dsooto2=aa*exp(-ea/8.314/tem5)*(soot+
$ (dsootf1-dsooto1)/2)*dt
C-----k3-----
    dgas3=ag*exp(-eg/8.314/tem5)*(fta5-tarloss-
$ (dgas2+dsootf2)/2)*dt
    dsootf3=af*exp(-ef/8.314/tem5)*(fta5-tarloss-
$ (dgas2+dsootf2)/2)*dt
    dsooto3=aa*exp(-ea/8.314/tem5)*(soot+
$ (dsootf2-dsooto2)/2)*dt
C-----k4-----
    dgas4=ag*exp(-eg/8.314/tem1)*(fta1-tarloss-
$ (dgas3+dsootf3))*dt
    dsootf4=af*exp(-ef/8.314/tem1)*(fta1-tarloss-
$ (dgas3+dsootf3))*dt
    dsooto4=aa*exp(-ea/8.314/tem1)*
$ (soot+dsootf3-dsooto3)*dt
C-----Fourth order Runge-Kutaa integration-----
    tarloss=tarloss+(dgas1+dsootf1+2*
$ (dgas2+dsootf2+dgas3+dsootf3)+dgas4+dsootf4)/6
    soot=soot+(dsootf1-dsooto1+2*(dsootf2+dsootf3-
$ dsooto2-dsooto3)+dsootf4-dsooto4)/6
    t=t+dt
    if (t.lt.time(i+1)) goto 120
    i=i+1
120 if (dis.lt.height(n)) goto 110
    sooth(n)=soot
    tarh(n)=fta1-tarloss
    n=n+1
    if (n.le.nheight) goto 110
    close (10)
    return
    end

```

Appendix F

KINETIC SCHEME FOR METHANE/HYDROGEN COMBUSTION

The following reaction scheme was adopted from the Chemkin manual (Kee, et al., 1985) and used in the simulations of flat flame structures.

ELEMENTS

H O C N

END

SPECIES

CH4 CH3 CH2 CH CH2O HCO CO2 CO

H2 H O2 OH HO2 H2O2 H2O N2 O

END

REACTIONS	!	A		β	E
CH3+H+M=CH4+M		8.0E26	-3.0	0.0	
CH4+O2=CH3+HO2	7.9E13	0.0	56000.		
CH4+H=CH3+H2		2.2E4	3.0	8750.	
CH4+O=CH3+OH		1.6E6	2.36	7400.	
CH4+OH=CH3+H2O	1.6E6	2.1	2460.		
CH3+O=CH2O+H		6.8E13	0.0	0.	
CH3+OH=CH2O+H2	1.0E12	0.0	0.0		
CH3+OH=CH2+H2O	1.5E13	0.0	5000.		
CH3+H=CH2+H2		9.0E13	0.0	15100.	
CH2+H=CH+H2		1.4E19	-2.0	0.	
CH2+OH=CH2O+H		2.5E13	0.0	0.	
CH2+OH=CH+H2O		4.5E13	0.0	3000.	
CH+O2=HCO+O		3.3E13	0.0	0.	
CH+O=CO+H	5.7E13	0.0	0.		
CH+OH=HCO+H		3.0E13	0.0	0.	
CH+CO2=HCO+CO		3.4E12	0.0	690.	
CH2+CO2=CH2O+CO		1.1E11	0.0	1000.	
CH2+O=CO+H+H		3.0E13	0.0	0.	
CH2+O=CO+H2		5.0E13	0.0	0.	
CH2+O2=CO2+H+H	1.6E12	0.0	1000.		
CH2+O2=CH2O+O		5.0E13	0.0	9000.	
CH2+O2=CO2+H2		6.9E11	0.0	500.	

CH2+O2=CO+H2O	1.9E10	0.0	-1000.
CH2+O2=CO+OH+H	8.6E10	0.0	-500.
CH2+O2=HCO+OH	4.3E10	0.0	-500.
CH2O+OH=HCO+H2O	3.43E9	1.18	-447.
CH2O+H=HCO+H2	2.19E8	1.77	3000.
CH2O+M=HCO+H+M	3.31E16	0.0	81000.
CH2O+O=HCO+OH	1.81E13	0.0	3082.
HCO+OH=CO+H2O	5.0E12	0.0	0.
HCO+M=H+CO+M	1.60E14	0.0	14700.
HCO+H=CO+H2	4.00E13	0.0	0.
HCO+O=CO2+H	1.0E13	0.0	0.
HCO+O2=HO2+CO	3.3E13	-0.4	0.
CO+O+M=CO2+M	3.20E13	0.0	-4200.
CO+OH=CO2+H	1.51E7	1.3	-758.
CO+O2=CO2+O	1.6E13	0.0	41000.
HO2+CO=CO2+OH	5.8E13	0.0	22934.
H2+O2=2OH	1.7E13	0.0	47780.
OH+H2=H2O+H	1.17E9	1.3	3626.
H+O2=OH+O	5.13E16	-0.816	16507.
O+H2=OH+H	1.8E10	1.0	8826.
H+O2+M=HO2+M	3.61E17	-0.72	0.
H2O/18.6/ CO2/4.2/ H2/2.86/ CO/2.11/ N2/1.26/			
OH+HO2=H2O+O2	7.5E12	0.0	0.
H+HO2=2OH	1.4E14	0.0	1073.
O+HO2=O2+OH	1.4E13	0.0	1073
2OH=O+H2O	6.0E8	1.3	0.
H+H+M=H2+M	1.0E18	-1.0	0.
H+H+H2=H2+H2	9.2E16	-0.6	0.
H+H+H2O=H2+H2O	6.0E19	-1.25	0.
H+H+CO2=H2+CO2	5.49E20	-2.0	0.
H+OH+M=H2O+M	1.6E22	-2.0	0.
H2O/5/			
H+O+M=OH+M	6.2E16	-0.6	0.
H2O/5/			
H+HO2=H2+O2	1.25E13	0.0	0.
HO2+HO2=H2O2+O2	2.0E12	0.0	0.
H2O2+M=OH+OH+M	1.3E17	0.0	45500.
H2O2+H=HO2+H2	1.6E12	0.0	3800.
H2O2+OH=H2O+HO2	1.0E13	0.0	1800.
END			

Appendix G

TEMPERATURE CORRECTION

In this study, the thermocouple reading obtained in the temperature measurement gave actually the temperature of thermocouple bead T_b . It was corrected for radiative heat loss to obtain the correct post-flame gas temperatures T_g . In the correction, it was assumed that the emissivity of the thermocouple bead ε was 0.2 and the surrounding temperature T_s was 773 K. The diameter of the bead D_b is 0.5 mm, as measured under an optical microscope. The energy balance between radiative heat loss and convective heat gain can be expressed as:

$$h(T_g - T_b) = \varepsilon\sigma(T_b^4 - T_s^4) \quad (\text{G-1})$$

where σ is the Stefan-Boltzmann constant and h is the convective heat transfer coefficient, which is related to the Nusselt number Nu. Because the gas velocity was very slow, the Nusselt number was approximately equal to 2. Therefore, the convective heat transfer coefficient can be expressed as:

$$h = \frac{k_g \text{Nu}}{D_b} = \frac{2k_g}{D_b} \quad (\text{G-2})$$

where, k_g is the heat conductivity of the gas. Combining Eq. G-1 with Eq. G-2, the gas temperature can be solved as:

$$T_g = T_b + \frac{\varepsilon\sigma D_b (T_b^4 - T_s^4)}{2k_g} \quad (\text{G-3})$$

Appendix H

TABULATION OF EXPERIMENTAL DATA

Data from Figure 3.3: Centerline gas temperature profile in the quartz tower

z (cm)	Thermocouple Reading (K)			Collected Gas Temperature (K)		
	$T_m=1650$	$T_m=1800$	$T_m=1900$	$T_m=1650$	$T_m=1800$	$T_m=1900$
0.64	1461	1618	1643	1590.7	1795.1	1828.1
1.27	1488	1628	1673	1625.4	1808.3	1867.9
1.91	1496	1638	1693	1635.8	1821.5	1894.5
2.54	1500	1637	1693	1641.0	1820.2	1894.4
3.18	1500	1636	1693	1641.0	1818.9	1894.4
3.81	1498	1633	1688	1638.4	1814.9	1887.8
5.08	1494	1626	1683	1633.2	1805.7	1881.1
6.35	1487	1614	1673	1624.2	1789.9	1867.8
7.62	1483	1605	1658	1619.0	1778.0	1847.9
8.89	1475	1593	1650	1608.7	1762.2	1837.4
10.16	1467	1581	1633	1598.4	1746.5	1814.9
12.70	1452	1555	1609	1579.1	1712.5	1783.2
15.24	1431	1532	1578	1552.2	1682.5	1742.5
17.78	1412	1504	1547	1528.0	1646.1	1702.0
20.32	1390	1478	1513	1500.1	1612.5	1657.8
22.86	1368	1446	1483	1472.3	1571.4	1619.00

† z is the height above the flat flame.

‡ T_m represents the temperature condition (close to the maximum temperature).

Data from Figure 3.4: Centerline gas temperature profile in the Pyrex tower

Height Above Flat Flame, z (cm)	Thermocouple Reading (K)	Corrected Gas Temperature (K)
1.27	1330	1775.4
2.54	1380	1841.4
5.08	1374	1833.4
7.62	1355	1808.3
10.16	1334	1780.6
15.24	1275	1703.3
20.32	1220	1631.9

Data from Figure 3.5: Horizontal gas temperature profile in the quartz tower

Thermocouple Reading (K)					
x (cm)	$z=1.3$ cm	$z=2.5$ cm	$z=5.0$ cm	$z=7.6$ cm	$z=10.2$ cm
0.000	1384	1421	1410	1385	1359
0.305	1420	1433	1422	1405	1378
0.635	1453	1454	1432	1415	1388
0.889	1461	1463	1441	1422	1389
1.270	1456	1467	1441	1420	1374
1.651	1445	1463	1421	1380	1340
1.905	1417	1440	1380	1310	1240
2.159	1350	1350	1200	1080	1130
2.413	1270	1220	1000	1000	1000

Collected Gas Temperature (K)					
x (cm)	$z=1.3$ cm	$z=2.5$ cm	$z=5.0$ cm	$z=7.6$ cm	$z=10.2$ cm
0.000	1846.7	1895.8	1881.2	1848.0	1813.6
0.305	1894.5	1911.8	1897.1	1874.5	1838.7
0.635	1938.4	1939.8	1910.4	1887.8	1852.0
0.889	1949.1	1951.8	1922.4	1897.1	1853.3
1.270	1942.4	1957.1	1922.4	1894.5	1833.4
1.651	1927.7	1951.8	1895.8	1841.4	1788.5
1.905	1890.5	1921.1	1841.4	1749.1	1657.8
2.159	1801.7	1801.7	1606.1	1453.4	1516.6
2.413	1696.8	1631.9	1353.8	1353.8	1353.8

† z is the height above the flat flame.

‡ x is the distance to the centerline of the tower.

Data from Figure 3.6: Radial gas temperature profile in the Pyrex tower

Thermocouple Reading (K)							
R (cm)	$z=1.3$	$z=2.5$	$z=5.0$	$z=7.6$	$z=10.2$	$x=15.2$	$x=20.3$
0.000	1330	1380	1374	1355	1334	1275	1220
0.254	1371	1391	1375	1355	1330	1265	1215
0.508	1418	1411	1378	1354	1320	1260	1205
0.762	1435	1422	1381	1353	1315	1250	1180
1.016	1438	1423	1372	1340	1305	1220	1150
1.270	1438	1418	1360	1315	1250	1200	1110
1.524	1432	1405	1325	1275	1210	1120	1090
1.778	1418	1370	1270	1200	1160	1080	1050
2.032	1380	1300	1150	1100	1080	1030	1000
2.286	1220	1120	1010	1000	1000	950	920
2.540	1000	950	900	910	940	880	900
2.794	700	800	800	830	870	850	860
Corrected Gas Temperature (K)							
R (cm)	$z=1.3$	$z=2.5$	$z=5.0$	$z=7.6$	$z=10.2$	$x=15.2$	$x=20.3$
0.000	1775.4	1841.4	1833.4	1808.3	1780.6	1703.3	1631.9
0.254	1829.5	1855.9	1834.7	1808.3	1775.4	1690.3	1625.4
0.508	1891.8	1882.5	1838.7	1807.0	1762.2	1683.8	1612.5
0.762	1914.4	1897.1	1842.7	1805.7	1755.7	1670.8	1580.4
1.016	1918.4	1898.4	1830.8	1788.5	1742.6	1631.9	1542.0
1.270	1918.4	1891.8	1814.9	1755.7	1670.8	1606.1	1491.2
1.524	1910.4	1874.5	1768.8	1703.3	1619.0	1503.9	1466.0
1.778	1891.8	1828.1	1696.8	1606.1	1554.8	1453.4	1415.9
2.032	1841.4	1736.0	1542.0	1478.6	1453.4	1390.9	1353.8
2.286	1631.9	1503.9	1366.2	1353.8	1353.8	1292.5	1256.1
2.540	1353.8	1292.5	1231.9	1244.0	1280.3	1207.9	1231.9
2.794	997.1	1113.0	1113.0	1148.4	1196.0	1172.1	1184.0

† z is the height above the flat flame in cm.

‡ R is the radial distance to the centerline of the tower.

Data from Figure 4.15: Volatiles yields and soot yields for Pittsburgh #8 coal

Temp (K)	z (cm)	t (ms)	Char	Soot (<5 μm)	Soot (>5 μm)	Soot (total)	Volatile
1900	2.54	13.7	40.7	16.13	0.00	16.13	59.3
	5.08	23.2	43.2	5.51	11.92	17.43	56.8
	7.62	31.9	43.0	4.03	14.80	18.83	57.0
	10.2	40.2	42.4	2.71	16.46	19.17	57.6
1800	2.54	14.2	43.3	18.23	0.00	18.23	56.7
	5.08	23.9	43.8	8.66	9.57	18.23	56.2
	7.62	32.6	44.6	5.91	12.08	17.99	55.4
	10.2	40.9	43.9	4.30	15.53	19.83	56.1
1650	2.54	14.6	43.9	20.26	0.00	20.26	56.1
	5.08	24.7	45.1	22.34	1.00	23.34	54.9
	7.62	33.9	44.8	17.70	2.84	20.54	55.2
	10.2	42.5	46.3	15.57	6.41	21.98	53.7

† All yields are weight percentage on dry ash-free basis.

‡ z is collection height above the coal injection point.

¶ t is particle residence time.

Data from Figure 4.16: Volatiles yields and soot yields for Illinois #6 coal

Temp (K)	z (cm)	t (ms)	Char	Soot (<5 μm)	Soot (>5 μm)	Soot (total)	Volatile
1900	2.54	14.0	34.1	13.66	0.00	13.66	65.9
	5.08	23.6	34.8	6.36	8.08	14.44	65.2
	7.62	32.3	33.8	4.08	10.72	14.80	66.2
	10.2	40.5	31.9	3.11	13.11	16.22	68.1
1800	2.54	14.4	35.9	15.48	0.00	15.48	64.1
	5.08	24.6	36.7	9.80	7.12	16.92	63.3
	7.62	33.8	34.2	5.65	11.94	17.60	65.8
	10.2	42.5	33.5	4.45	12.19	16.64	66.5
1650	2.54	14.6	34.9	17.03	0.00	17.03	65.1
	5.08	25.2	37.5	19.88	1.13	21.01	62.5
	7.62	34.9	37.7	17.83	1.03	18.85	62.3
	10.2	44.0	35.8	15.22	5.41	20.63	64.2

† All yields are weight percentage on dry ash-free basis.

‡ z is collection height above the coal injection point.

¶ t is particle residence time.

Data from Figure 4.17: Volatiles yields and soot yields for Utah Hiawatha coal

Temp (K)	z (cm)	t (ms)	Char	Soot (<5 μm)	Soot (>5 μm)	Soot (total)	Volatile
1900	2.54	13.6	45.6	9.91	0.00	9.91	54.4
	5.08	23.0	40.3	5.84	5.88	11.72	59.7
	7.62	31.8	39.2	4.53	7.08	11.62	60.8
	10.2	40.0	40.3	2.72	10.76	13.49	59.7
1800	2.54	14.0	43.1	11.79	0.00	11.79	56.9
	5.08	23.9	42.1	7.93	3.11	11.04	57.9
	7.62	32.9	41.1	7.52	4.30	11.82	58.9
	10.2	41.5	39.7	3.94	9.61	13.55	60.3
1650	2.54	14.3	46.0	12.16	0.00	12.16	54.0
	5.08	24.6	45.6	14.73	1.14	15.87	54.4
	7.62	34.3	42.6	15.32	0.78	16.11	57.4
	10.2	43.6	44.4	13.93	2.38	16.31	55.6

† All yields are weight percentage on dry ash-free basis.

‡ z is collection height above the coal injection point.

¶ t is particle residence time.

Data from Figure 4.18: Volatiles yields and soot yields for Pocahontas #3 coal

Temp (K)	z (cm)	t (ms)	Char	Soot ($<5 \mu\text{m}$)	Volatile
1900	2.54	14.2	75.38	5.41	24.62
	5.08	24	78.02	2.28	21.98
	7.62	32.8	78.12	1.60	21.88
	10.2	41.2	78.91	1.26	21.09
1800	2.54	14.2	76.18	7.38	23.82
	5.08	24.2	77.01	3.92	22.99
	7.62	33.4	78.73	2.63	21.27
	10.2	42.2	80.98	2.20	19.02
1650	2.54	14.8	79.84	9.56	20.16
	5.08	25.6	76.93	8.72	23.07
	7.62	35.4	77.37	7.76	22.63
	10.2	44.6	80.39	7.12	19.61

† All yields are weight percentage on dry ash-free basis.

‡ z is collection height above the coal injection point.

¶ t is particle residence time.

Data from Figure 4.18: Volatiles yields and soot yields for Dietz coal

Temp (K)	z (cm)	t (ms)	Char	Soot ($<5 \mu\text{m}$)	Volatile
1900	2.54	14	41.56	6.66	58.44
	5.08	24.5	40.86	4.90	59.14
	7.62	34.4	38.75	3.28	61.25
	10.2	43.9	33.34	2.27	66.66
1800	2.54	14.4	42.16	6.71	57.84
	5.08	24.3	40.94	6.88	59.06
	7.62	33.2	39.85	4.72	60.15
	10.2	41.6	37.06	3.34	62.94
1650	2.54	14.5	50.26	7.54	49.74
	5.08	25	45.36	10.14	54.64
	7.62	34.8	40.56	10.71	59.44
	10.2	44.2	40.09	9.82	59.91

† All yields are weight percentage on dry ash-free basis.

‡ z is collection height above the coal injection point.

¶ t is particle residence time.

Data from Figure 4.18: Volatiles yields and soot yields for Zap lignite

Temp (K)	z (cm)	t (ms)	Char	Soot (<5 μm)	Volatile
1900	2.54	13.4	44.37	2.07	55.63
	5.08	22.7	36.82	2.81	63.18
	7.62	31.5	32.06	2.69	67.94
	10.2	39.9	28.67	2.56	71.33
1800	2.54	13.5	45.83	2.31	54.17
	5.08	23	39.81	3.08	60.19
	7.62	32.1	35.30	3.08	64.70
	10.2	40.8	37.22	2.72	62.78
1650	2.54	14.5	48.27	2.48	51.73
	5.08	25	46.74	4.13	53.26
	7.62	34.9	42.01	4.93	57.99
	10.2	44.2	39.02	5.37	60.98

† All yields are weight percentage on dry ash-free basis.

‡ z is collection height above the coal injection point.

¶ t is particle residence time.

Data from Figures 4.24 through 4.28: Elemental composition of soot samples

Coal Type	Temperature (K)	z=2.54 (cm)			z=10.2 (cm)		
		C	H	N	C	H	N
Pittsburgh #8	1650	90.6	1.46	0.67	94.8	1.21	0.38
	1800	96.6	0.93	0.69	96.8	0.92	0.23
	1900	98.5	0.85	0.60	96.9	1.09	0.28
Illinois #6	1650	94.2	1.57	0.59	95.4	0.62	0.69
	1800	95.3	0.41	0.60	94.4	0.42	0.92
	1900	97.1	0.74	0.56	90.4	0.97	0.26
Utah Hiawatha	1650	96.6	1.41	0.55	95.4	0.90	0.65
	1800	96.8	0.57	0.73	93.6	0.61	0.50
	1900	95.0	0.49	0.66	91.9	0.37	0.83
Pocahontas #3	1650	94.1	1.61	0.22	98.1	1.49	0.37
	1800	93.4	0.94	0.21	90.9	0.91	0.48
	1900	96.9	0.75	0.18	93.2	1.15	0.11
Dietz	1650	96.2	2.42	0.34	97.8	1.43	0.73
	1800	90.3	1.06	0.40	91.6	0.99	0.44
	1900	94.7	0.76	0.55	85.5	0.90	0.44

Data from Figures 4.29 through 4.31: Elemental composition of char samples

Coal Type	Temperature (K)	z=2.54 (cm)			z=10.2 (cm)		
		C	H	N	C	H	N
Pittsburgh #8	1650	84.5	1.00	1.55	84.7	0.48	1.42
	1800	86.8	0.82	0.95	87.7	0.34	1.54
	1900	81.0	0.63	1.26	87.3	0.13	1.39
Illinois #6	1650	74.7	1.38	1.04	76.3	0.00	1.30
	1800	69.8	0.82	1.29	74.9	0.00	1.31
	1900	nm	nm	nm	75.7	0.11	1.38
Utah Hiawatha	1650	nm	nm	nm	74.7	0.64	1.17
	1800	nm	nm	nm	73.6	0.89	1.10
	1900	nm	nm	nm	76.0	0.91	1.14
Dietz	1650	79.4	1.65	1.03	83.2	0.73	1.19
	1800	82.1	1.36	0.81	82.4	0.30	1.17
	1900	80.8	0.66	1.20	83.5	0.30	1.12

nm: Data not measured.